Author:
Ansell, Oliver J

Title:
Design and fabrication of photonic components based on active vertical coupler structures

Design and fabrication of photonic components based on active vertical coupler structures

Oliver J Ansell

A dissertation submitted to the University of Bristol in accordance with the requirements of the degree of PhD in the Faculty of Engineering.

Word Count: 20231

PAGE NUMBERING AS ORIGINAL

Abstract

This thesis presents and validates a model for designing multimode SOA-like waveguide devices. This model was used to design an active vertical coupler wavelength converter device making use of both cross-gain and cross-phase modulation. The simulated output extinction ratio was over 30dB for a maximum input pump level of under 6 dBm.

A multi-quantum well wafer structure was designed and ordered. Two rounds of devices were designed and multiple fabrication processes developed. These included three levels of etch depth, for which one depth was required to be correct within a small tolerance. Also, the dry plasma etch was required to create totally internally reflecting mirrors in a two step etch so much development was required for this step to keep the surface optically smooth. After the fabrication process development devices were successfully fabricated with good quality waveguides and totally internally reflecting mirrors.

Characterisation of completed devices exhibit coupling and gain variation due to carrier modulation. The extinction ratio of the devices has been measured as over 30dB with varying current injection. The transmission extinction ratio has been measured as over 20dB with varying injection current.

It was discovered that the fabricated devices have a low quantum efficiency (μ_e). This prevented high carrier concentration which made optical saturation too small to observe. Although all-optical wavelength conversion was not demonstrated, the successful modulation of the coupling due to carrier population changes by injection current has demonstrated the operation principles. Optical saturation of the carrier density and modulation of the coupling should be achievable with a wafer design that has improved carrier confinement in the active layer.

Probable solutions to all these problems have been described which should result in high quality devices.

Author's Declaration

I declare that the work in this dissertation was carried out in accordance with the Regulations of the University of Bristol. The work is original, except where indicated by special reference in the text, and no part of the dissertation has been submitted for any other academic award. Any views expressed in the dissertation are those of the author.

Signed: .....

Date: 22/08/2008

Contents

List of Figures

List of Tables

Publications

A list of publications is included below. They are also included in the bibliography where they are cited in the text of the thesis.

S.C. Lee, R. Varraza, O. Ansell, C. Born and S. Yu. Optical packet multicast operation using active vertical coupler (AVC) based 4×4 optical crosspoint switch matrix. *Lasers and Electro-Optics Society, 2004. LEOS 2004. The 17th Annual Meeting of the IEEE*, 2, 2005.

S.C. Lee, R. Varrazza, O. Ansell, and S. Yu. Highly Flexible 4×4 Optical Crosspoint Packet Switch Matrix for Optical Multicast Operations. *Photonics Technology Letters, IEEE*, 17(4):911–913, 2005. [18]

S. Yu, S.C. Lee, O. Ansell and R. Varrazza. Lossless Optical Packet Multicast Using Active Vertical Coupler Based Optical Crosspoint Switch Matrix. *Lightwave Technology, Journal of*, 17(10):2984–2992, 2005. [41]

N. Chi, J. J. Vegas Olmos, K. Thakulsukanant, Z. Wang, O. Ansell, S. Yu and D. Huang. Experimental characteristics of optical crosspoint switch matrix and its applications in optical packet switching. *Journal of lightwave technology*, 24(10):3646–3653, 2006. [2]

N. Chi, Z. Wang, O. Ansell and S. Yu. Improvement of switching properties and cascadability of an ultra-fast reconfigurable optical crosspoint switch matrix using DPSK payloads. *Optics Communications*, 265(1):120–125, 2006.

Chapter 1

Introduction

1.1. Brief history

The "optical telegraph" is the first known system to transmit data optically. The system used semaphore towers, invented by Claude Chappe in the 1790s [14]. There were people stationed in the towers who would see a signal from a tower in the distance and pass it on in the correct direction by moving flags around. This system was much faster than sending a message over land, however it would stop completely when the weather caused bad visibility. Optical data transmission systems as we know them now have been in use since the early 1970s. This is when the development of light emitting diodes, semiconductor lasers capable of high speed modulation, low loss glass fibre and solid state detectors all reached a state where the technology could be implemented [6]. The first equipment made use of only the low loss window in the fibre transmission spectrum at around 850nm due to the sources and detectors that were available at that time. After a breakthrough by Kao and Hockham, they manufactured fibres with only a 10dB loss over 2.5Km [15]. When the fibre technology had improved, the lower loss window at around 1310nm became accessible. The 1550nm window was first used in the late 1970s and is the current wavelength range of choice due to the smallest theoretical loss of 0.2dB/Km [24]. The 1550nm window is known as the C band and recently an extension to the C band has been developed allowing use of fibres into longer wavelengths of around 1625nm and is called the L band [13]. See Figure 1.1 for a graphical representation of the transmission spectrum of optical fibres.

Optical communication technology has been continually improving over the past few decades with a drive for faster, cheaper, longer links with greater capacities. As the demand for backbone network capacity has been doubling annually and seems set to continue [3] there will still be the need for improvements to the transmission

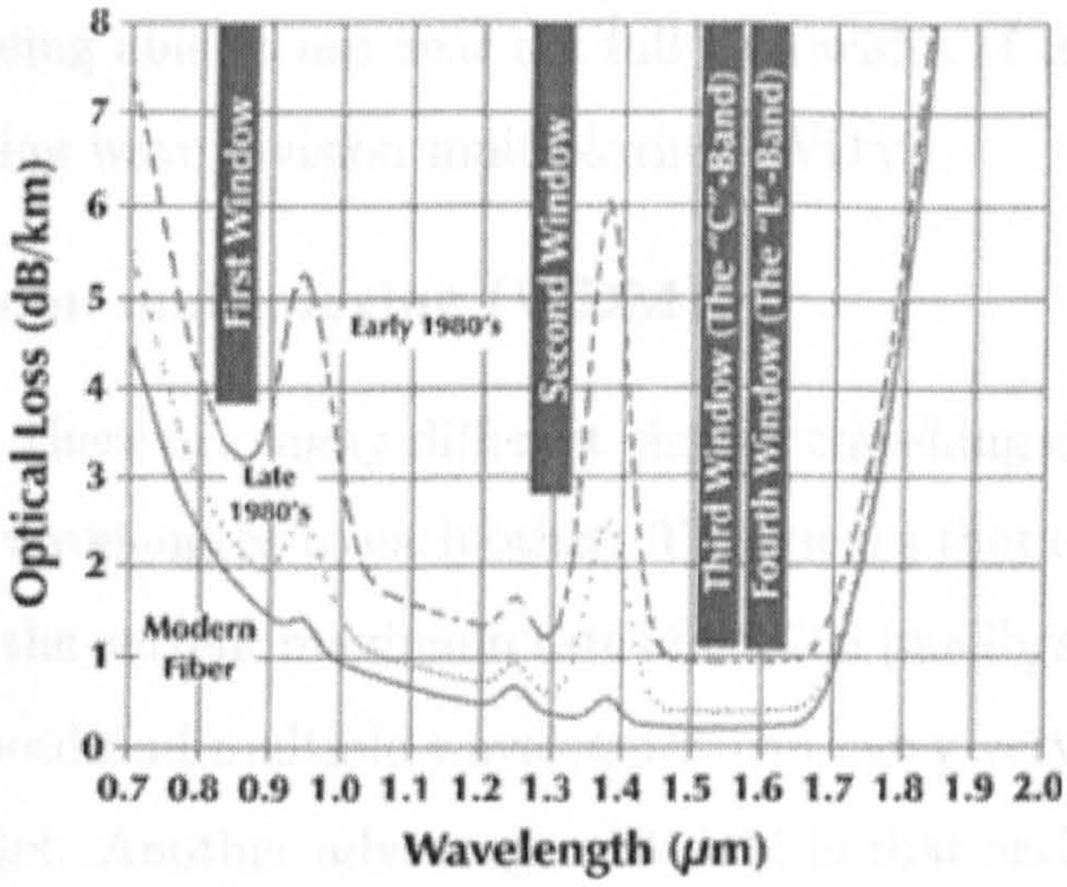

Figure 1.1: Optical fibre spectrum [6]

technology in the future.

1.2. Point to point system

The simplest form of a optical fibre data link is in a point to point system where electrical data is modulated onto a carrier wavelength at the transmitter. This may be via direct modulation of the optical source or using an external modulator in series with a constant level source. The light is transmitted through some length of optical fibre where the signal is degraded by absorption, scattering, dispersion and some self modulation. At the end of the fibre the light is detected and converted back to electronic signals for whatever processing is required.

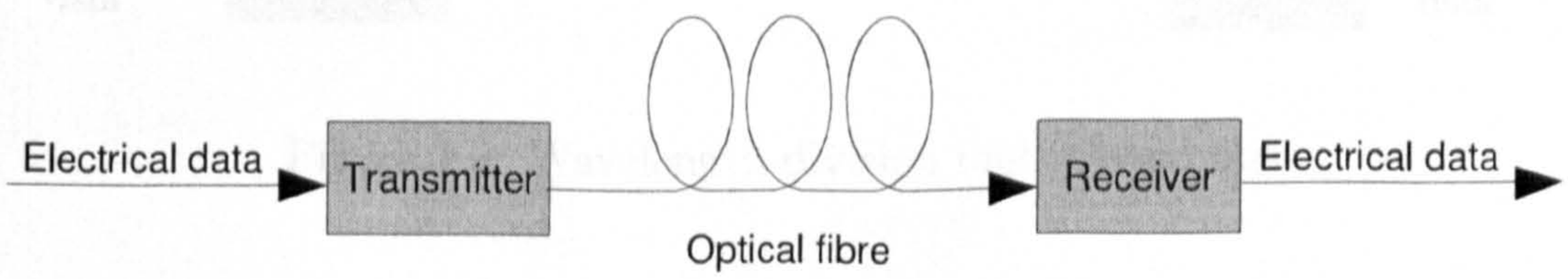

Figure 1.2: Optical point to point link

1.2.1. Multiplexing

A single data link has some limitations. The theoretical bandwidth limit of optical fibre, assuming a linear channel is in the region of $330Tb/s$ [23] and digital electronics is unlikely to ever reach this processing speed. A method of transmitting at slower

speeds while still being able to use near the full bandwidth of the fibre was needed. This is achieved using wave division multiplexing (WDM).

Wavelength division multiplexing (WDM)

In a WDM system, there are many different signals travelling down the same fibre on different carrier wavelengths to each other. This means that each wavelength can carry data at up to the current maximum rate of OC768 (40Gb/s), so the electronics can work at this speed and multiple wavelengths can carry very large quantities of data when in parallel. Another advantage of WDM is that each channel can work at different speeds, so the hardware can be improved bit by bit as the need arises [25]. The multiplexer (mux) and de-multiplexer (demux) shown in figure 1.3 are normally arrayed waveguide gratings (AWGs) that spatially separate or combine different carrier wavelengths [31].

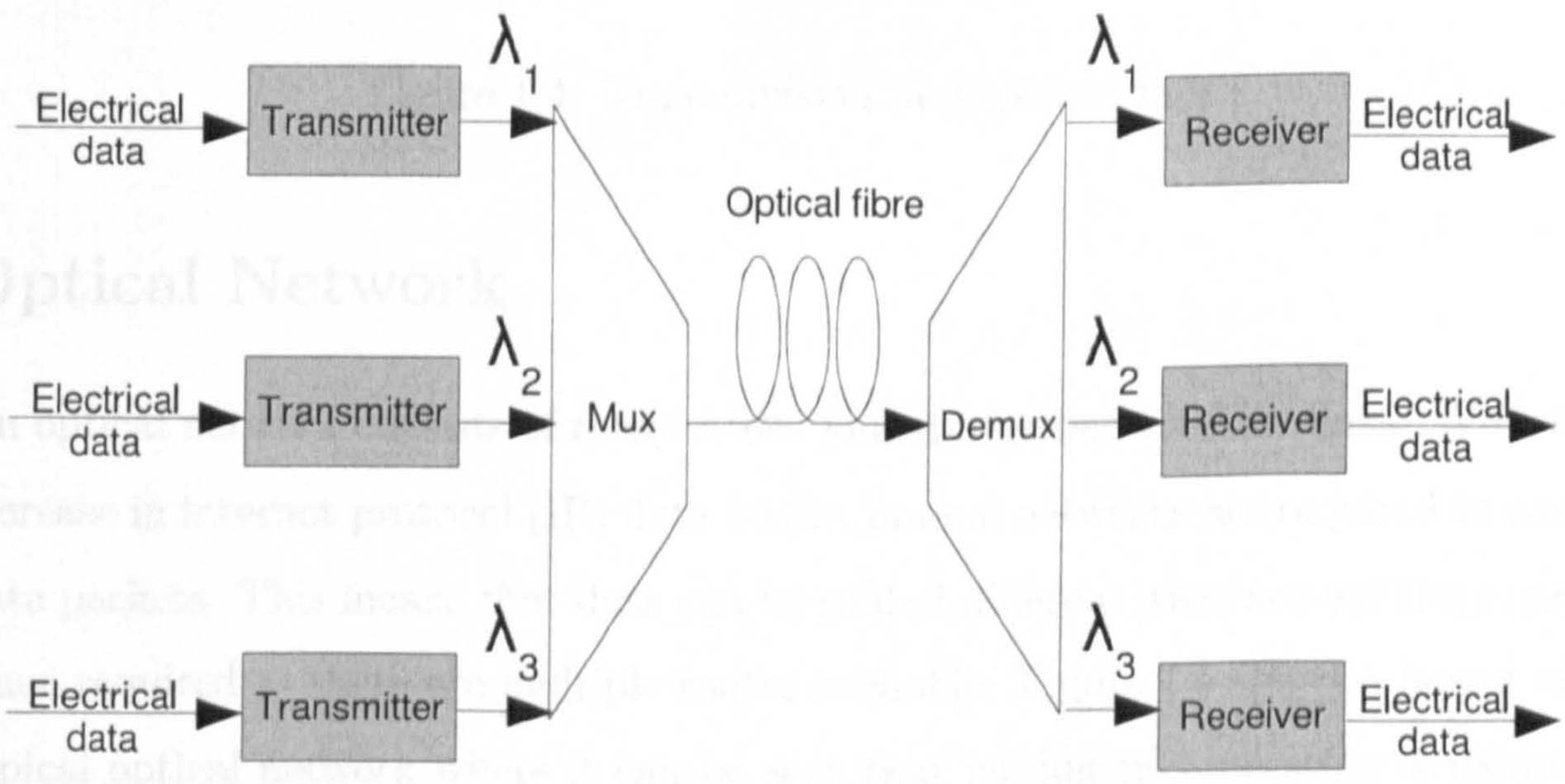

Figure 1.3: Wavelength division multiplexed link

Optical time division multiplexing (OTDM)

OTDM can be used with return to zero (RZ) data encoding as multiple slow signals can be transmitted with delays between each one, so that when they are added together they do not interfere. This means that the electronics used to process the data need only run at a lower speed where the only high speed parts are short pulse generators. The short pulses can be produced as short as 5.8ps [21] or 20fs [22]. An

alternative demultiplexing technique is shown in [10] using a semiconductor laser amplifer to act as a switch to extract 10GB/s data from a 40GB/s data stream.

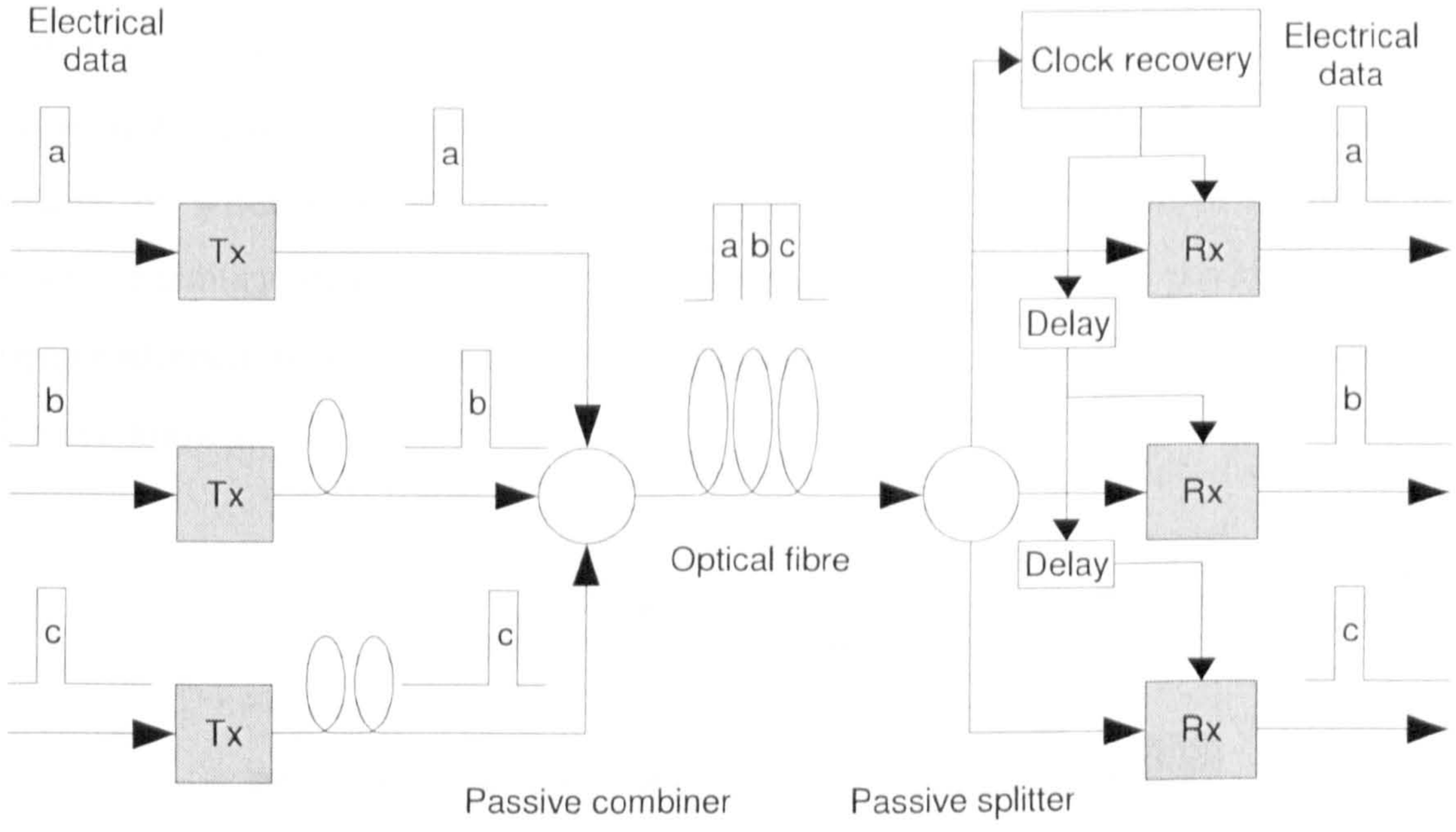

Figure 1.4: Time division multiplexed link

1.3. Optical Network

An optical network consists of many nodes joined together via fibre links. With the increase in internet protocol (IP) data traffic, optical networks are required to route data packets. This means that data can be routed different ways around the system when required as there are multiple routes available. Figure 1.5 shows a layout of a typical optical network where it can be seen that intelligent processing is required at the nodes.

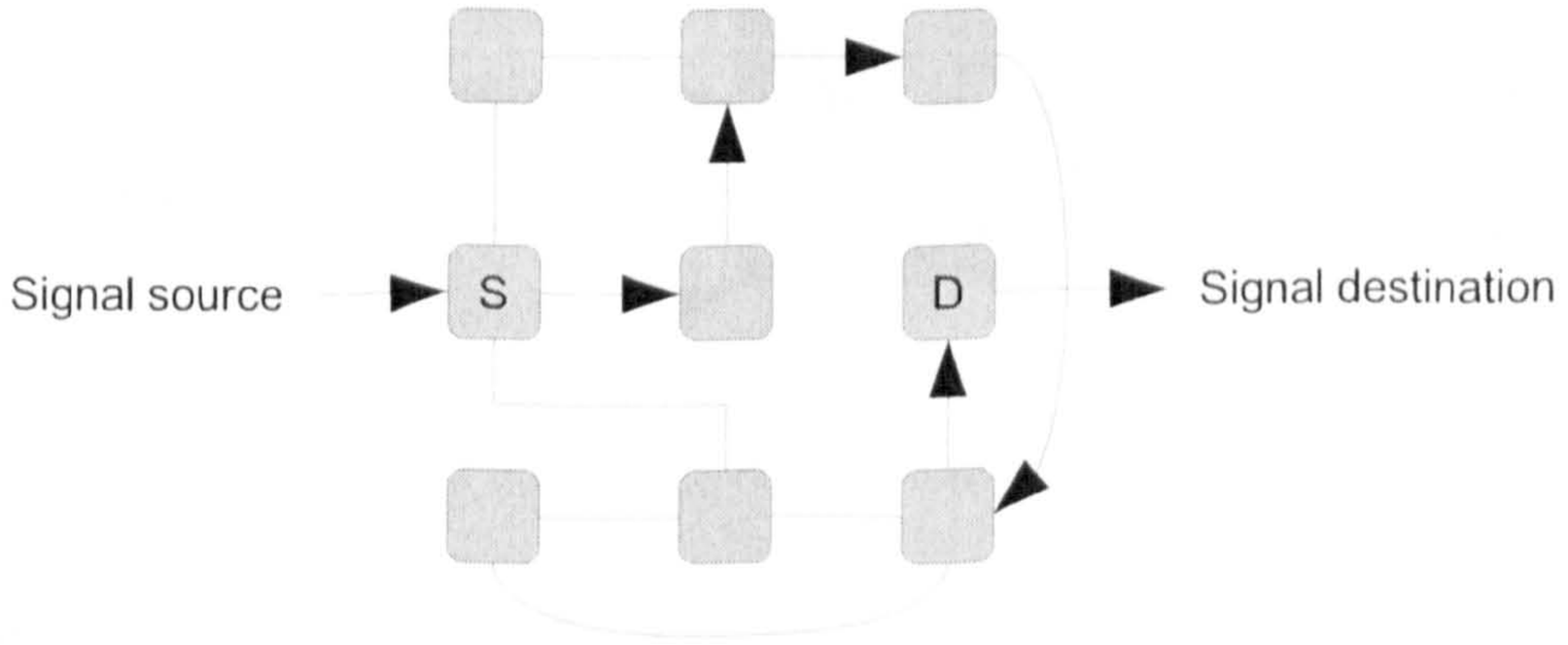

Figure 1.5: Optical network overview

Optical-electric-optical node

The network nodes available on the market at the current time require all the data from the incoming fibre to be converted to high-speed electronics, processed then retransmitted to the correct destination. This method ensures that the signal is cleaned up when it is retransmitted. However, it is very wasteful in terms of processing, memory and power. The bulk of the data, known as the payload, does not require alteration, so could be routed without any processing if the destination was already known.

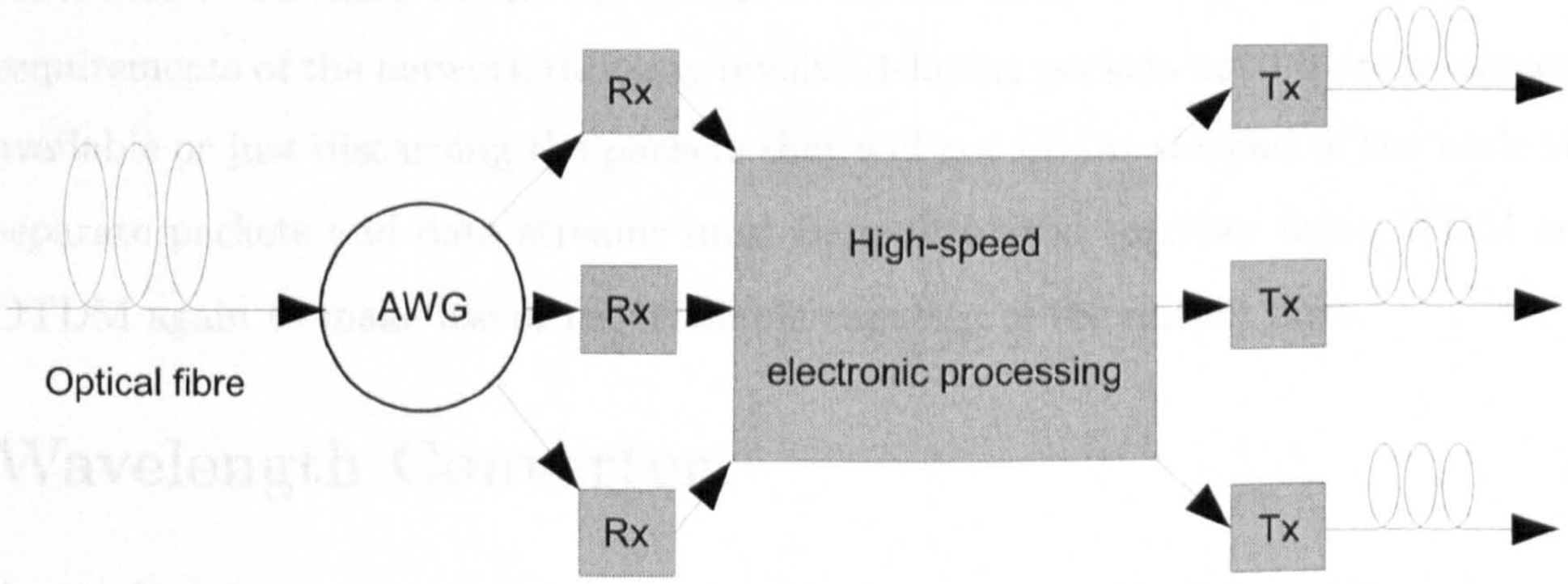

Figure 1.6: Optical-electrical-optical node

All optical node

For an all optical node to become a reality there are a selection of processes that must occur to avoid converting the payload into electronic data.

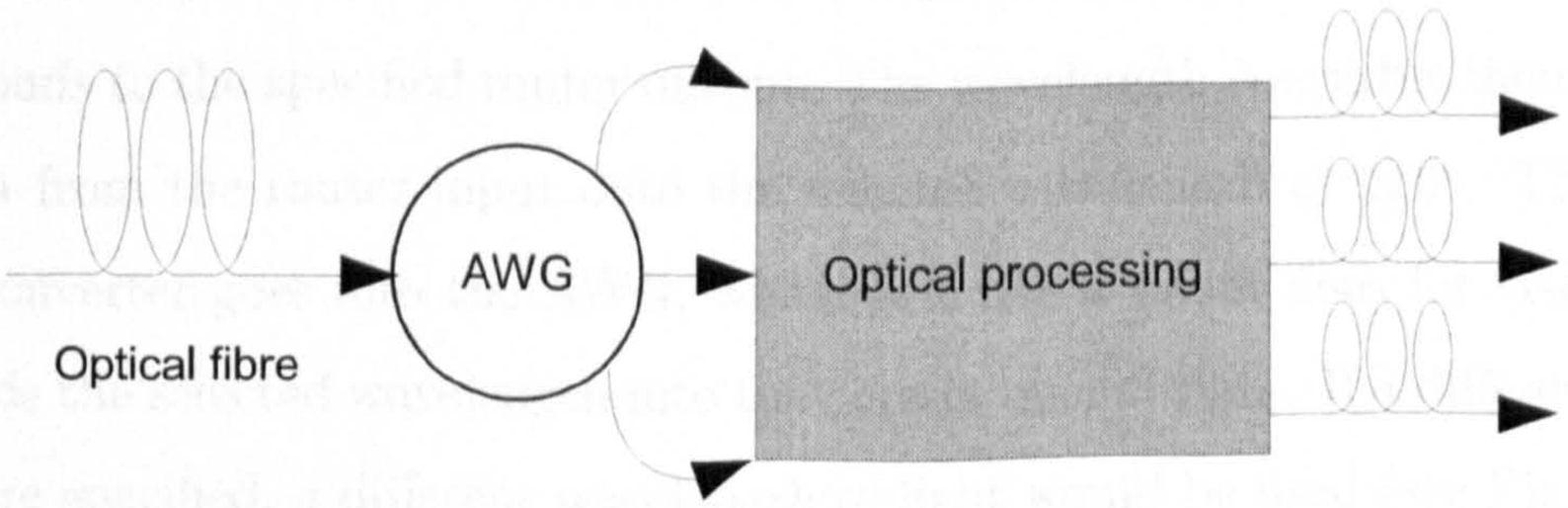

Figure 1.7: All-optical node

Demultiplexing from WDM and OTDM is required so that each packet or data stream can be routed separately. These processes are discussed in sections 1.2.1 and 1.2.1. The header extraction and processing [4] can be achieved at lower electronic

speeds by using one channel of the fibre for header data that can be modulated at a much lower data rate. This method can be used where the payload packets are much longer than the header so that there is time for the slower processing. The payload may be sent down a delay path while the rest of the node reconfigures according to the header data. Wavelength conversion is required to transfer the payload onto the wavelength to be transmitted. A Crosspoint switch is then needed to route the payload to the correct output fibre [16][8]. There is the possibility of many packets needing to be sent down the same fibre at exactly the same time so there must be some sort of blocking resolution to cope with this situation [4]. Depending on the requirements of the network this may involve delaying packets until there is capacity available or just discarding the packets that will not fit. At the end of the node the separate packets and data streams must be multiplexed together using WDM and OTDM again to make use of the available capacity of the output fibre.

1.4. Wavelength Converter

A wavelength converter takes data modulated on one carrier wavelength and transfers it onto an alternative carrier wavelength. This process is similar to changing the carrier frequency of a radio frequency data stream. One important use of a wavelength converter is in conjunction with a tunable laser and an AWG (arrayed waveguide grating) in a router system. The data in the header at the router input contains information that is used to select the router output to which the data should be sent. The input information is used to set the tunable laser to a wavelength that corresponds to the specified router output. The wavelength converter then transfers the data from the router input onto the selected wavelength of light. The output of the converter goes into the AWG, which acts like a prism does for visible light, and sends the selected wavelength into the correct output fibre. If a different output fibre were specified, a different wavelength of light would be used (see Figure 1.8).

Routers that incorporate wavelength converters are required in all-optical wave division multiplexed (WDM) networks to enable each link of the network to operate independently (see Figure 1.9). Without wavelength conversion, wavelengths would have to be specified across the whole network [1].

The current technology for interconnects at nodes in an optical network involves

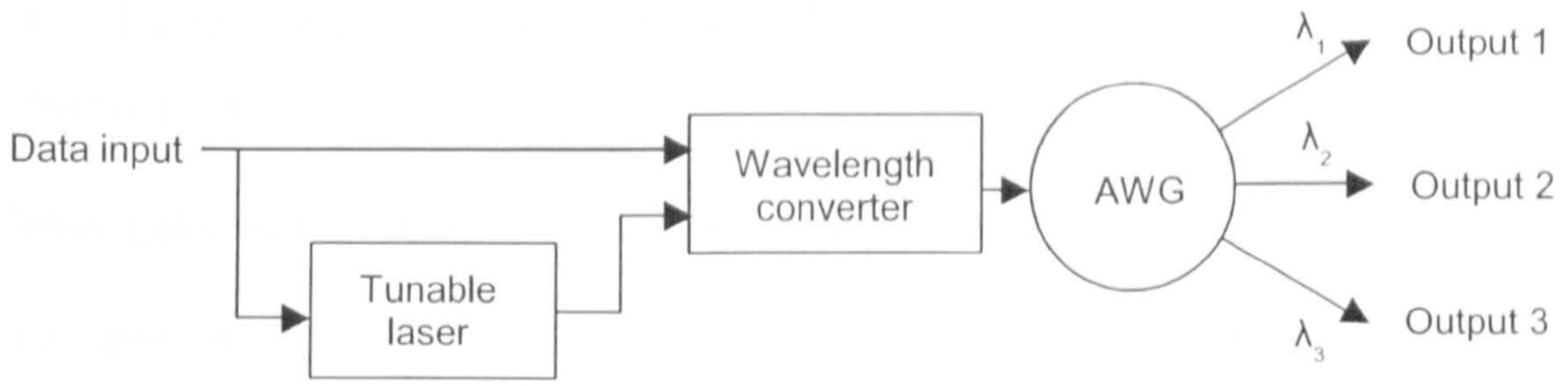

Figure 1.8: An all-optical router incorporating a wavelength converter

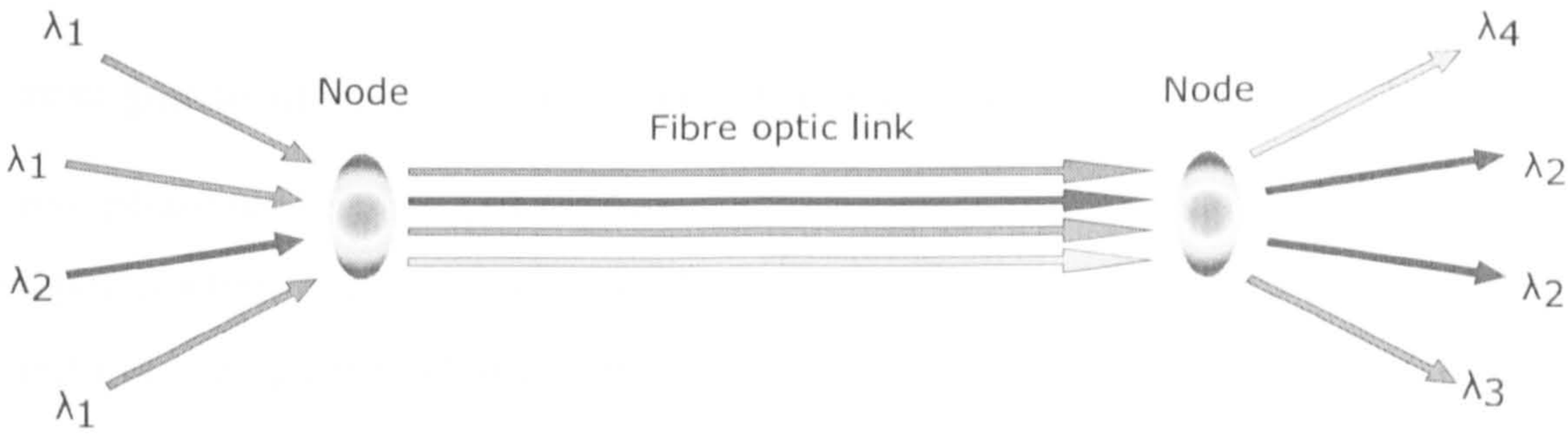

Figure 1.9: Optical network link using a wavelength converter

demodulating the data received at a node onto a high-speed electronic circuit. The routing of the data is then handled using high-speed logic and the signals are modulated onto new wavelengths and transmitted down the correct fibre-optic links. This process is effectively using optical-electrical-optical wavelength converters. This system is relatively slow compared to the possibilities of all-optical systems. Also, the high-speed electronic circuitry has high power consumption and is expensive to manufacture. All-optical wavelength converters have the potential to be faster, cheaper and simpler to implement, as there are fewer stages in the interlink system.

Wavelength converters that can only convert between half the range of possible wavelengths in a network reach close to the improvement of full conversion [39] so when designing a wavelength converter it is not a requirement to be able to convert over the whole fibre spectrum all though it would be one of the aims.

1.4.1. Previous wavelength converter research

Conventional all-optical wavelength converter (WC) devices based on semiconductor optical amplifiers (SOA) have been researched for some time [40]. There are five main types of wavelength converter which are explained below in sections 1.4.1-

1.4.1. These sections also detail the draw backs of previous SOA based wavelength converters [9].

Cross gain modulation wavelength converters

Cross gain modulation (XGM) based wavelength conversion uses the gain saturation of an SOA as a means of modulating the output [11]. This mechanism is fully explained in section 2.1.1. The main drawback with XGM is that only limited extinction ratios can be achieved.

Cross phase modulation wavelength converters

Cross phase modulation (XPM) based wavelength conversion makes use of two optical paths where only one path has the optical pump signal. This causes the optical length of that path to change with high pump power, therefore changing the interference between the outputs of the two paths [11]. Both paths require the use of a SOA, so the device has high power consumption. XPM requires an interferometer structure (most popularly the Mach-Zehnder interforeometer - MZI), which is complicated to fabricate and has high optical loss in the passive 3-dB couplers used to form the MZI. In theory this can achieve high extinction ratio but in practice extinction ratio is limited by the 3-dB coupler split ratio accuracy.

Four wave mixing wavelength converters

Four wave mixing (FWM) is a cause of crosstalk in WDM systems as it is the formation of a different wavelength of light when the fibre has three or more wavelengths travelling through it. FWM occurs due to non-linear effects in the fibre so it also occurs in non-linear SOAs. Due to this effect FWM can be used to enable wavelength conversion [11]. The main disadvantages of FWM are that it requires three input wavelengths, so there are more wavelengths that need to be filtered from the output and that the conversion efficiency is very sensitive to the wavelength shift [43] as can be seen in figure 1.10.

Ultra-fast nonlinear interferometer wavelength converters

Ultra-fast nonlinear interferometer (UNI) converters use cross gain modulation in an SOA to modulate the output signal where polarisation is used to improve the

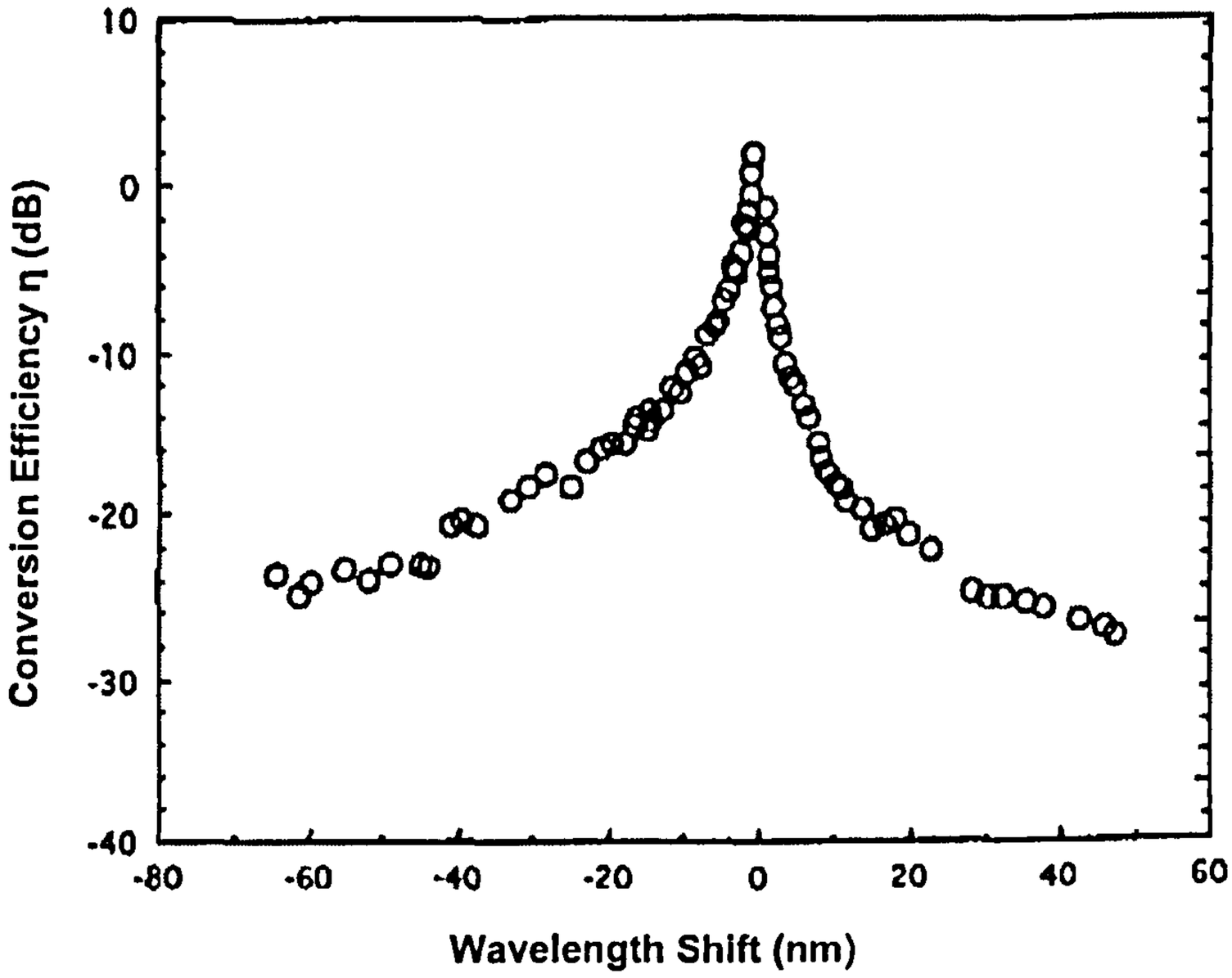

Figure 1.10: Four wave mixing conversion efficiency with wavelength shift [43]. η is the output power relative to the input power depending on the wavelength shift required to transfer from the input wavelength to the output wavelength.

extinction ratio [27].

1.5. Active vertical coupler

An active vertical coupler structure can be used to achieve wavelength conversion. This structure has been used to fabricate optical cross-point switches [42] [38] and is a vertical coupler where the top waveguide is active and the bottom waveguide is passive. The vertical waveguide coupler design, shown in Figure 1.11 (a), is easier to manufacture than a horizontal waveguide coupler, shown in Figure 1.11 (b) [20], as only the vertical dimension requires a tight tolerance. The alignment of the inputs and outputs onto the device are also not as sensitive to lateral skew. Also, the vertical structure allows many devices to be integrated on a single chip, linked by a lower passive waveguide.

The active vertical coupler (AVC) structure uses a combination of cross gain and cross phase modulation, which gives improvements over alternate device designs. The AVC can be modelled as an interferometer structure due to the interference of

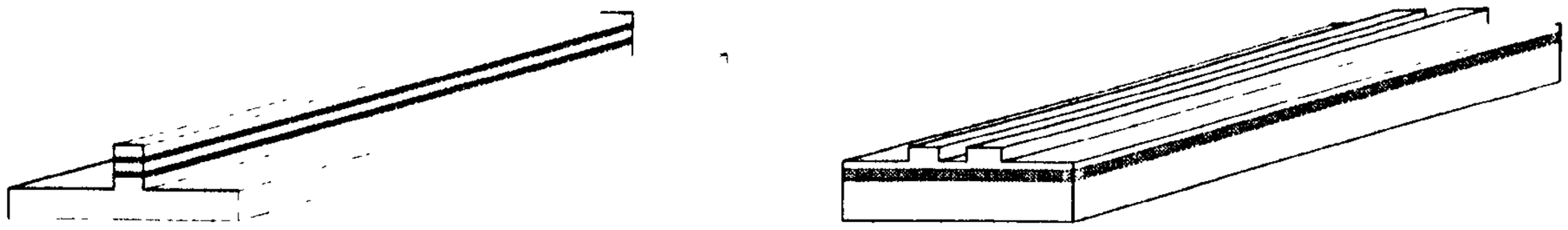

(a) Vertical coupler (b) Horizontal coupler

Figure 1.11: (a) Vertical and (b) horizontal waveguide couplers

the supermodes in the coupler. This means that only one active device is required for wavelength conversion, as is explained in chapter 4, which gives this structure advantages over the Mach-Zehnder structure. High extinction ratio can be achieved in the AVC as the input power is split between the super modes automatically by the input excitation. This distribution means that one of the output ports can be tuned to have very low output power by adjusting the gain and length of the AVC. An AVC structure allows the active and passive waveguides to be placed very close to each other with great accuracy, which is required to form directional couplers of reasonable lengths. No other coupler orientation can achieve the same accuracy. The vertical alignment of the waveguides allows the design of optical integrated circuits with arrays or matrixes of devices connected by passive waveguides.

1.6. Scope

This introduction chapter has given the background information in optical networking that leads up to the research in this thesis. In the following two chapters a simulation is presented and validated for any multiple waveguide structure containing a single active waveguide. The specific aim of this simulation is to model the non-linear saturation behaviour of an active optical waveguide whilst coupling occurs between this waveguide and others.

Chapter 4 details the design of an all-optical wavelength converter using the simulation with the aim of completely validating the simulation.

The fabrication processes and research are discussed in chapters 5 and 6 which lead to the completion of two rounds of devices with differing masks. These devices are characterised and their results discussed in chapter 7.

Chapter 8 details the conclusions and future work discovered and planned during

the research for this thesis.

Chapter 2

Active vertical coupler simulation

In this chapter the operation of the active vertical coupler structure (AVC), shown in figure 2.1, is discussed and the development of a model to predict its behaviour is explained.

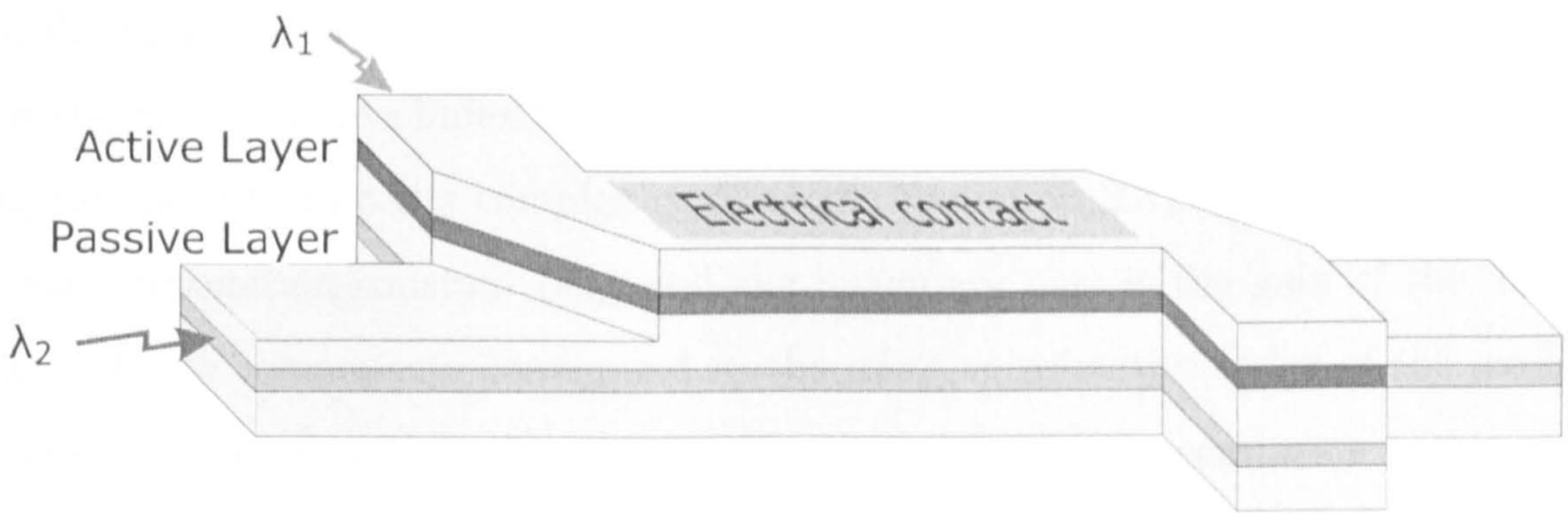

Figure 2.1: Active vertical coupler as a wavelength converter

2.1. Theory of operation

The active vertical coupler (AVC) structure is designed to take advantage of two mechanisms to enable operations such as wavelength conversion and pulse reshaping. These mechanisms are cross phase modulation and cross gain modulation. The model's initial aim was to simulate these mechanisms that are both controlled by the carrier concentration change due to the light intensity in the waveguide. This change occurs due to the saturation of the free carriers in the active region. The rate equation is used to simulate the carrier concentration change as discussed in section 2.5.6.

2.1.1. Cross gain modulation

$$E_{m,z} = E_{0,m}e^{-j\beta_m z} \tag{2.1}$$

$$\beta_m = \frac{2\pi n_{eff,m}}{\lambda} \tag{2.2}$$

$$\beta_m = k_m + jg_m \tag{2.3}$$

$$n_{eff,m} = n_{re,m} + jn_{im,m} \tag{2.4}$$

The propagation equation shown in equation 2.1 shows that the amplitude of the light (E) in each mode, m, at a distance z in the direction of propagation depends on the propagation parameter β_m. This parameter can be defined as a function of the effective refractive index for the mode (n_{eff}) and the wavelength of the light (λ). β_m can be split into it's complex components (equation 2.3), where the real part is the propagation constant (k_m) and the imaginary part is the gain of the mode (g_m). These components correspond to the effective refractive index of the mode, where both parts are functions of wavelength and carrier concentration within the waveguide material. The real part of the refractive index (n_{re}) can be modelled as a polynomial in carrier concentration (N) where the polynomial coefficients are x, y and z. The imaginary part can be modelled as a linear function above the transparency carrier concentration (N_{tr}). These are shown in equations 2.5 to 2.8.

$$k = 2\pi n_{re} \tag{2.5}$$

$$= 2\pi(xN^2 + yN + z) \tag{2.6}$$

$$g = 2\pi n_{im} \tag{2.7}$$

$$= 2\pi g_0(N - N_{tr}) \tag{2.8}$$

The gain of an optical amplifier reduces if there is high light intensity within the amplifier, due to the saturation of free carriers. It can be seen from equations 2.8 and 2.10 that a high carrier concentration within a material causes a larger gain and therefore a larger magnitude of the propagating mode (equation 2.11). The rate equation is shown in equation 2.13 where J is the injected current density, e is the charge on an electron and A, B and C are the recombination coefficients that can

be found in literature for a certain material. In the steady state, with only a small light intensity in all modes (I), the carrier concentration (N) will find an equilibrium where $\frac{dN}{dt} = 0$. If one or more modes were to have a high intensity $\frac{dN}{dt}$ would be negative and the carrier concentration (N) would reduce to a new equilibrium. This occurs due to free carriers being consumed by stimulated emission. Equations 2.8 and 2.10 show that a lower carrier concentration will cause a lower gain and therefore lower optical intensity after propagation.

$$E_{m,z} = E_{0,m} e^{\frac{-2\pi}{\lambda} z j (k_m + j g_m)} \tag{2.9}$$

$$= E_{0,m} e^{\frac{2\pi g_m}{\lambda} z} e^{\frac{-2\pi k_m}{\lambda} z j} \tag{2.10}$$

$$|E_{m,z}| = E_{0,m} e^{\frac{2\pi g_m}{\lambda} z} \tag{2.11}$$

$$\angle E_{m,z} = \frac{-2\pi g_m}{\lambda} z \ rad \tag{2.12}$$

$$\frac{dN}{dt} = \frac{J}{eD_{act}} - N(A + BN + CN^2) - \sum_{m=1}^{modes} [g_m I_m] \tag{2.13}$$

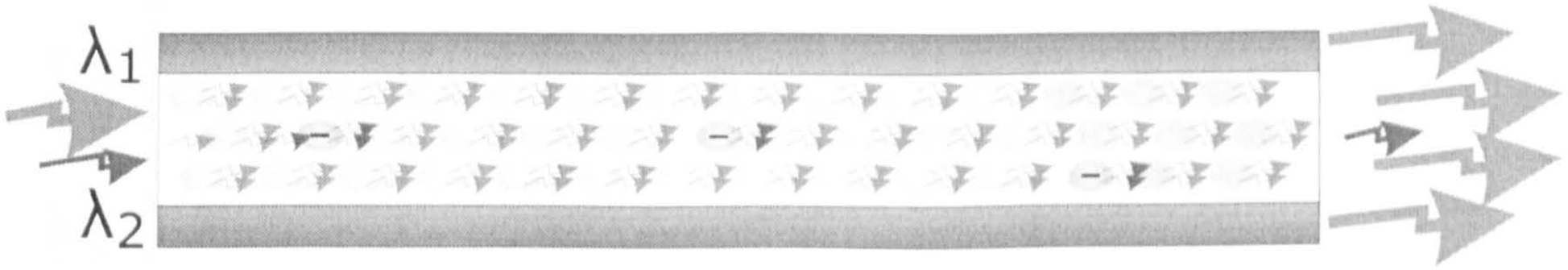

Figure 2.2: Saturated active region. The high power pump signal (λ_1) uses up a large proportion of the free carriers (represented by the ellipses) by stimulated emission. This leaves the probe signal (λ_2) few free carriers to cause stimulated emission, so the probe is only slightly amplified.

Figure 2.2 is a diagram showing how this occurs with a large intensity pump signal. If there was only one high intensity signal in the amplifier, the amplifier would saturate and the gain would be minimal. This means that if a second signal with an alternative wavelength is applied, little amplification will occur. This means that the second signal is at an off state at the output (see Figure 2.3) when the first signal is in the on state.

If the first signal is at a very low power (in the off state), the carrier concentration will remain high and the second signal will be amplified as normal and will have a

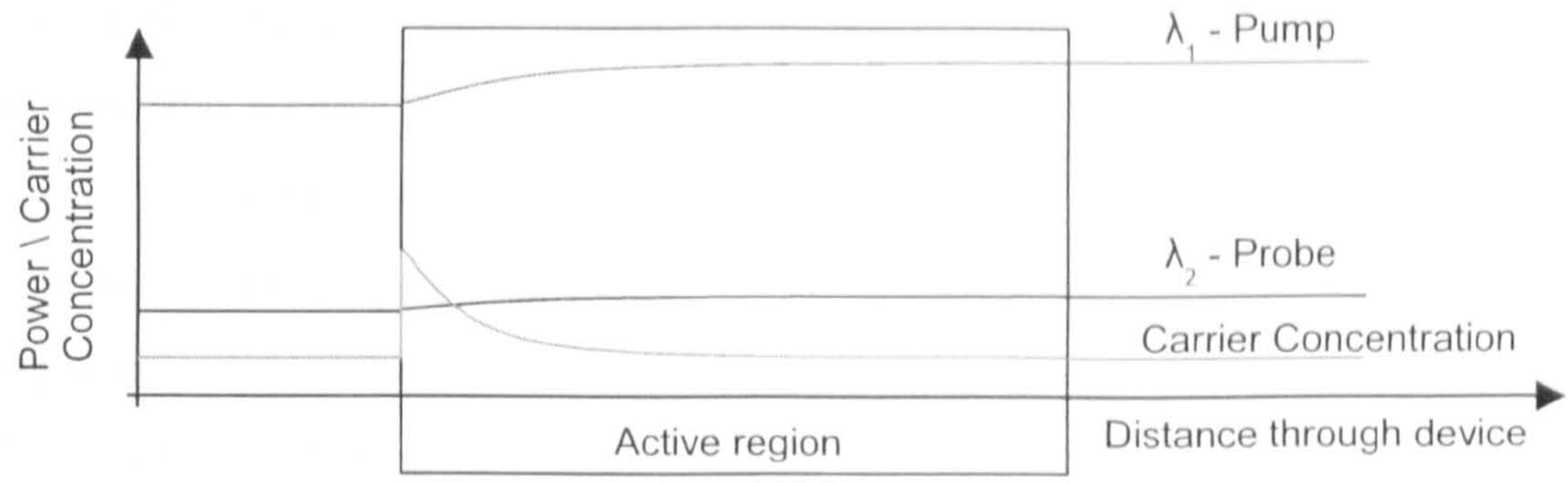

Figure 2.3: Saturated optical amplifier

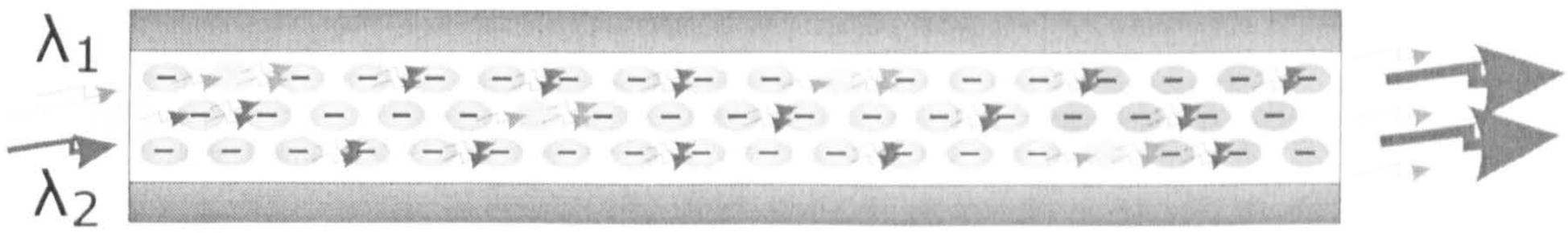

Figure 2.4: Unsaturated active region. The low power pump signal (λ_1) uses up a few of the free carriers (represented by the ellipses) by stimulated emission. This leaves the probe signal (λ_2) many free carriers to cause stimulated emission, so the probe signal is amplified to give a high output.

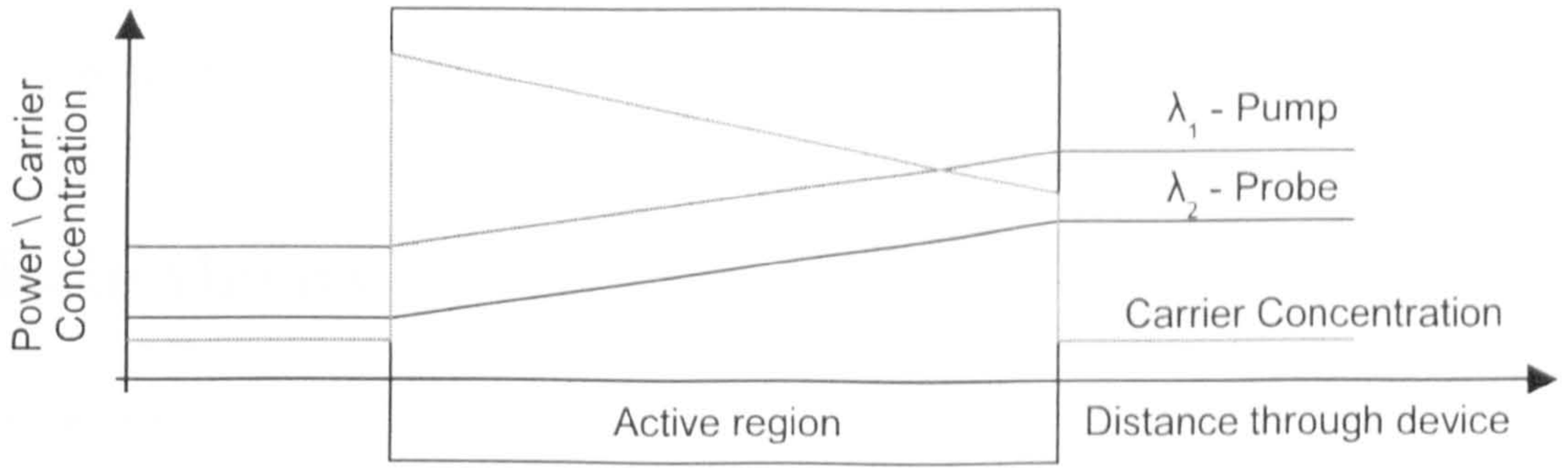

Figure 2.5: Unsaturated optical amplifer

high output intensity, the on state (see Figure 2.4 and Figure 2.5). If the first signal has data modulated on one wavelength and the second signal has constant power and a constant alternative wavelength, then the device described is a wavelength converter.

2.1.2. Cross phase modulation

Cross-phase modulation is another wavelength conversion mechanism. Using Figure 2.6 as an example, λ_1 applies the modulation to λ_2 which will then contain the data at the output. A high power λ_1 will saturate the active section of the device by

reducing the number of free carriers as shown in equation 2.13. Equations 2.6 and 2.5 show that a change in carrier concentration alters the propagation constant. It can be seen in equations 2.10 and 2.12 that a change in k will cause a change in the phase of the propagating mode. As λ_2 is split into two paths and only one of the paths is active, constructive or destructive interference will occur when the two paths rejoin, depending on the modulation applied. This transfers the data from λ_1 to λ_2.

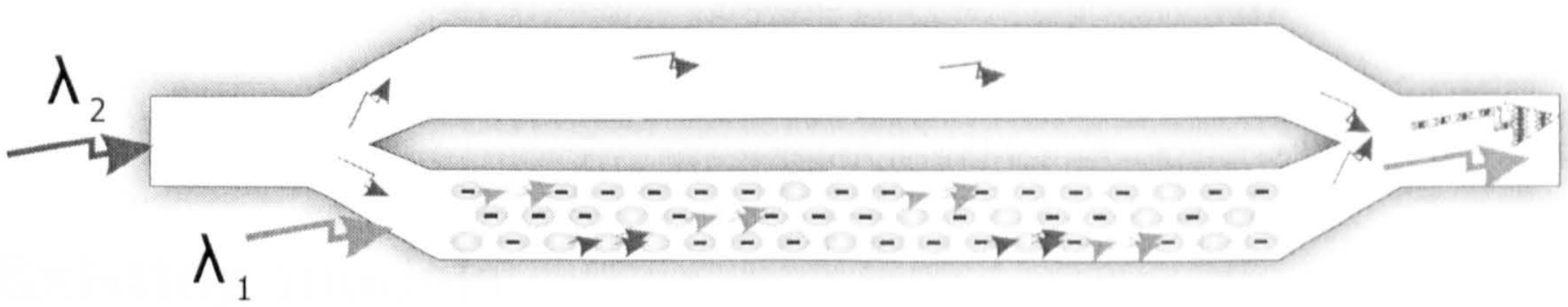

Figure 2.6: Cross phase modulation. A high power pump signal (λ_1) will saturate the active region, leaving few free carriers (represented by the ellipses). This reduces the gain of the active region and increases the refractive index. The change in index causes an altered optical path length for the probe signal (λ_2) thereby causing interference to occur.

2.2. Mode theory

The active vertical coupler structure, shown in Figure 2.1, supports one symmetric and one anti-symmetric super mode. The modes of a waveguide are the possible patterns that a certain wavelength of light can form in a waveguide. These two super modes propagate at different speeds due to the different material properties in the device. This means that the output at any port will depend on the interference between the two modes. This causes a coupling effect between the waveguides that can be seen in Figure 2.7.

The combination of the coupler and both the cross-phase and the cross-gain modulation mechanisms can produce efficient wavelength conversion and other applications. This combination means that a greater output extinction ratio can be achieved than with either mechanism on its own.

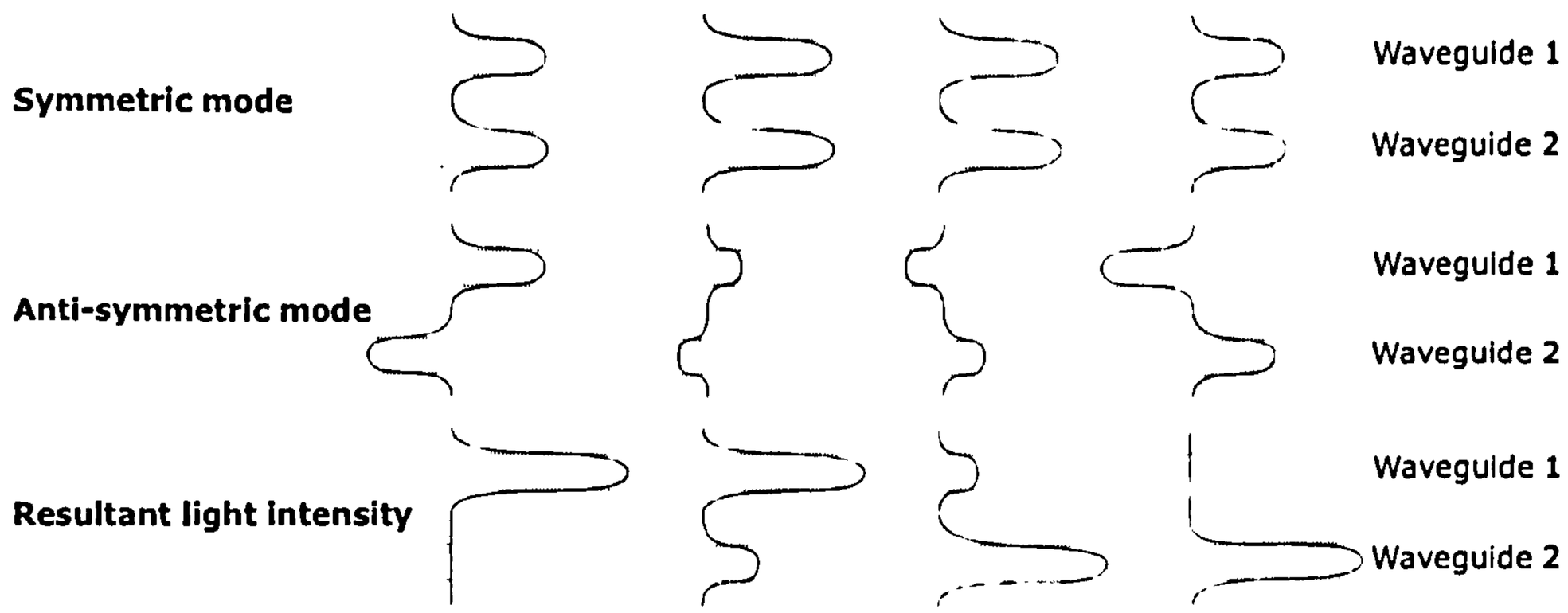

Figure 2.7: Waveguide coupling effect

2.3. Existing models

There are some methods available that can be used to model similar structures to the active vertical coupler. However, none of these can take into account all of the mechanisms described above. An amplifier could be modelled using travelling wave theory [33], where cross gain, cross phase and amplified spontaneous emission can be accounted and no complex mode solving would be required. However this only applies to devices with a single mode as it does not take into account the interaction of multiple waveguides.

The model explained in [29] is for a similar situation to the active vertical coupler. However, it uses only weakly coupling waveguides so the coupling equations can be used independently from the propagation and carrier concentration equations.

2.4. Initial implementation

To take account of the saturation effect in the active layer using the rate equation, an implementation was required that could be used to extract the light intensity within the active layer. This could then be used to calculate the carrier concentration at that position. Analytical methods for propagating light in waveguide structures are specific to a given structure. The requirements in this case ruled a purely analytical method out as the waveguide structure needed to be optimised. A finite difference time domain (FDTD) method could be used to recalculate the carrier concentration at every mesh point. However, this is not a trivial problem to incorporate into FDTD

software and rerunning the simulation for many different input power levels would take a very long time. The best implementation method found was to use a mode solving and propagation tool. For each waveguide structure the propagating modes can be found for given carrier concentrations. Once modes are found, propagation of the light does not require much calculations and it is simple to calculate the average light intensity in a given cross section of the mode.

2.4.1. Mode solving

This simulation uses the super modes of the directional coupler to propagate light through the device. This method means that the model is very general and can be used for any structure, with some limitations due to calculation complexity. The super modes of a structure are simply the propagating modes in a coupler structure. These are distinct from the waveguide modes which are the modes in a single waveguide, not in a coupler. This nomenclature is used in coupled mode theory which is only an approximation to the real situation. The conversion into and out of waveguide modes is completed in this simulation by finding the overlap integral at the inputs and outputs of the device where the waveguides are split. A structure's modes can be calculated as the eigenmodes of Maxwell's equations in the frequency domain. The eigenvalues of these eigenmodes are the propagation constants, k, which are proportional to the effective refractive index, n_{eff}, and gain or loss of the modes by the relationship shown in equation 2.14.

$$k_{re} + jk_{im} = 2\pi(n_{eff,re} + jn_{eff,im}) \tag{2.14}$$

This means that it is simple to propagate the light in these modes using the propagation equation (equation 2.1 and the gain and phase information is preserved. The disadvantage of using mode solving is that wherever the waveguide cross section changes, the modes will change shape and an overlap integral must be performed to calculate the power in the new modes. However, this allows the interference between the changing relative phase of the modes to be evaluated, which completes the model of a coupler.

2.4.2. Fimmwave

Fimmwave is an optical component simulation software. It finds the modes that can propagate along the z-axis of a cross-section of a waveguide. It will then propagate these modes in the z-direction accounting for discontinuities where the cross-section changes by carrying out the overlap integral calculations using the FimmProp module. The main limitation of Fimmwave is that it can not model devices where saturation occurs.

The first version of the model established in this work created complete Fimmwave components where the device was split up into sections in the z direction. Each end of the simulated device had probes attached that mimicked the effect of totally internally reflecting (TIR) mirrors separating the passive and active waveguides. These probes were swapped to simulate the different inputs and outputs available from the device.

2.4.3. Steady state saturation

To simulate the carrier concentration change with high optical power levels, the device was broken up into short sections in the z direction and placed together within Fimmwave. These sections are assumed to have constant carrier concentration so that the carrier concentration in each section is related to the light intensity at the middle of the section by the rate equation, which is explained more fully in section 2.5.6. The basic design of this simulation is similar to reference [12], however multiple modes can be propagated. All of the inputs to the device are assumed to be on independent wavelengths and will only affect each other by altering the total light intensity in the waveguide, which will therefore alter the carrier concentration. It is this change in carrier concentration that causes the alteration in material gain and phase change over a given length due to the eigenmodes changing. There is an additional feedback problem in this situation; when the carrier concentration is changed to be consistent with the light intensity in the active waveguide, the propagation of the light is altered so the light intensity is changed. This non-linear feedback problem was solved using an iterative technique as an analytical method was not possible due to the numerical solution to the propagation.

2.4.4. Automated implementation

To implement this simulation in code, Microsoft Visual C++ 6.0 was chosen for speed of execution and flexibility in communicating with Fimmwave. Fimmwave can be started with the command line parameter, "-pt ¡port¿", where the port is the TCP/IP port that Fimmwave will listen to for connections from other programmes. A class was written that would send and receive command and return strings to and from Fimmwave. It was coded so that the programme can continue with other operations until the reply is received when an interrupt is triggered.

2.4.5. Limitations

This implementation was very slow as after every iteration in a section, Fimmwave needed to recalculate the overlap integral on each side of the section. The University of Bristol only had two licences for Fimmwave so there was only a very limited scope for parallel processing. There is no method to introduce a distributed power source within Fimmwave so spontaneous emission can not be modelled. This is a serious limitation as when dealing with devices in saturation, they will tend to be long and have high gains causing the amplified spontaneous emission (ASE) to have a noticeable affect.

2.5. Second implementation

To overcome the limitations of the first implementation the method adopted was to only use Fimmwave to find all transfer functions that connect pairs of sections with all carrier concentrations in the range that may occur in the device. These transfer functions can then be used one at a time to recalculate the propagation of the light from one section to the next, quickly swapping transfer functions as the carrier concentration is changed. This additionally meant that once all possible transfer functions had been found and recorded for a given structure and wavelength, the simulation could be run independently from Fimmwave, thereby allowing parallel processing and freeing up the limited number of licences within the research group.

2.5.1. Wavelength Dependance

To model the device more accurately the response of the device to different wavelengths needed to be incorporated. The reciprocal function shown below is used to simulate the wavelength dependence of the gain (g) of a waveguide as used in [32].

$$g(\lambda, N) = a_1(N - N_0)\left(1 - \left(\frac{\frac{c}{\lambda} - \frac{c}{\lambda_{gap}}}{C_v(N - N_0)} - 1\right)^2\right)$$

Where $a_1(N - N_0)$ is the linear approximation to gain with carrier concentration, N, c is the speed of light in vacuum, λ_{gap} is the band gap of the material and C_v is a constant that defines the rate of change of the reciprocal function. Reference [36] gives C_v as $6.4 \times 10^6 Hzcm^3$.

2.5.2. Amplified spontaneous emission

Modelling amplified spontaneous emission (ASE) requires spontaneous emission (SE) to be calculated and included in the simulation at every point in the active region of the device. This is simplified by assuming that the total spontaneous emission power occurs at a single wavelength and that the total spontaneous emission occurring in a device section is added to the simulation at the centre of the section. The fact that the SE is a distributed light source throughout the device required the change in implementation explained in this section. Once the SE has been calculated and added to each mode in each direction, its propagation can be simulated as if it was a separate input. There are many published methods for calculating the spontaneous emission that is within the active region, then the proportion that is coupled into the guided modes [33] [37] [7] [32] [12] [5] [28]. The most suitable method is a combination of the equation for noise power spectral density (W_{se}) taken from [19] and the equation for noise coupling into guided modes (β) from [28].

$$W_{se} = 2h\nu\Gamma g(N, \lambda) n_{sp}(N, \lambda) \tag{2.15}$$

Where h is Plank's constant, ν is the frequency of the light, Γ is the confinement factor, $g(N, \lambda)$ is the gain of the mode, which is a function of the carrier concentration and the wavelength, and $n_{sp}(N, \lambda)$ is the inversion factor, which is also a function of the carrier concentration and the wavelength.

$$\nu = \frac{c}{\lambda} \tag{2.16}$$

The multiple of two in equation 2.15 is to include the coupling into both transverse electrical (TE) and transverse magnetic (TM) modes.

$$\beta = \frac{1}{4}\frac{\lambda^2\Gamma}{\pi^2 n_{re}^2 A_{act}} \tag{2.17}$$

Where λ is the wavelength of the SE, Γ is the confinement factor of the mode in question, n_{re} is the real part of the effective refractive index of the mode and A_{act} is the cross-sectional area of the active pumped region.

The noise power spectral density is integrated over the gain spectrum and assumed to behave as though all the SE has a wavelength equal to the peak of the gain spectrum [32]. This means that the wavelength in equation 2.17 can be approximated as the peak of the gain spectrum. β from equation 2.17 is used instead of Γ in 2.15 to make the coupled power more accurate. The multiple of two has been removed as the TE and TM modes are treated separately in this simulation. Therefore the light intensity coupled into the mode m in one direction is given by I_m.

$$I_m = \frac{\delta z h c}{\lambda}\beta_m n_{sp}\int g(N,\lambda)d\lambda \tag{2.18}$$

$$\beta_m = \frac{1}{4}\frac{\lambda^2\Gamma_m}{\pi^2 n_{re,m}^2 A_{act}} \tag{2.19}$$

n_{sp} is normally calculated from the Fermi level of the junction or by an approximation to this [35] [35] [30] as the spontaneous emission is due to spontaneous recombination of carriers. In this simulation there is a parameter that is already being used for the spontaneous recombination of carriers which is BN^2 in the rate equation. Therefore the only extra action that is required is an adjustment to take account of the fact that the spontaneous emission spectra is different to the gain spectra and that the whole of the amplified spontaneous emission is being propagated at a single wavelength. This new spontaneous emission factor will be referred to as n'_{sp} and will be found by comparing measured results with the simulated results.

$$I_m = \frac{\delta z h c}{\lambda}\beta_m B N^2 n'_{sp}\int g(N,\lambda)d\lambda \tag{2.20}$$

$$\beta_m = \frac{1}{4}\frac{\lambda^2\Gamma_m}{\pi^2 n_{re,m}^2 A_{act}} \tag{2.21}$$

2.5.3. Dynamic Simulation

Modelling the dynamic response of the device requires more effects to be modelled. The first of these is to take account of the time constants that are in the rate equation. That is done by using the rate equation in its $\frac{dN}{dt}$ form to calculate the change in carrier density and assuming that the time step used is small enough that the answer will be accurate. The other dynamic effect that has been incorporated into the simulation is the propagation delay. Unfortunately the light is travelling through different materials with slightly different refractive indices so the propagation delay of the light depends on the path that it takes. However to simplify the model, it is assumed that the light is travelling at a constant speed in the device of c/n, where n is the bulk refractive index in the device. This simplification is justified as the differences in refractive indices are very small and any phase changes that they would cause are already accounted for in the transfer functions used in propagation of the modes. The propagation delay is modelled by delaying the change in light intensity in neighbouring sections by the time step. The time step is calculated from the device section length and the speed of light in the material, $T = \delta z n_{eff}/c$, so that the propagation delay between sections is correct.

2.5.4. Simulation Organisation

The model was designed to be as modular and flexible as possible. The actual commands to send to Fimmwave are all in one header file, to allow for changes to commands in more recent and future versions of Fimmwave above version 3.41, which was used for this simulation. Commands or functions that must wait to be executed or completed are all added to a function tree, where the first branch is always executed first (see figure 2.8). Where there is a scanner loop occurring, the branches are just disabled when they have executed and when the loop restarts, all the branches are enabled again (see figure 2.9). The settings required to begin a simulation are set on a group of property sheets and these settings can be saved and reloaded at a later date. A log file was used during writing and debugging of the simulation and can still be used if required.

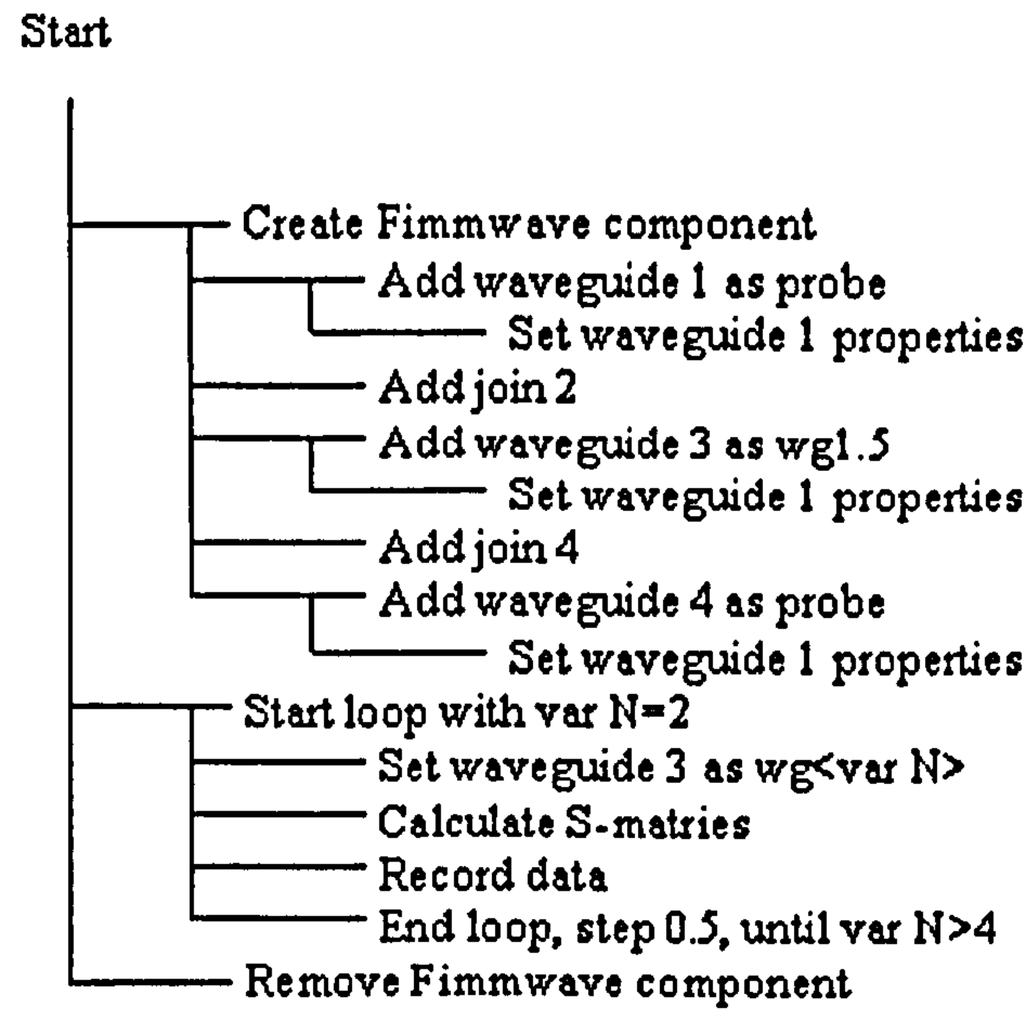

Figure 2.8: Function tree diagram

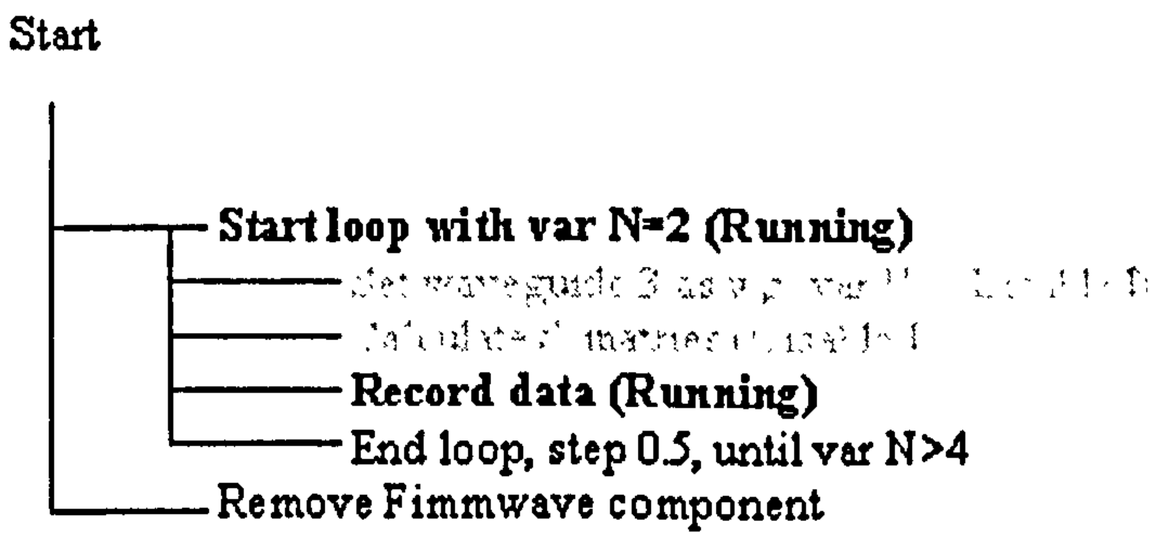

Figure 2.9: Looping in the function tree

2.5.5. Simulation Setup

Before the simulation can start there are a few steps that must be completed. The structure of the device must be created in Fimmwave where the carrier concentration in the active region is at transparency. The modes of interest must then be found at every wavelength that is required, where each wavelength is a different file. Probes that separate the waveguides must also be created for every wavelength. These probes are the same structure as the main part of the device but Indium Phosphide (InP) replaces the waveguides that are not of interest as shown in figure 2.10. The probes are used to approximate the different outputs available when the waveguides are split using a TIR mirror.

There is a function in the simulation program that copies all of these files from

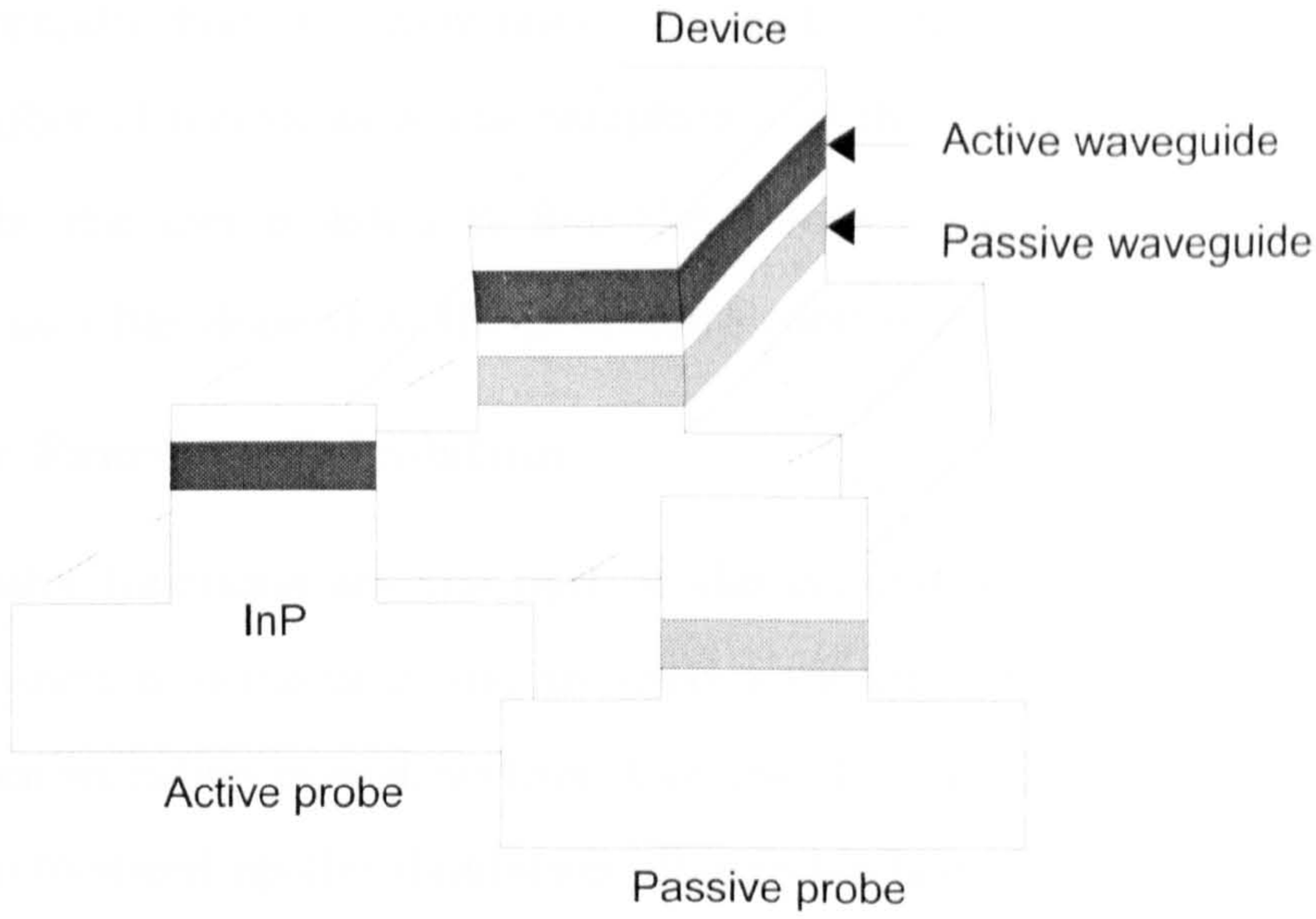

Figure 2.10: Waveguide probes

another directory, changes a specified value and attempts to find the modes again. This speeds up the initial stage of setting up the simulation. Once these files have been created there is a waveguide creation function in the simulation program that takes the waveguide section at transparency and creates all the other waveguides required at all the different carrier concentrations. User intervention is sometimes required when Fimmwave can not find the modes automatically due to the modes in a new waveguide being too different to the previous one. Once all of these have been created successfully the simulation program can be used to find all the transfer functions from all the possible combinations of the waveguides.

Waveguide File Creation

To create the waveguide files with all of the different carrier concentrations the waveguide at transparency is used as a template. The previous waveguide produced (at the beginning this is the template waveguide) is first of all copied to the new filename within Fimmwave, which also copies all of the mode data. The template file is then altered according to the "find and replace" settings from the simulation setup file. This sets the new carrier concentration and is then saved over the new waveguide file. This new waveguide file is then loaded in Fimmwave and the modes are fine tuned (polished) to the new structure. This method works reasonably well as there is only a small change between consecutive waveguides, so polishing the old

modes normally finds the new ones. A check is performed to see if there are the same number of modes as in the template and that they are all TE modes. If this check fails, the user is asked to find the modes manually for that waveguide and once the user has done this, the procedure continues.

Transfer Function Calculation

The transfer functions are the part of the simulation that propagates the modes from one section to the next and are used many times in the iteration that finds the carrier concentration in each section. Getting the transfer functions from Fimmwave is slow, so to speed up the simulation all possible transfer functions are found before the main simulation and are stored in a text file so that they can be loaded when required by the main simulation. The simulation can also work in a different mode where Fimmwave is only queried for a transfer function if it has not been used before, but this requires the main simulation to be running on the same computer as Fimmwave, so is not desirable unless only one simulation is required. For every possible transition from one section to another a device is created in Fimmwave where one section is joined by a simple join to the other one. Both section lengths are half of the defined longitudinal step size, so that the device represents changing from the centre of one section to the centre of the other section (see figure 2.11. The only exception to this is where one of the sections is a probe, where in this case the probe is given a length of zero so that simulated measurements are taken directly from the ends of the coupler. The "S-Parameters" of the device can then be extracted from Fimmwave and recorded. The number of modes, the effective refractive index of the modes and their filling factors are recorded at the same time, as these are also to be used in the simulation.

2.5.6. Saturation Simulation

The root of the simulation is the iteration loop where the carrier density is found that corresponds to the light intensity in a particular section. This is found from the steady state result of the rate equation. The rate equation adjusted for this case

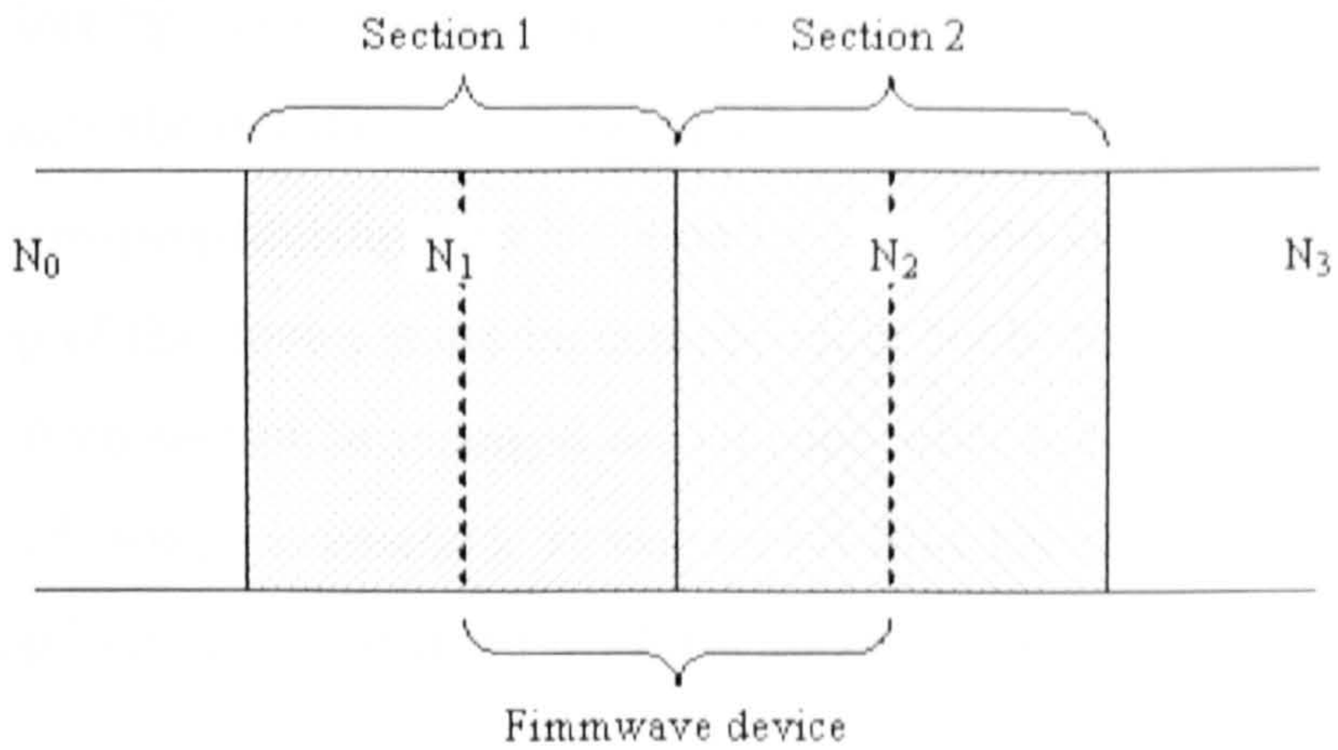

Figure 2.11: Finding transfer functions within Fimmwave

is shown below.

$$\frac{dN}{dt} = \frac{J}{eD_{act}} - N(A + BN + CN^2) - \sum_{i=1}^{ninputs} \left[\frac{dg}{dn}(N - N_{tr}(\lambda_i))\Lambda_i I_i \right] \tag{2.22}$$

Where,

$$\Lambda_i = \left(1 - \left(\frac{\omega_i - \omega_{gap}}{2\pi C_v (N - N_{tr}(\lambda_i))} \right)^2 \right) \tag{2.23}$$

$$I_i = \frac{P_{act,i}}{A_{act} h \omega_i} \tag{2.24}$$

It can be seen that this takes into account all of the light intensities in all the modes at all the significant wavelengths within the active region. The iteration begins at the previous carrier concentration for this section, or transparency if it is the first iteration. Transfer functions are then used to propagate the mode powers into this section from the neighbouring sections for both the forward and the backward directions at all of the wavelengths required. The $\frac{dN}{dt}$ value is then calculated from the equation shown above, which is then used to give the value of carrier concentration for the next iteration. Unfortunately the transfer functions are only applicable to discreet values of carrier concentration, so the new value of carrier concentration must be rounded to the nearest discreet value. This can cause infinite loops, as the exact carrier concentration can never be found. A loop is detected when the carrier concentration iteration sets the carrier concentration to a value that has already been tested. When this occurs the iteration is stopped and all values of carrier concentration within the extremes of the loop are tested and the carrier concentration

with the smallest $\frac{dN}{dt}$ is used. Only one section at a time can be iterated, so to find all of the sections the iteration must sweep along the length of the device. To allow inputs in counter-propagating directions and a complete two-way simulation of the ASE the sweep of the device must be completed in both directions. The sweeps are continued until no section is changed or, to cope with infinite loops, until a maximum number of sweeps is reached. It was found that the simulation rarely fell into an infinite loop here and that a value above 16 sweeps would ensue accuracy.

2.5.7. Dynamic Simulation

Implementing the dynamic part of the simulation requires the simulation to continue after the steady state device has been completed. The dN/dt is found at each time step throughout the device using the delayed propagated mode powers from the sections on either side of the section being calculated to give the light intensity. Once the dN/dt is found, a new accurate value for N is calculated and recorded, ready to be used in the dN/dt calculation in the next time step. A rounded value of N is then used for propagating the light in the next time step. The new value of N is not used for any calculations until the next time step.

2.5.8. Performance Improvements

Scan Properties

Automation of the simulation was required so that the simulation could be left running without user intervention for a long period of time. This allows multiple long simulations to be run overnight or at the weekends. The automation was implemented by allowing running of simple script files that gave commands as if the user was using the graphical interface. The script files also allow simple "for loops" which means that repetitive commands can be simplified into a loop.

Distributed Computing

Condor is the distributed computing system that runs in the Electrical and Electronic Engineering department at the University of Bristol. It allows long tasks that can be broken down into many small tasks to be spread around idle computers in the department so that they can all be executed at the same time. The first

parts of the simulation cannot be assisted by the use of distributed computing as they require the use of Fimmwave which the University only has a limited number of licences. Therefore the transfer functions must be found using a computer that has Fimmwave installed. Once the transfer functions have been found, the simulation can be split up into many small tasks and executed by Condor. To allow this the simulation software was converted to a console application and all references to Fimmwave were removed. Also, command line parameters were used to load the properties for the simulation and change certain values in the property file when it was loaded to allow simple calls to create the condor instances.

Chapter 3

Validating the simulation

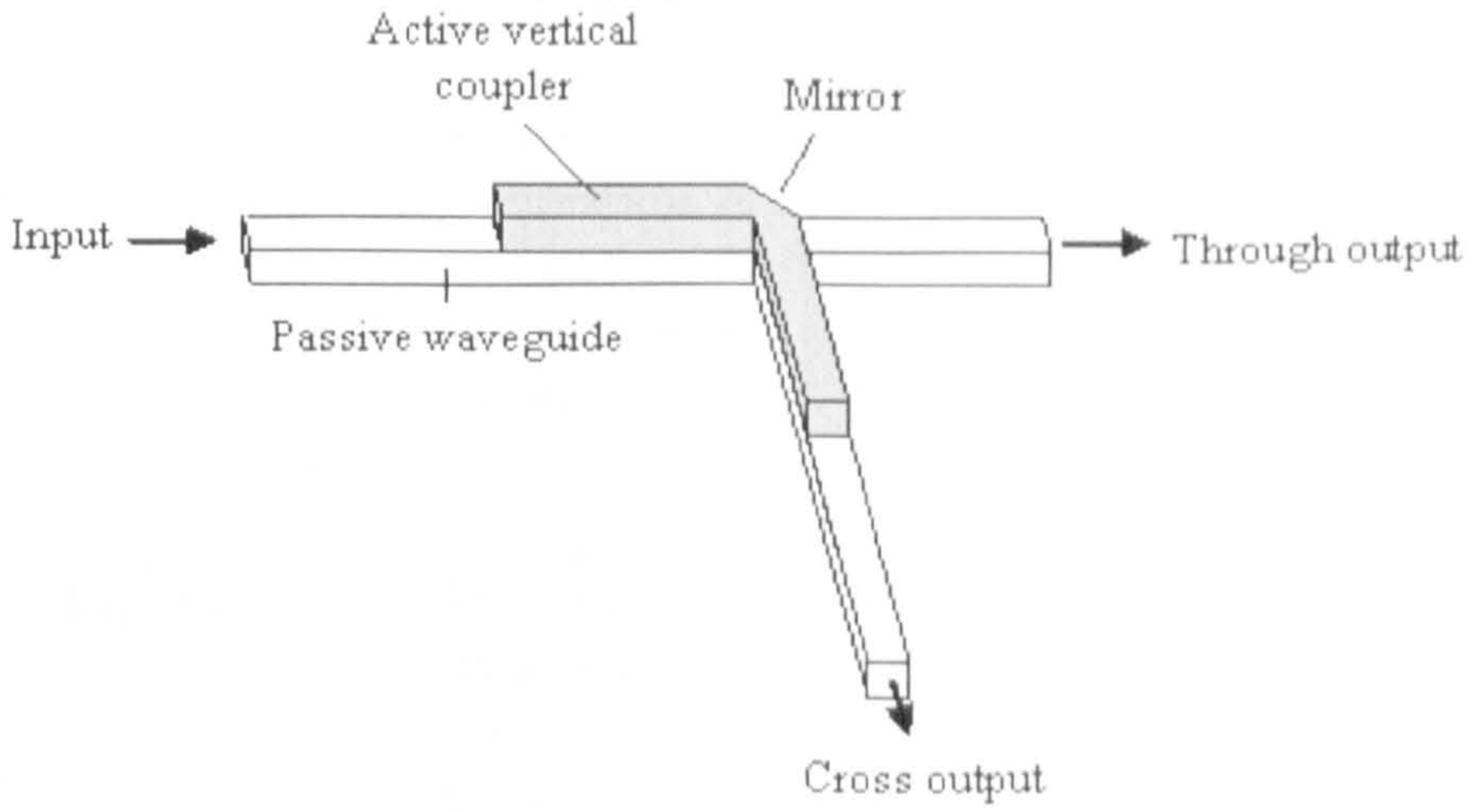

Figure 3.1: Crosspoint device using an active vertical coupler structure

Much work has been done on an optical crosspoint switch in the photonics group at the University of Bristol [42] [38] depicted in figure 3.1. This device is implemented using an AVC structure, so it was a good device to validate the model. This is particularly important for validating the amplified spontaneous emission calculations as much signal to noise ratio has been gathered for these devices.

3.1. Simulation properties

The material and device properties used in the crosspoint simulation are shown in table 3.1. The description and explanation for the properties are described below.

The device length is taken to be the length of half a single crosspoint. This will simulate half of the active vertical coupler structure and needs to be split in two at this point as there is a TIR mirror through just the active waveguide that can not be simulated within a single simulation.

Group	Property	Value	Unit
Device	Device length	450	μm
	N number format	"%0.2e"	string
	N Step	5×10^{16}	cm^{-3}
	N Value	3×10^{18}	cm^{-3}
	Z Step	10	μm
	Max Sweeps	100	
	Probe 0	Active	
	Probe 1	Passive	
Waveguide	Active Depth	0.0525	μm
	Active X-Section	0.2625	μm^2
	Current Density	Varied	$KAcm^{-2}$
	$\frac{dG}{dN}$	2×10^{-16}	cm^2
	Transparency (N_0)	1.5×10^{18}	cm^{-3}
	Time constant A	1×10^{8}	s^{-1}
	Time constant B	1×10^{-10}	$cm^3 s^{-1}$
	Time constant C	5×10^{-29}	$cm^6 s^{-1}$
	Band gap	1600	nm
	C_v	6.4×10^{-6}	$Hzcm^{-3}$
	n'_{sp}	0.5	
Input 0	Direction	Forward	
	Power In	0.001	mW
	Probe	Passive/Active	
	Wavelength	1550	nm
Input 1	Direction	n/a	
	Power In	n/a	mW
	Probe	none - ASE	
	Wavelength	1550	nm

Table 3.1: Crosspoint simuation settings

The 'N number format' is a string using the C++ 'sprintf' number format specifiers that will correspond to the number format in the file names of the waveguides in the simulation.

The refractive index step (N step) was chosen by running simulations with varying step sizes. A value of 5×10^{16} was found to give good accuracy whilst not slowing the simulation too much. A refractive index value can be specified in case the values used do not pass through zero.

The longitudinal step size (z step) was also chosen by running simulations with varying step sizes and comparing the results. The value chosen was $10 \mu m$, that would ensure accuracy with devices as short as $200 \mu m$ whilst limiting the number of calculations required.

The property 'max sweeps' is used to limit the number of iterative loops the simulation goes through when sweeping backwards and forwards over the whole device. It is used to break out of any infinite loops. It was chosen to be 100 sweeps to ensure accuracy of the simulation.

The 'active depth' and 'active cross-section' are values taken from the physical structure of the device.

The injected current density is varied to cause different default carrier concentrations in the device.

The material properties, $\frac{dG}{dN}$, N_0, time constants and band gap were taken from previous simple Fimmwave simulations of the crosspoint material which had been validated against experimental results. The time constants were originally taken from reference .

The reciprocal wavelength function constant, C_v, was chosen to approximately match the gain spectrum of InGaAsP materials.

The new spontaneous emission factor, N'_{sp}, was found by running the simulation at different values and comparing the results to experimental measurements of ASE.

3.2. Single crosspoint

Figure 3.2 compares simulated and experimental results of the crosspoint device. The output measurements of a single device (a) were made at the first cross output and the pass though measurement needed to be transferred through the next crosspoint (b) to the second cross output. This setup is shown in figure 3.3, where the second crosspoint (b) is set to a fixed current. The simulation was split into the two halves of the crosspoint so that the whole device including the mirror could be modelled by simple equations. The simulation produces the results for gain from passive to active (G_{pa}) and passive to passive (G_{pp}) in the first half of the device. Active to passive gain is found in the second half of the crosspoint (G_{ap}). These data are all found for varying current density injection.

The whole device cross gain can be found by,

$$G_{cross} = G_{pa}(J)G_{ap}(J) \tag{3.1}$$

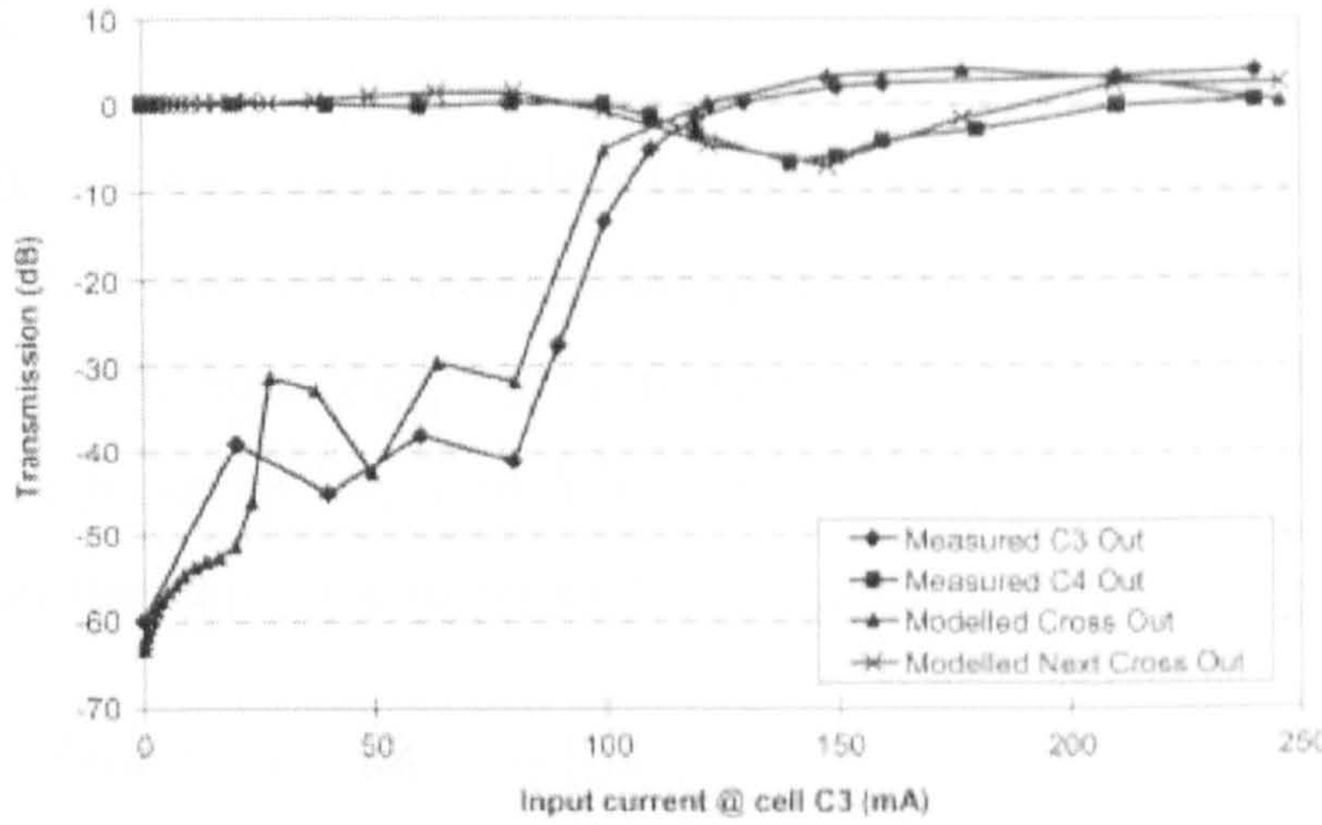

Figure 3.2: Experimental and simulated results of the cross and next cross out in a crosspoint [18]

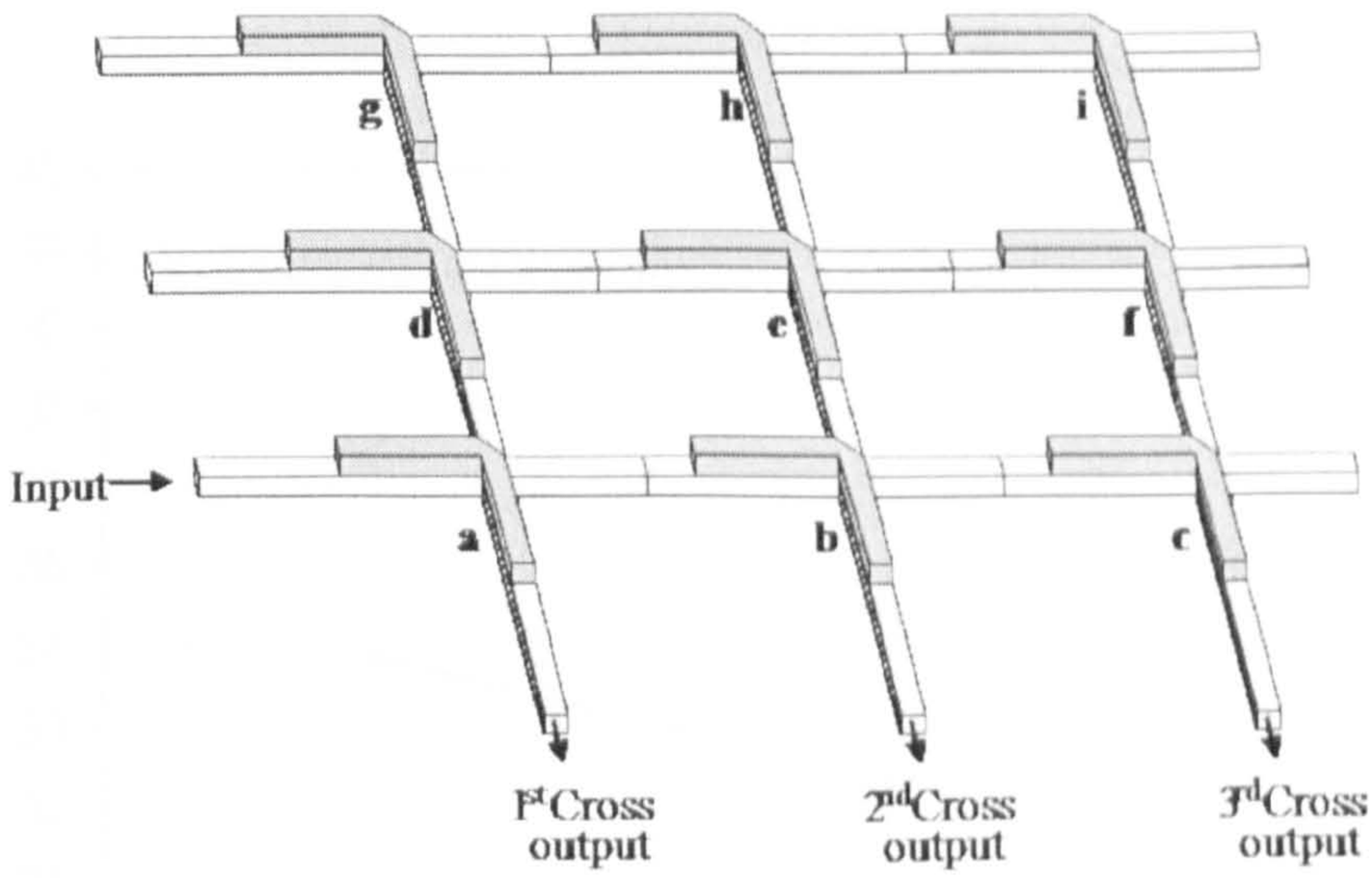

Figure 3.3: Single crosspoint test setup

The next cross gain is found by,

$$G_{next} = G_{pp}(J)G_{pa}(J_n)G_{ap}(J_n) \tag{3.2}$$

It can be seen that the comparison of the experimental and simulated results in figure 3.2 agree very well. This correlation gives good evidence that the simulation is calculating the transfer and coupling of the devce very well. The limitation of this experiment used only low input powers so did not test the saturation of the device.

3.3. Multicast

Multicast simulation was used to validate the ASE part of the simulation. Multicast is implemented by many crosspoints being positioned one after the other on the passive (pass through) waveguide. To calculate the gain at the cross output (G_x), gain at the through output (G_t) and ASE at the same places (ASE_x and ASE_t) for the n^{th} device in the multicast situation the following calculations were used.

$$G_{xn} = G_{t(n-1)}G_{pa}(J_n)G_{ap}(J_n) \tag{3.3}$$

$$G_{tn} = G_{t(n-1)}G_{pp}(J_n) \tag{3.4}$$

$$ASE_{xn} = ASE_{t(n-1)}G_{xn} + SE_{pa}(J_n)G_{ap}(J_n) + SE_{ap}(J_n) \tag{3.5}$$

$$ASE_{tn} = ASE_{t(n-1)}G_{tn} + SE_{pp}(J_n) \tag{3.6}$$

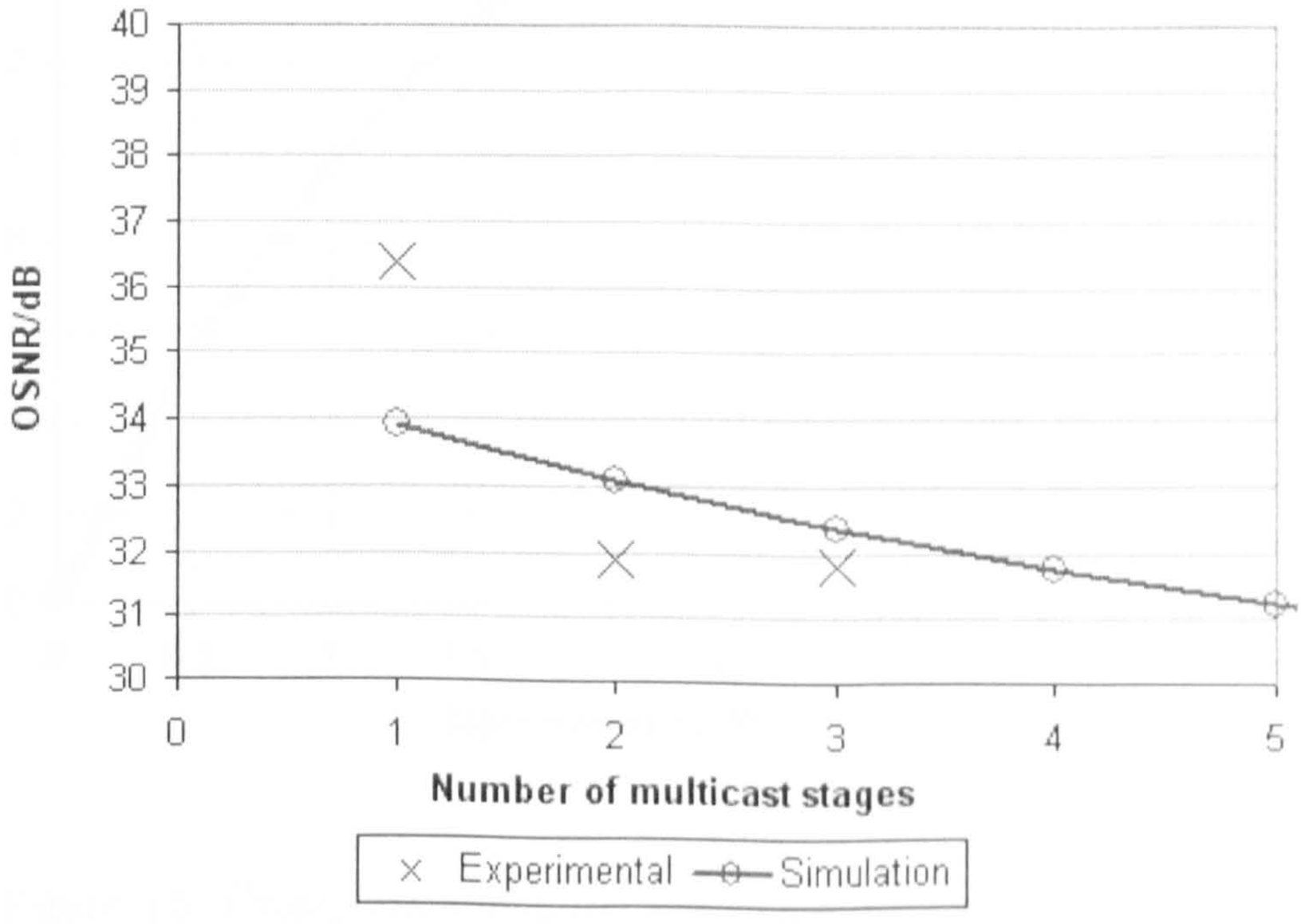

Figure 3.4: Multicast calculated and experimental OSNR with a measurement optical bandwidth of 0.1nm [41]

Each section has the previous section's ASE increased by it's gain and has it's own ASE added. The results of these calculations and some experimental results are shown in figure 3.4 where it can be seen that there is good agreement. The simulated results have had one loss coefficient that has been fitted to the data to account for the losses associated with the waveguides and input fibre coupling [18].

This gives confirmation of the ASE calculations within the simulation.

3.4. Saturation

The crosspoint simulation predicts the saturation of the device when the on-chip input power is approximately 5 dBm. Unfortunately with fibre coupling losses, these power levels can not be achieved in the lab. The closest experimental data is shown in figure 3.5 where the experimental data was used from reference [2] adjusted for coupling losses and the simulated data was calculated using the method explained in section 3.2

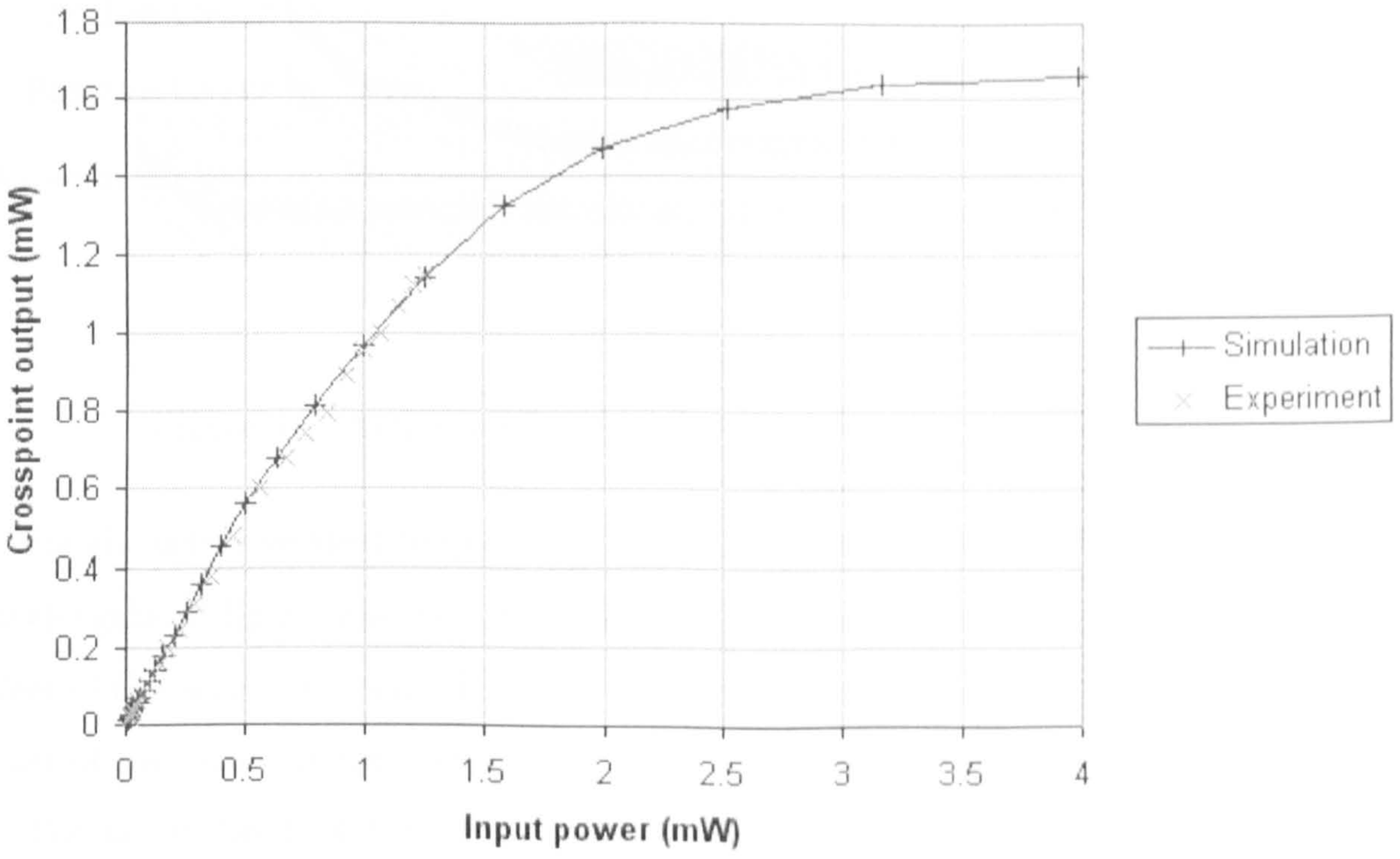

Figure 3.5: Crosspoint simulated and experimental saturation results

3.5. Conclusion

The simulation's predicted gain and ASE agree well with experimental results for steady-state unsaturated devices. Unfortunately, there is not enough data to draw firm conclusions about the accuracy of the saturated simulations.

Chapter 4

Wavelength Converter Design

4.1. Wavelength Converter Theory

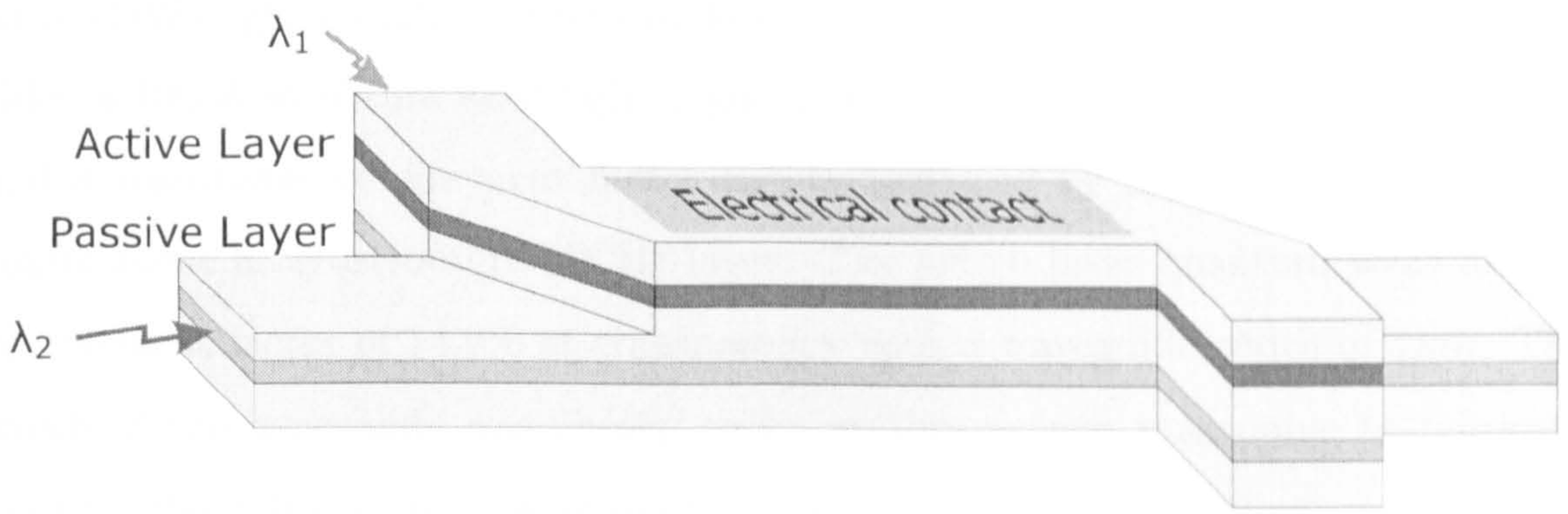

Figure 4.1: Active vertical coupler as a wavelength converter

For the active vertical coupler structure to be used in wavelength conversion two wavelengths of light must be input. These two wavelengths can be launched into either of the active or passive layers at either end. The λ_2 output can be taken from either of the layers at the opposite end of the device to the λ_2 input.

The active layer of the device operates using a number of quantum wells in the centre of the layer. The quantum wells are thin layers of material that trap free carriers to a much greater extent than the material around them due to the potential well effect. This means that any carriers nearby become concentrated in the quantum wells. As a result, this active layer has a greater gain and therefore non-linear effect than one without quantum wells.

The operation of the device as a wavelength converter is achieved by placing one high power pump wavelength with amplitude modulated data into the device (shown as λ_1 in figure 4.1). This pump will alternately saturate the active layer when there is an optical high power (an optical '1') and will allow the active layer to become unsaturated when there is a low optical power (an optical '0'). This

means that the path lengths and gain of the supermodes of the second input on the target wavelength, known as the probe signal (shown as λ_2 in figure 4.1), will change depending on the pump input. This causes the probe signal to change it's output level, thereby displaying wavelength conversion.

4.2. Wafer design

To research into a wavelength converter device, the model was used to optimise the device shown in figure 4.1. A high confinement factor in the active layer quantum wells (QWs) gives high gain and makes the device easier to saturate. It was decided a 10QW structure would give a good uniform distribution of carriers in QWs, and a reasonable confinement factor can be achieved by optimising the separate confinement heterostructure (SCH) layer. The active layer quantum wells have a confinement factor of 14.9% at transparency with a waveguide width of $4\mu m$. The width of the waveguide was chosen to be as thin as was reasonable to fabricate because the thinner the waveguide the greater the light concentration in the active region, so the amplification saturation will be greater. The limit of $4\mu m$ was chosen as totally internally reflecting (TIR) mirrors needed to be aligned with the waveguide and this width allowed the mirrors to continue to operate even with up to $0.5\mu m$ misalignment. The simulation properties used for the design stage are shown in table 4.1.

4.2.1. Optimisation process

A study of the nonlinear saturation behaviour of the AVC structure containing a 10QW active layer was carried out to optimise the structure parameters for wavelength conversion. In this process, each alteration of the AVC structure required the simulation to be run whilst sweeping the steady-state operating current density (which alters the corresponding maximum carrier concentration in the quantum wells), the device length and the pump input power. The probe output is then monitored at all of the outputs and the various transmission arrangements tested. There are four ports of the device and there are two inputs and one useful output. These could be arranged in any organisation so they must all be simulated. The optimisation target chosen was to produce the maximum extinction ratio at

Group	Property	Value	Unit
Device	Device length	Varied	μm
	N number format	"%0.2e"	string
	N Step	5×10^{16}	cm^{-3}
	N Value	3×10^{18}	cm^{-3}
	Z Step	10	μm
	Max Sweeps	100	
	Probe 0	Active	
	Probe 1	Passive	
Waveguide	Active Depth	0.075	μm
	Active X-Section	0.3	μm^2
	Current Density	4.5	$KAcm^{-2}$
	$\frac{dG}{dN}$	2.4×10^{-16}	cm^2
	Transparency (N_0)	1.5×10^{18}	cm^{-3}
	Time constant A	1×10^{8}	s^{-1}
	Time constant B	1×10^{-10}	$cm^3 s^{-1}$
	Time constant C	5×10^{-29}	$cm^6 s^{-1}$
	Band gap	1600	nm
	C_v	6.4×10^{-6}	$Hzcm^{-3}$
	n'_{sp}	0.5	
Input 0	Direction	Forward	
	Power In	0.001	mW
	Probe	Passive/Active	
	Wavelength	1550	nm
Input 1	Direction	Forward/Backward	
	Power In	Varied	mW
	Probe	Passive/Active	
	Wavelength	1550	nm
Input 2	Direction	n/a	
	Power In	n/a	mW
	Probe	none - ASE	
	Wavelength	1550	nm

Table 4.1: Design simuation settings

the probe output, for a maximum input pump extinction ratio and minimum input pump power. The maximum input extinction ratio was set to be $10dB$ as it is very unlikely for real world applications to have better extinction ratios than this. The maximum input pump power was set to be $10dBm$ as communication systems rarely use signals above this level.

For each structure the 'scanner' feature of the simulation was used to sweep the input power, device length and the current density. It was also used to switch between all the combinations of inputs and outputs as shown in table 4.2. Both inputs on the same port are avoided as this would require a coupler on the input

which would introduce more complexity into the real world system. All of the outputs are monitored in every simulation which reduces the number of simulation runs required.

Propagation direction	Pump input	Probe input
Co-propagation	Left active	Left passive
	Left passive	Left active
Counter-propagation	Left active	Right active
	Left active	Right passive
	Left passive	Right active
	Left passive	Right passive

Table 4.2: Port combinations

Operation types

Altering the gap between the waveguides and the thickness of the passive waveguide has optimised the structure of a 10 quantum well device. Figure 4.2 shows the types of operation for which the device could be optimised. Where (a) shows a single deep trough at a specific input power, which is using mainly cross phase modulation to produce the output change. (b) shows a more robust step where the trough makes the edge of the step steeper. This is using mainly cross gain modulation to produce the output change but cross phase modulation to increase the effectiveness.

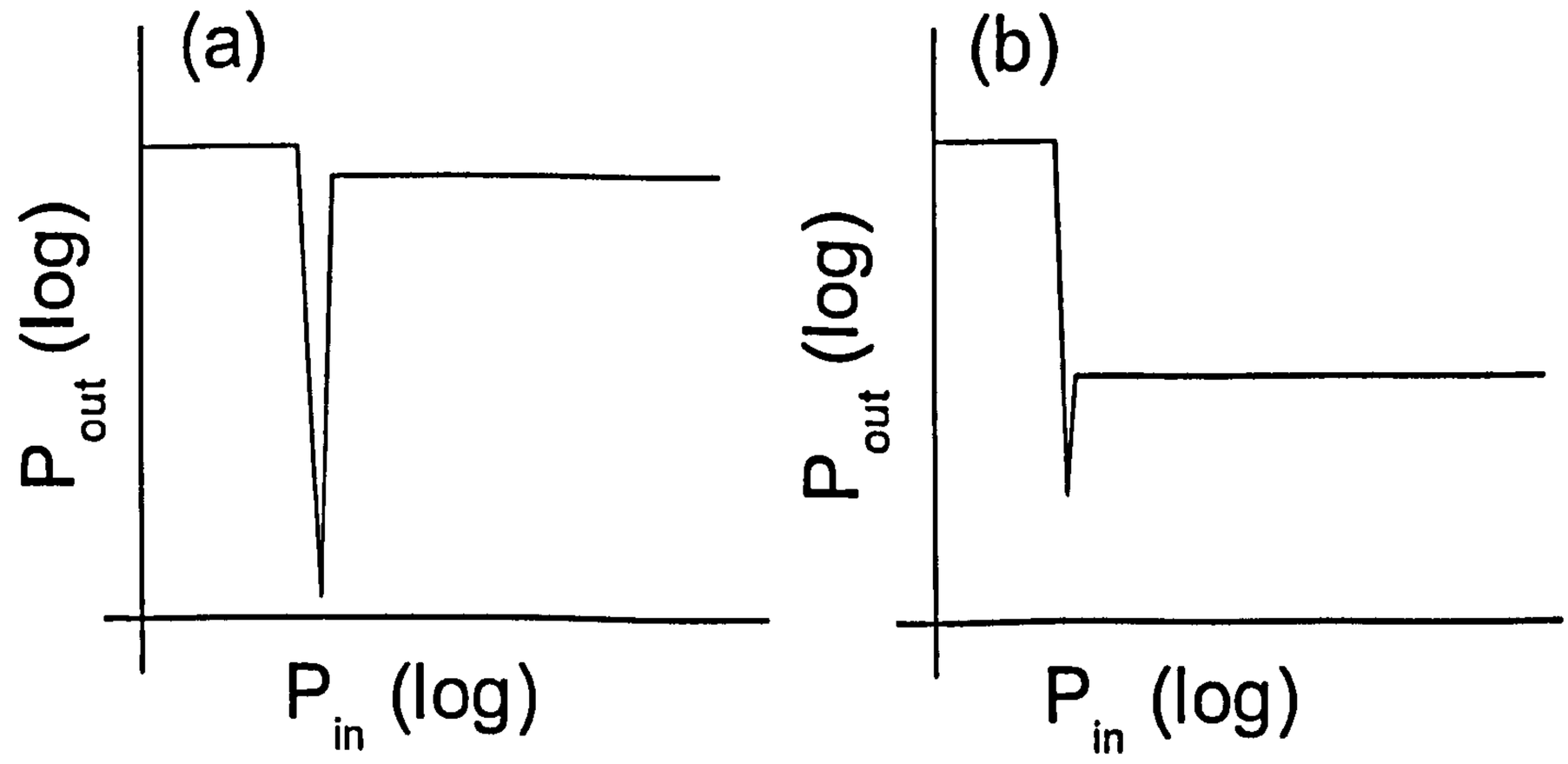

Figure 4.2: Operation Type; (a) deep trough (mainly cross-phase modulation), (b) consistent low output power (mainly cross gain modulation)

It can be seen that the device operating with mainly gain modulation is a better solution as it gives a deep trough and therefore high extinction ratios but is more robust as spikes of higher input powers would not cause as large problems.

Figure of merit

The initial design was chosen for the passive layer effective refractive index to cause strong coupling between the two waveguides so that there would be a large interaction between them. The input optical power and coupler length are scanned using the computer model to calculate the transmission under all possible transmission arrangements. These simulation results were then scanned using a Matlab script to find the best output extinction ratio for up to the maximum permitted input power of 10dBm and extinction ratio of 10dB. This best extinction ratio for each length of device is shown in figure 4.3. The maximum output extinction ratio from all of the possible lengths was used as the figure of merit for each wafer structure. The width of the passive layer was altered to change the effective refractive index of the waveguide and the gap between the two layers was altered to change the coupling ratio of the waveguides. The results of these simulations found the best combination between all of the parameters.

Waveguide gap optimisation

The figure of merit was used to iteratively improve the design of the coupler structure. Figure 4.4 shows a graph of this figure of merit depending on the gap between the two waveguides. It can be seen that there is a trend where a gap of $1.2\mu m$ gives the maximum figure of merit. It was discovered that there was a trend that showed that the larger the gap between the waveguides, the longer the device required and the lower the decision point. This is explained as a large gap reduces the coupling between the waveguides so a longer device is required for the same amount of coupling to occur. The longer the device, the more any input signal will be amplified, which means that the input signal can be smaller and still be sufficient to saturate the device. There is a limit to this trend as the longer a device the greater the ASE produced so the device will become noisy and the device becomes larger and more difficult to fabricate. Also the start of the trough becomes less steep as complete

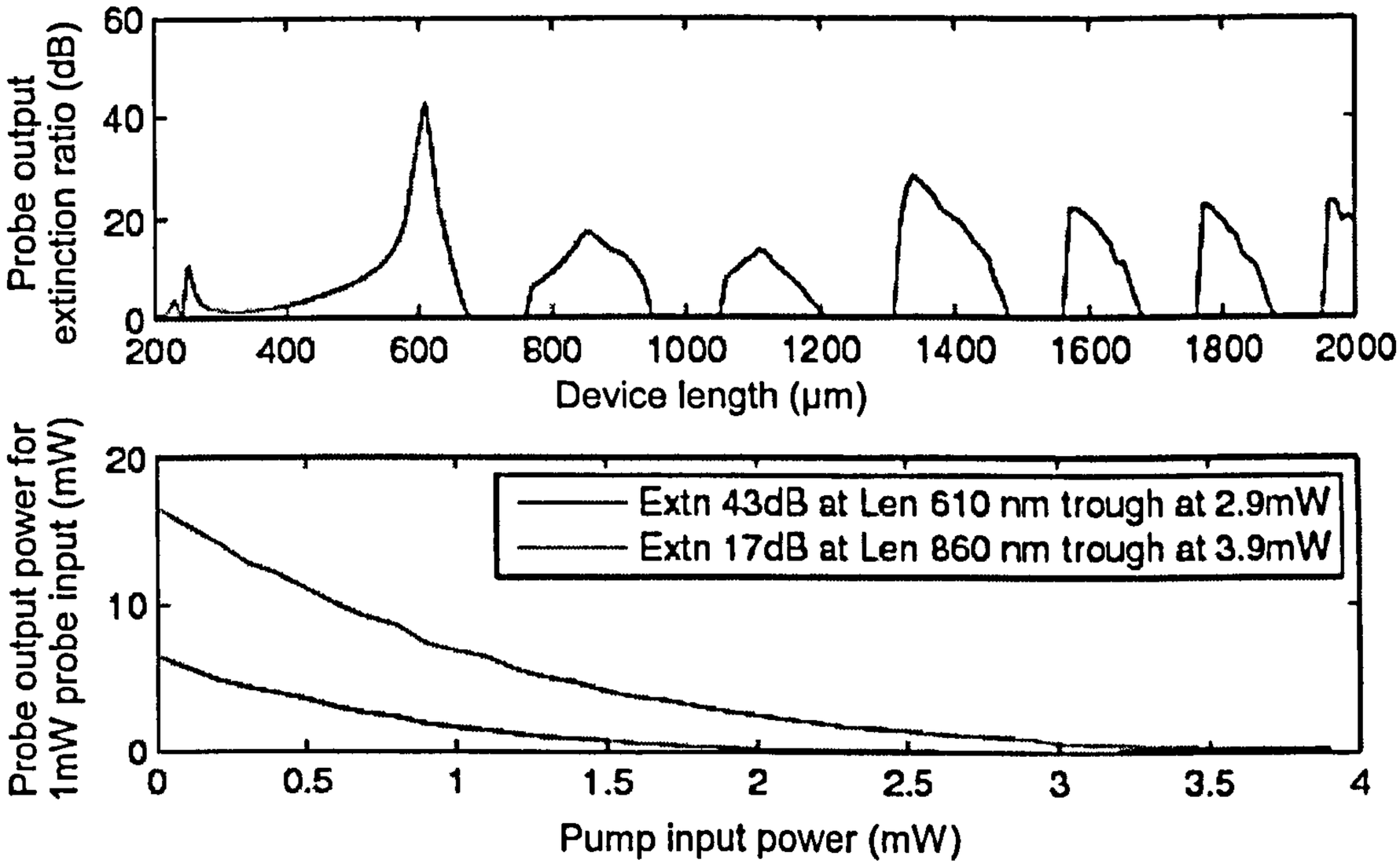

Figure 4.3: Steady-state operating points. Top: Maximum output extinction ratio for an input extinction ratio of 10dB, with maximum input power level of 10dBm. Bottom: Linear plot of input power to output power for a 1mW probe signal.

coupling does not occur.

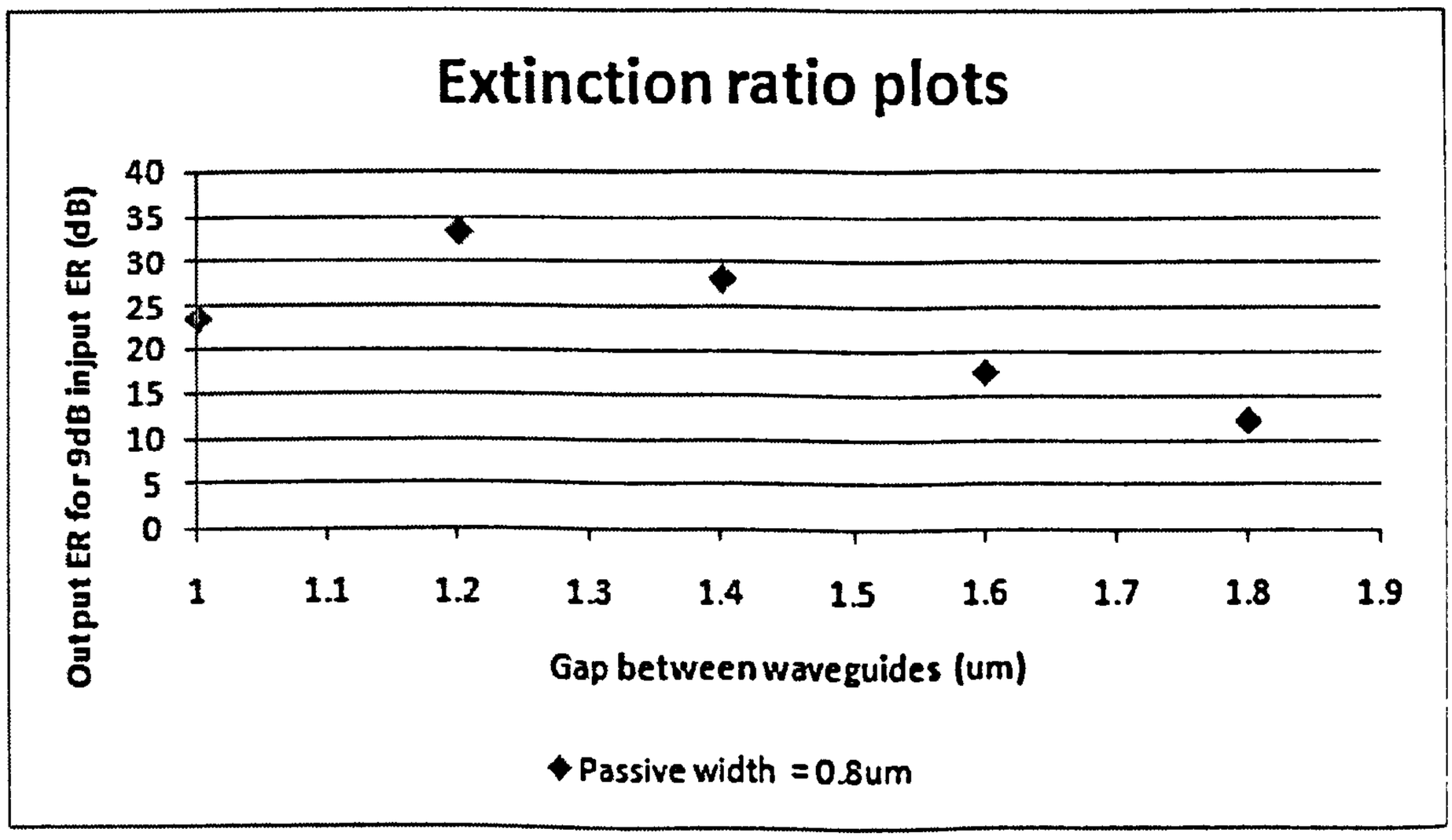

Figure 4.4: Figure of merit (output extinction ratio) when the gap between the waveguides is altered, for an input extinction ratio of 10dB

Passive waveguide width optimisation

Figure 4.5 shows the figure of merit as the passive waveguide width is altered. This plot has some spread due to the figure of merit calculation locking onto different lengths of device and different operating regimes. However, taking a trend over the maximum of these points gives a maximum figure of merit at a passive waveguide width of $0.73\mu m$. The thickness of the passive waveguide alters the symmetry of the trough, so can be used to tune the position of trough to find the minimum. The thickness of the passive waveguide alters the effective refractive index of the modes within it. This means that the passive waveguide width can be chosen to match the active waveguide's effective refractive index at a specific level of saturation. This allows the saturation that causes maximum coupling to be chosen.

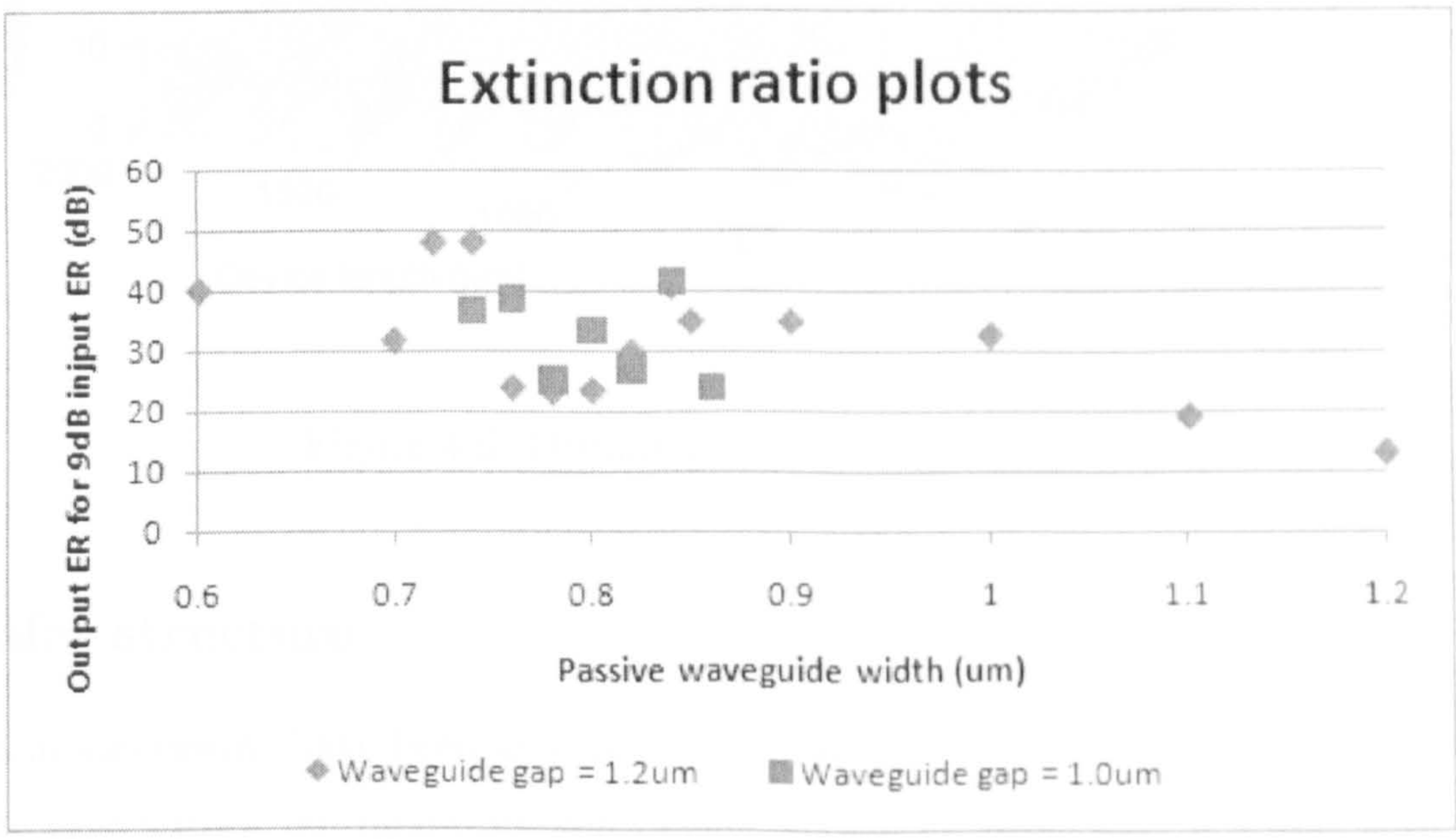

Figure 4.5: Figure of merit (output extinction ratio) when the width of the passive waveguide is altered, for an input extinction ratio of 10dB

The optimum device simulation output data is shown in figure 4.6 where the transmission of a signal wavelength within the gain bandwidth of the active layer between the two passive waveguide ports is plotted against the device length and pump power in a co-propagation mode. The wavelengths of both inputs are at the peak of the gain spectrum to speed up the simulation. As can be seen, the transmission has multiple fluctuations as the length of device is increased because of periodic coupling of light back and forth between the two waveguides. The general

increase in the transmission peak value is due to gain in the active layer. The amplitude and position of the peaks and troughs are moved by the increasing pump power.

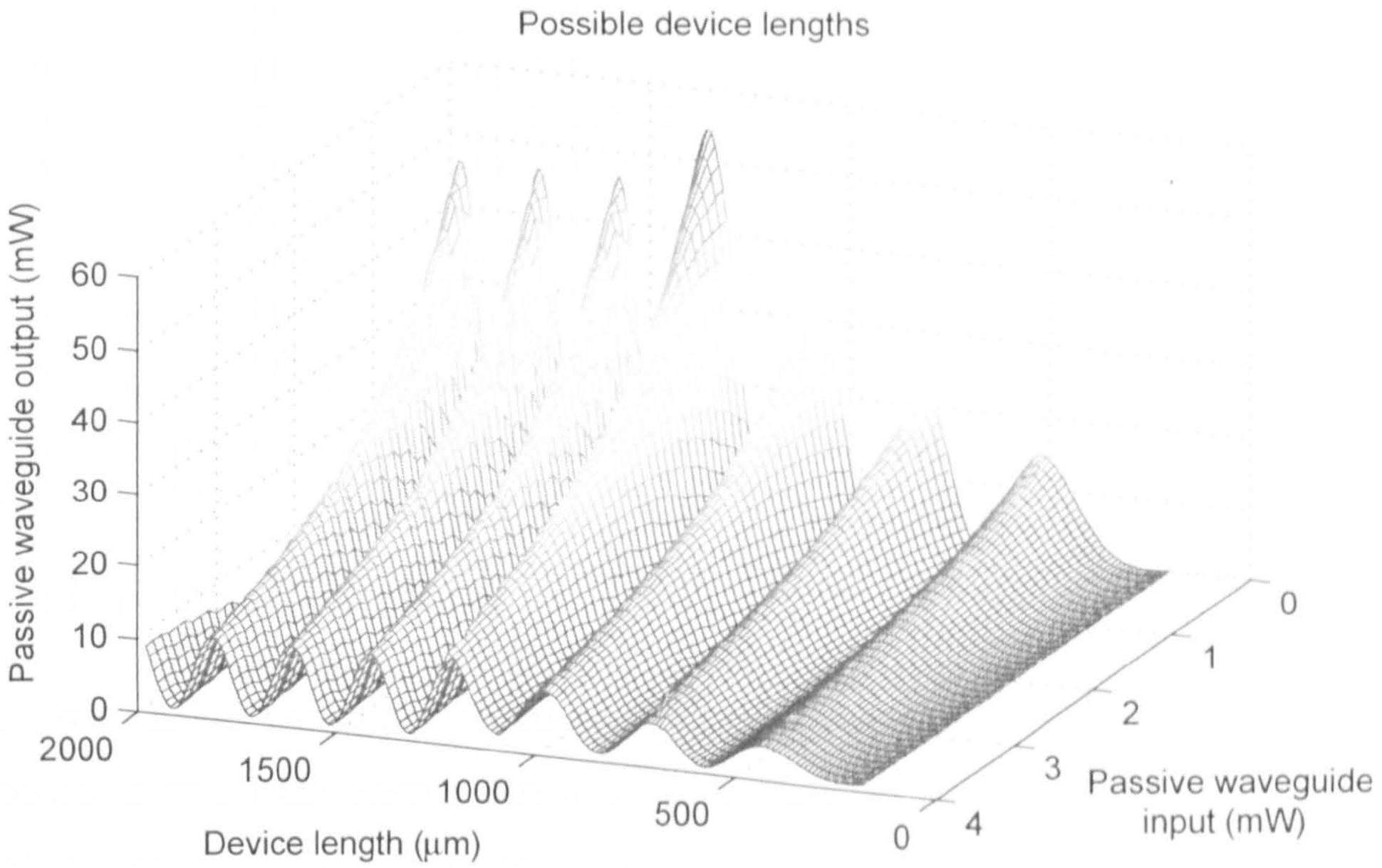

Figure 4.6: Optimum device simulation data

4.2.2. Wafer structure

The model results have been used to produce an optimised structure for the steady-state case with a ten quantum well device, shown in Table 4.3. A wafer with this structure was grown at the National Centre for III-V semiconductors in Sheffield. This structure was based upon the cross point design previously fabricated successfully at the University of Bristol [42]. The number of quantum wells has been increased to ten to increase the gain of the device so that saturation will occur more readily. The waveguide width was chosen to be $4\mu m$ as this is the smallest deep etched waveguide where mirrors can be aligned with reasonable accuracy using photo lithography.

Repeats	Thickness (A)	Material	Dopant	type	Concentration (cm-3)
1	2000	In0.53 GaAs Cap	Zn	p	1E+19
1	500	Q1.1	Zn	p	2.0E+18
1	12000	InP	Zn	p	5.0E+17
1	1162	Q1.3 Barrier	-	i	
1	75	In0.53 GaAs QW	-	i	
9	60	Q1.3 Barrier	-	i	
9	75	In0.53 GaAs QW	-	i	
1	1162	Q1.3 Barrier	-	i	
1	12000	InP	Si	n	2-4E+17
1	7300	Q1.2 passive wg	Si	n	2-4E+17
1	2000	InP cladding			2-4E+17
1	10000	InP buffer	Si	n	2E+18

Table 4.3: Optimised 10 quantum well steady-state wafer layer structure for wavelength converter

4.3. First round devices

A simple mask set was used to fabricate devices and perform simple tests and to experiment with fabrication techniques. This mask set is shown in figure 4.7 for a single length of device. The masks were made before the simulations were finished to speed up the process, so a selection of coupler lengths were chosen as 200, 400, 600 and 800µm to find the differences between them.

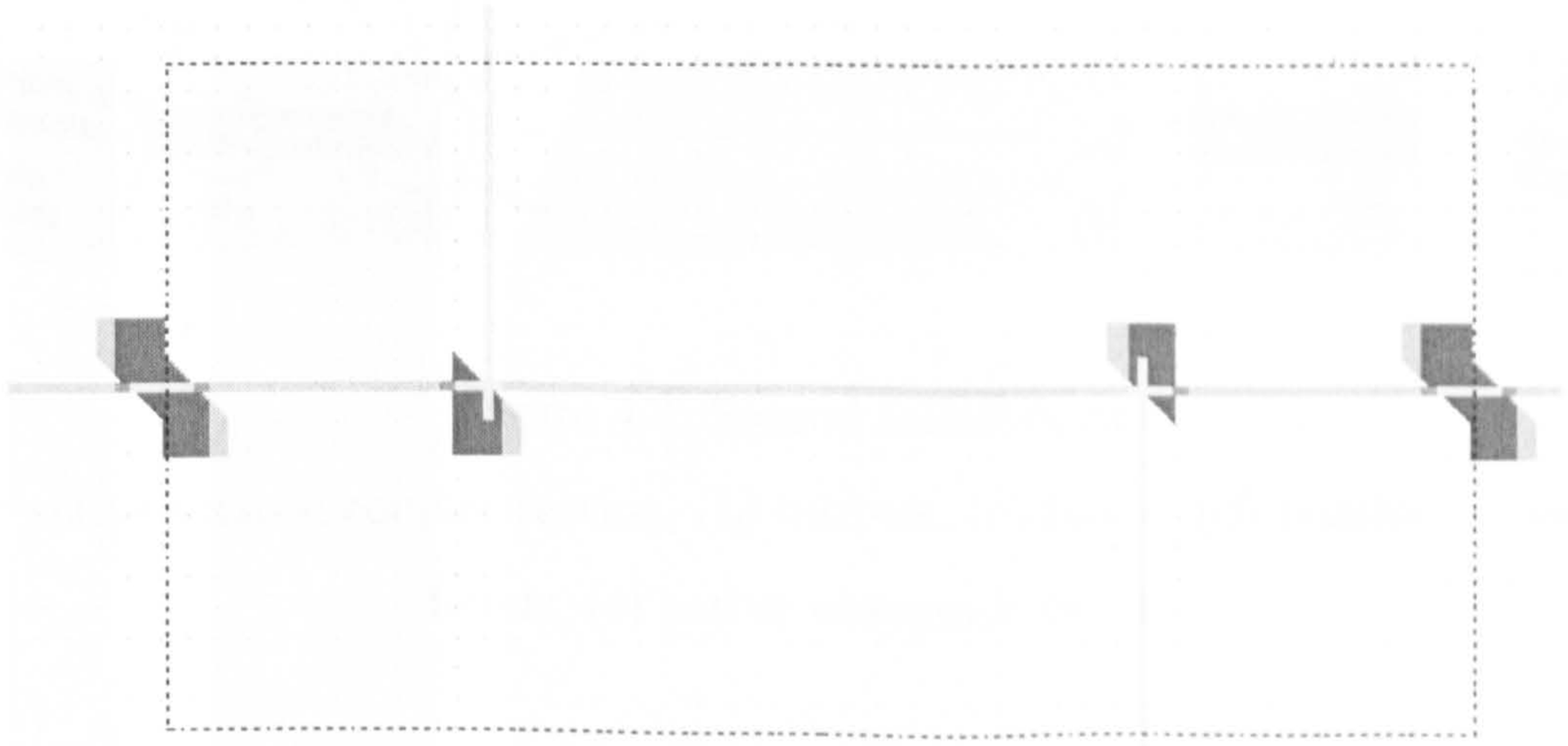

Figure 4.7: Round one device masks

4.3.1. First round problems

The first set of devices fabricated from the round one masks were found to not exhibit a diode electrical characteristic. This was discovered to be due to sidewall damage during a slow RIE etch. This was solved by developing a faster RIE etch process as explained in chapter 6. The design of the masks themselves was not good as the lengths chosen were not the most effective that the simulation predicted and the active waveguide outputs were not able to be pumped, so they caused a large attenuation.

4.4. Second round devices

The photo lithography masks were designed for devices simulated using the wafer structure shown in table 4.3.

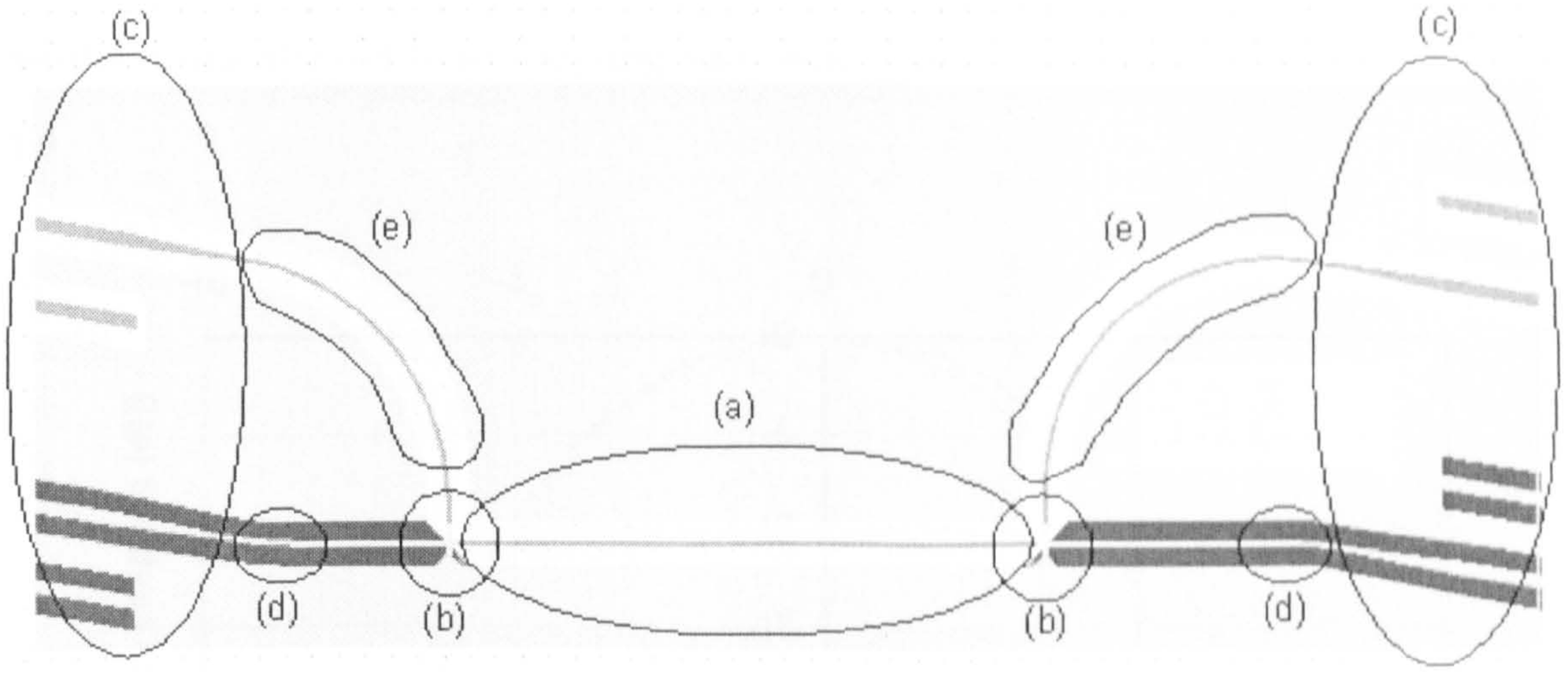

Figure 4.8: Second round device

(a) active vertical coupler section, (b) mirrors, (c) facets, (d) passive waveguide bends, (e) active waveguide bends

4.4.1. Active vertical coupler section

Six different device lengths were placed on the same set of masks to give a good selection of devices for testing. Devices were produced for the two best lengths 610 and $860 \pm 20 \mu m$ to allow for simulation and fabrication inaccuracies. The simulation results showing the best lengths are shown in figure 4.3.

4.4.2. Mirrors

The mirrors were designed to be simple 45° mirrors as they needed to be aligned to the waveguides by eye. The attenuation caused by ignoring the Goos-Hänchen shift [17] can be accepted for this first iteration of the device and the mirrors can not be fabricated to an accuracy to incorporate Goos-Hänchen shift due to the limitations in alignment accuracy of photo lithography.

4.4.3. Facets

The facets of the device were designed to be at an angle of 10° from perpendicular to the waveguide so that the reflections at the facets do not cause the device to lase. The angled facets require the fibres to be aligned at an angle of approximately 23°. To make alignment of the fibres easier, mode expanders were introduced on the horizontal plane, which allow the fibres to be butt-coupled to the device. The results of misaligned fibre coupling simulations in FimmWave are shown in Figure 4.9.

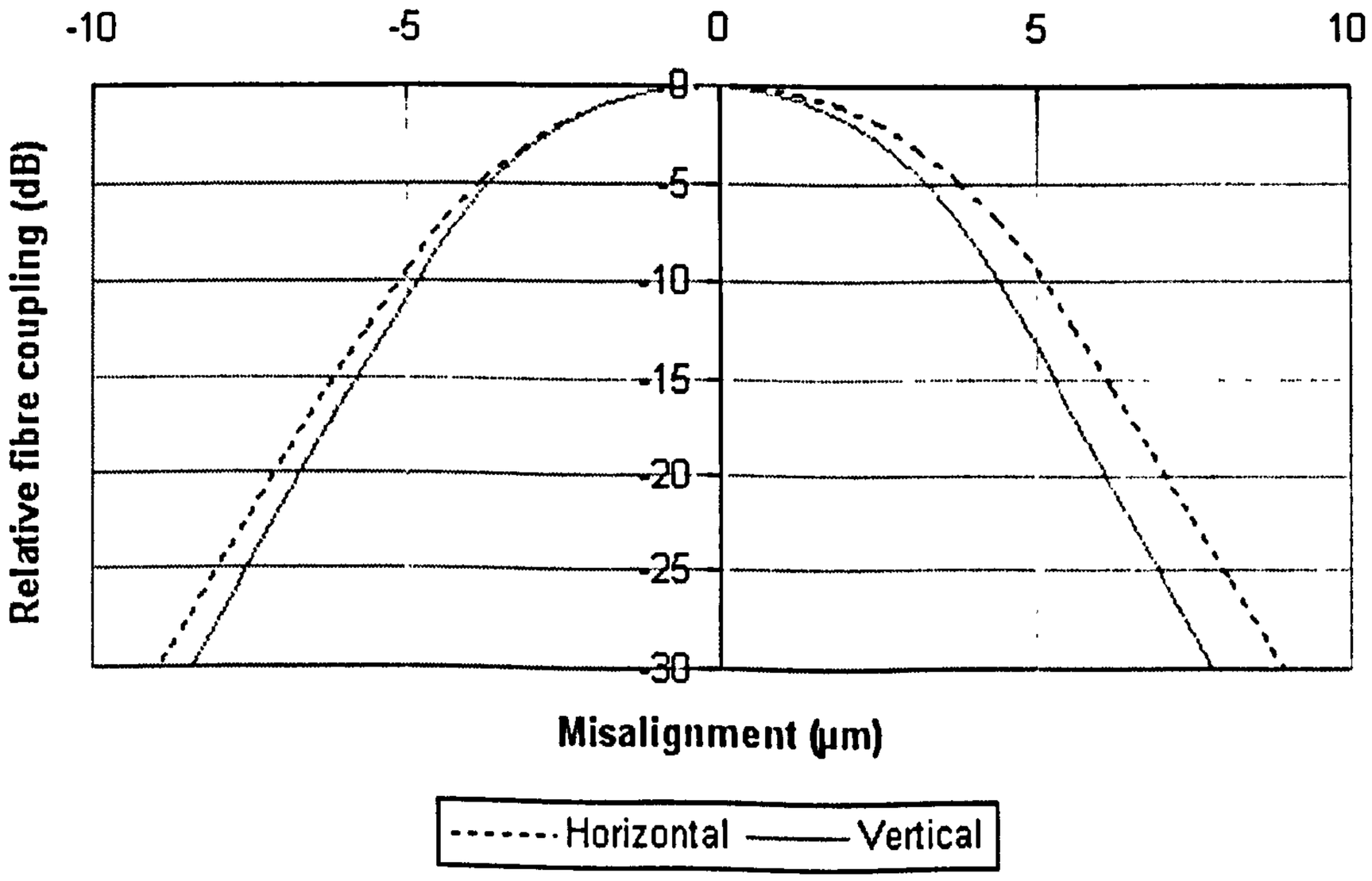

Figure 4.9: Misaligned fibre coupling simulation

The facet width of 12µm was chosen after a simulation sweep showing coupling losses was reviewed as shown in figure 4.10.

4.4.4. Passive waveguide bends

Due to the 10° angled facets, either the whole device needed to be at 10° to the crystal plane of the substrate or there needed to be two 10° bends at each end of the device. As the longer devices are a minimum of $1mm$ long rotating the whole device would require that each die would have to be a minimum of $1mm \times sin(10°) = 174\mu m$ wider. Also rotating the whole device off the crystal plane would mean that the device could not be cleaved shorter to test sections of the device separately. Due to these reasons the passive waveguides have 10° bends before the facets. The results of a Fimmwave simulation varying the radius of a circular bend are shown in figure 4.12 from where a bend radius of $470\mu m$ was chosen. This corresponds to the centre line of the waveguide having a height of $470(1 - cos(10°)) = 7.14\mu m$ and a length of $470sin(10°) = 81.615\mu m$.

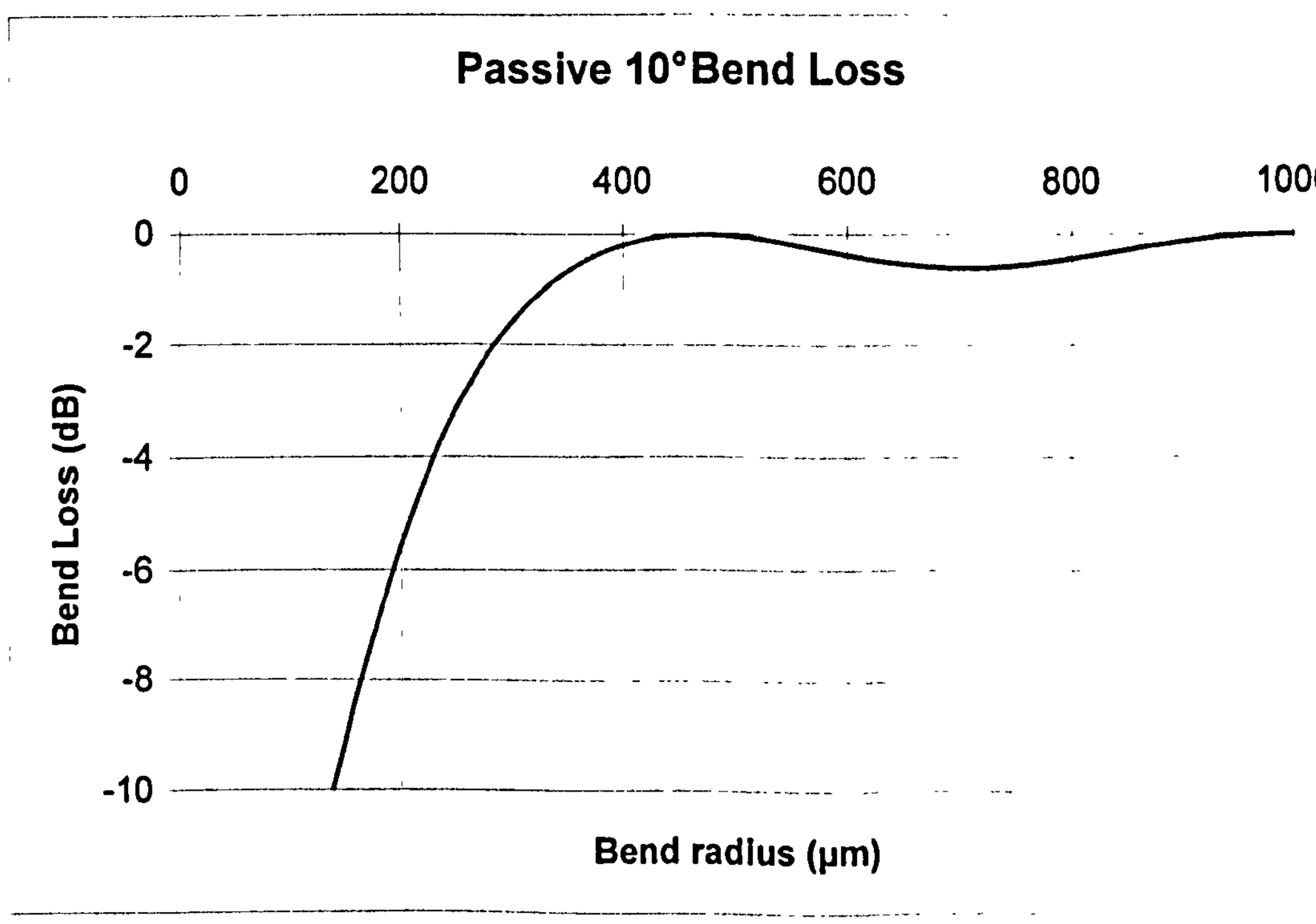

Figure 4.12: Bend loss in the 10° passive waveguide bend

4.4.5. Active waveguide bends

There must be an 80° bend after the TIR mirror on one end of the device and a 100° bend on the other end. This should mean that there will be less loss than doing a 90° bend then 10° either way and only increases complexity slightly at the design stage.

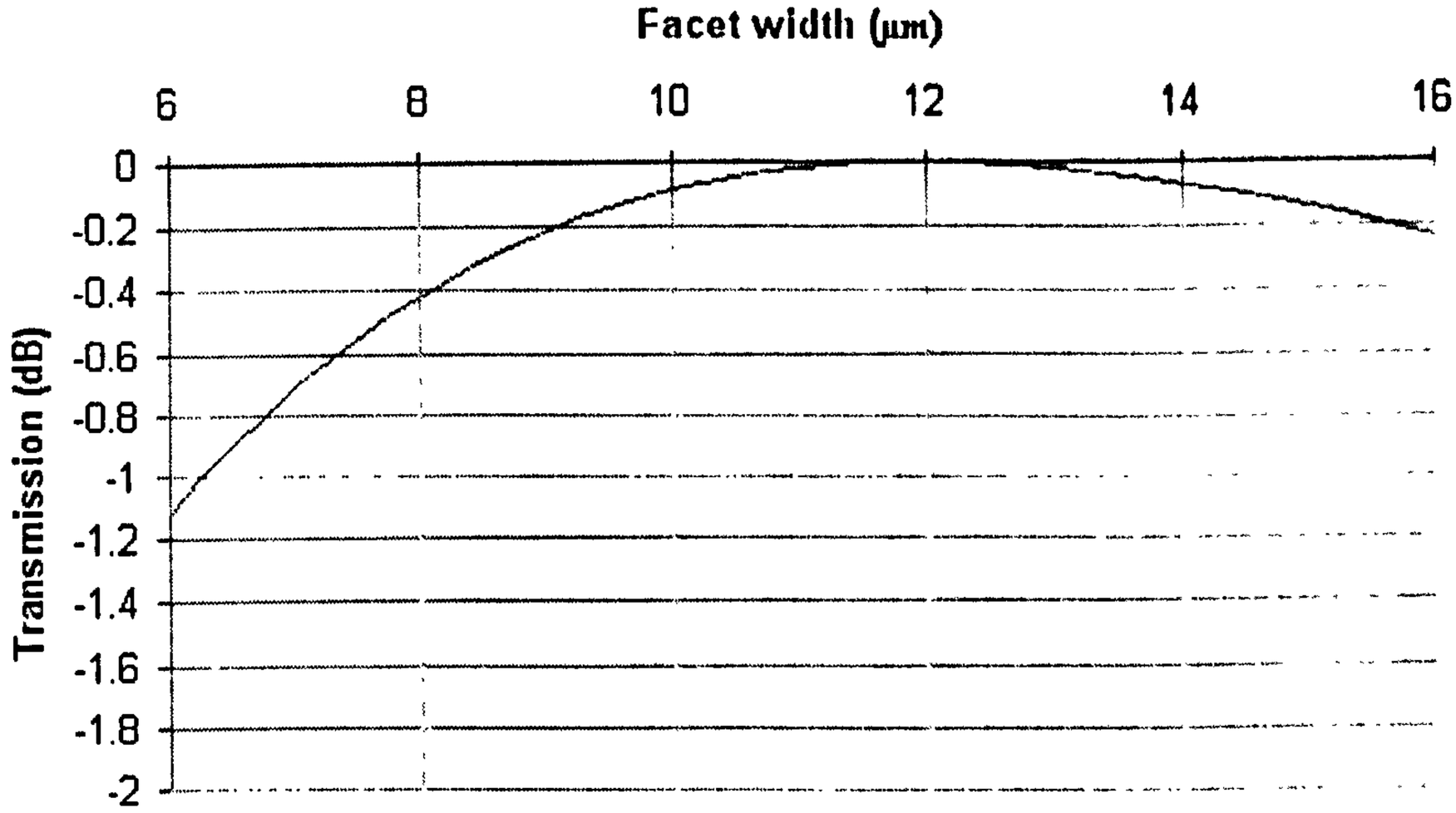

Figure 4.10: Facet width simulation

The taper length of $110\mu m$ was chosen after the simulation results shown in figure 4.11 were reviewed.

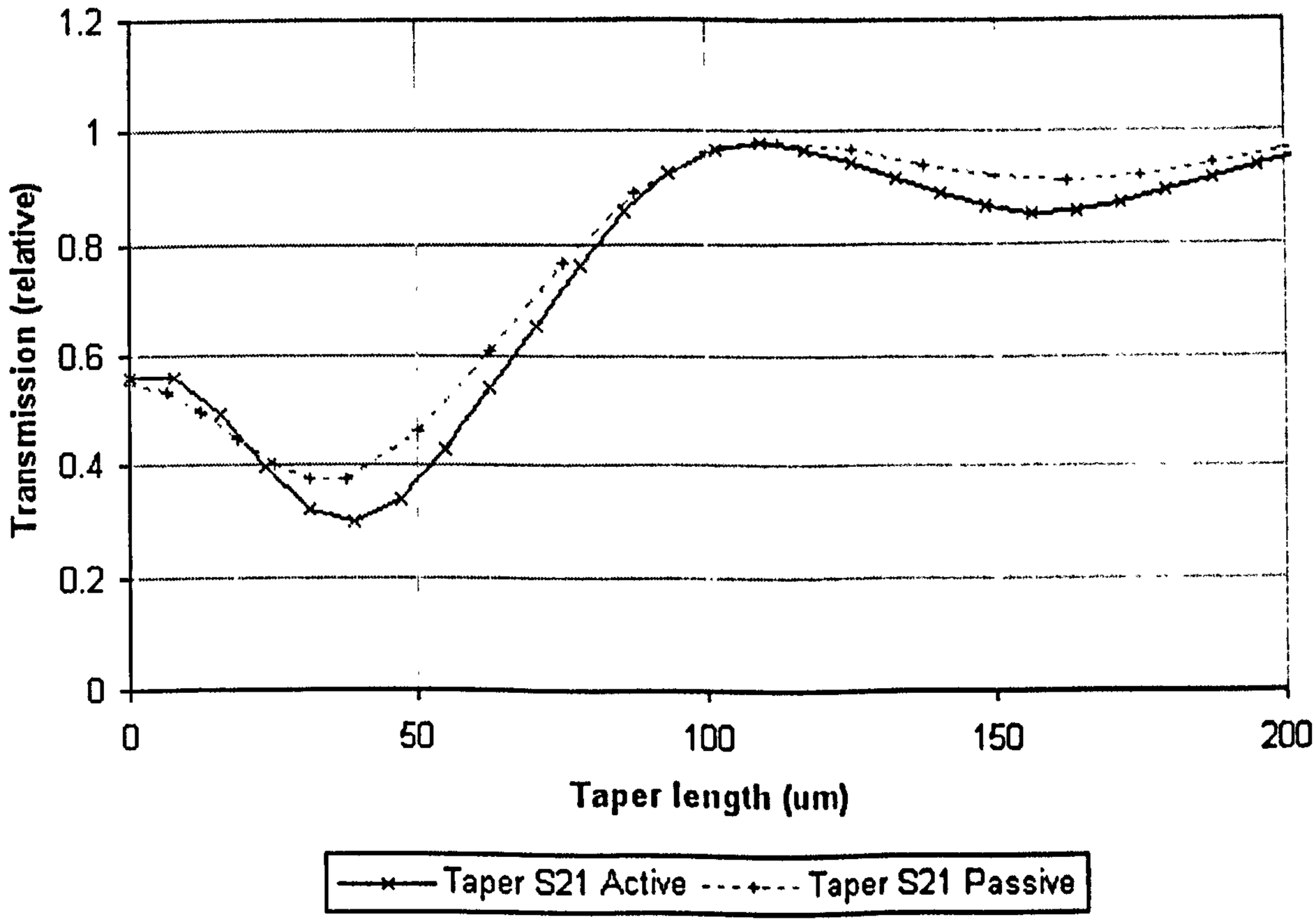

Figure 4.11: Taper length simulation

The Fimmwave simulation results for the 80° bend are shown in figure 4.13 where it can be seen that a radius of $241\mu m$ is a good compromise between size of the structure and stability due to manufacturing tolerances. This radius corresponds to the centre line of the waveguide having a height of $241sin(80^o) = 237.34\mu m$ and a length of $241(1 - cos(80^o)) = 199.15\mu m$.

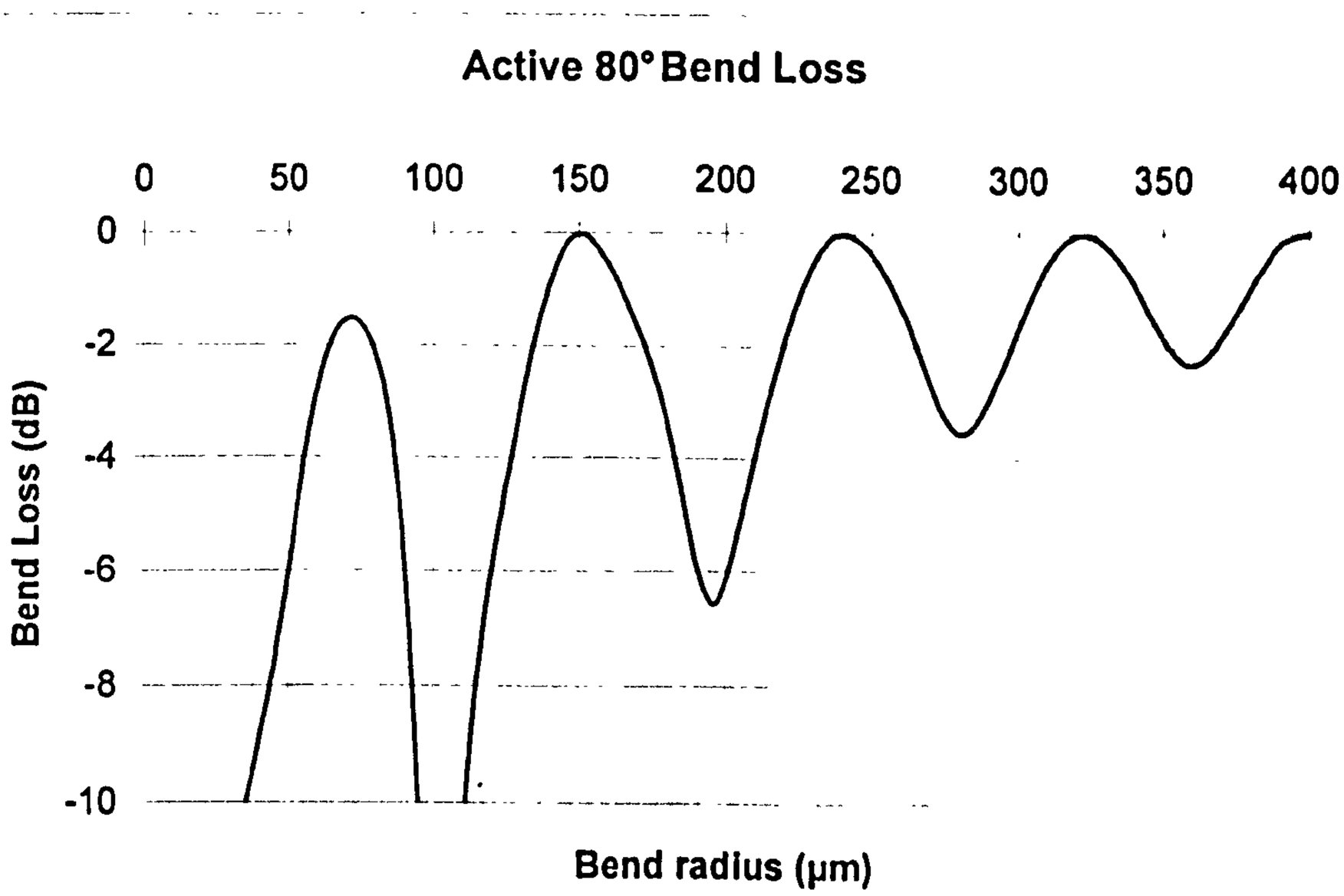

Figure 4.13: Bend loss in the 80° active waveguide bend

The Fimmwave simulation results for the 100° bend are shown in figure 4.14. The dotted lines are the results for the same structure with the waveguide width adjusted by $\pm 0.25\mu m$. A radius of $224\mu m$ was chosen as a good compromise between minimum loss with exact fabrication, no more than 2dB loss with fabrication error less than $\pm 0.25\mu m$ and size of the feature. This radius corresponds to the centre line of the feature having max height of the full radius ($224\mu m$), final height of $224sin(100^o) = 220.60\mu m$ and a width of $224(1 - cos(100^o)) = 262.90\mu m$.

In all of these bend simulations it can be seen that the bend loss seems to be oscillating with bend radius, which would not be true for a single mode waveguide. The reason for the oscillations is that within the bend light is transferred into higher order modes. The majority of this light will be coupled back into the output waveguide, however there will still be a proportion in higher order modes. The model for these simulations placed an output waveguide after the bend that cut off either the

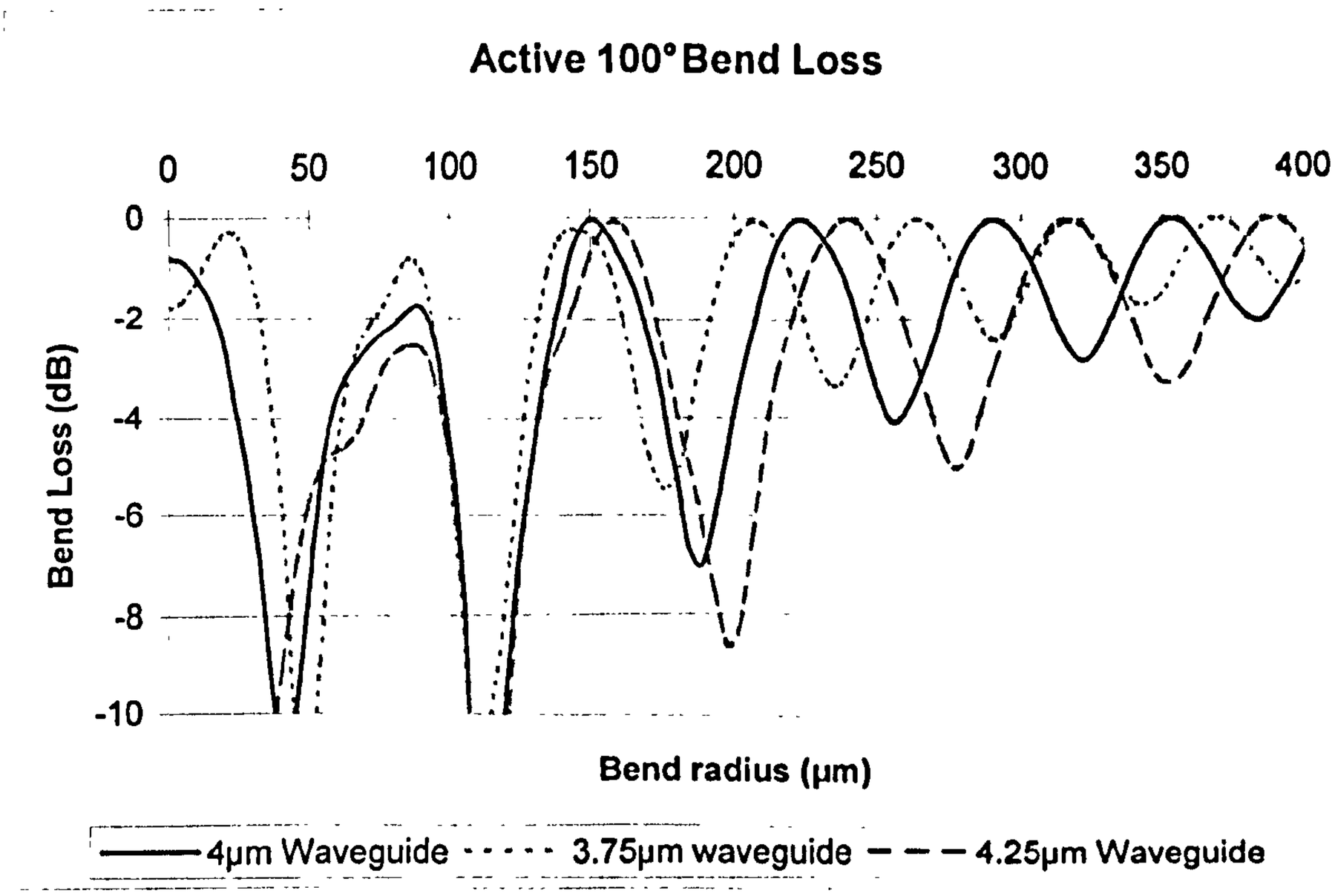

Figure 4.14: Bend loss in the 100° active waveguide bend including fabrication tolerances

active or the passive waveguide. Therefore any light still in the high order modes will cause oscillations in the output depending on the length of the waveguides.

Chapter 5

Fabrication Processes

This chapter will describe the fabrication processes that were used and developed in the course of this PhD project.

5.1. Passivation layer deposition

Thin films of silicon oxide (SiO_2) and silicon nitride (Si_3N_4) are required for etch masks, device passivisation and carrier wafer protection. A plasma enhanced chemical vapour deposition (PECVD) machine was available at the University of Bristol to produce these films. The PECVD process works by injecting gasses into a process chamber which is kept at a constant low pressure using an automatic pressure controller (APC). The chamber is heated to a given temperature and a radio frequency (RF) plasma is started. In the SiO_2 process, the active gases are a silane (SiH_4) /nitrogen (N_2) 95%/5% mix and nitrous oxide (N_2O) and in the Si_3N_4 process they are the silane/nitrogen (SiH_4/N_2) mix and ammonia (NH_3). Once the auto-matching unit was repaired these process could be run in a more automated manner and more importantly it enables pulsed high/low frequency RF to be used for the nitride deposition process. The process settings are shown in tables 5.1 and 5.2 for silicon oxide and silicon nitride respectively.

SiH_4/N_2 95%/5% flow rate	$240cm^3s^{-1}$
N_2O flow rate	$825cm^3s^{-1}$
Pressure	$800mT$
High frequency power	$55W$
Temperature	350^oC
Deposition rate	$75nm/min$

Table 5.1: Silicon oxide PECVD process

SiH_4/N_2 95%/5% flow rate	$500cm^3s^{-1}$
NH_3 flow rate	$27.9cm^3s^{-1}$
Pressure	$920mT$
High frequency power	$35W$
High frequency pulse time	$11s$
Low frequency power	$35W$
Low frequency pulse time	$9s$
Temperature	350^oC
Deposition rate	$30nm/min$

Table 5.2: Silicon nitride PECVD process

5.2. Photo Lithography

Photo lithography is the process that transfers the pattern from a mask onto the wafer. The normal method is to use positive photo resist where after development there is resist where the mask is dark and no resist where the mask is transparent.

5.2.1. Positive photo resist

The standard photoresists that are used are S1805 ($0.5\mu m$ thick) and S1813 ($1.3\mu m$ thick). The process for their use is shown below.

1. Wash samples
2. Drying oven bake for 10 mins at 90°C
3. Spin microposit primer, drip on, 10s still, 10s at 4000 RPM
4. Spin S1805 or S1813 photo resist, drip on, 10s still, 30s at 4000 RPM
5. Pre-bake in oven for 10 mins at 90°C
6. Align mask to the sample
7. Expose to ultra violet light for 30s with S1805, 60s with S1813.
8. Develop using MF319 developer for approx 1min until exposed areas are clear

SPR220 is a $4\mu m$ thick resist that is very good for liftoff processes but can not be used on very small features. The process for using SPR220 is shown below.

1. Wash samples
2. Drying oven bake for 10 mins at 90°C
3. Spin microposit primer, drip on, 10s still, 10s at 4000 RPM
4. Spin SPR220 photo resist, drip on, 10s still, 30s at 3000 RPM, 3s at 6000RPM

5. Pre-bake on hotplate for 90s at 120°C
6. Align mask to the sample
7. Expose to ultra violet light for of a minimum of 120s (varies on the depth of trenches that need developing).
8. Development using MF319 developer for approx 1min until exposed areas are clear

5.2.2. Negative photo resist

In the process of fabrication, some of the round one masks were the inverse of what was required. Therefore a process of producing negative images from photo resist was fine-tuned using photo resist that can be cross-linked to produce areas of photo resist that are resistant to developer. The process is shown below.

1. Wash samples
2. Drying oven bake for 10 mins at 90°C
3. Spin microposit primer, drip on, 10s still, 10s at 4000 RPM
4. Spin AZ1514 photo resist, drip on, 10s still, 30s at 4000 RPM
5. Pre-bake on hotplate at 110°C for 1min
6. Align mask to the sample
7. Expose to ultra violet light for 20s
8. Reverse bake on hotplate at 85°C for 2mins, which cross-links the exposed areas making them resistant to developer even after more exposure.
9. Flood exposure for 130s
10. Development using MF326 developer for approx 1min until non-exposed areas are clear

5.2.3. Liftoff resists

For liftoff processes, where a thin metal film is evaporated or sputtered onto the patterned resist, it is often useful to use liftoff resists. These are thin layers of polymer resist placed underneath the normal resist, which is not photosensitive and develops faster than the standard photo resist. The result of this is that after development there is an undercut in the resist which means that the metal layer

deposited on top is completely broken along the edge of the resist so that the metal on the surface of the resist is easily removed when the resist is removed. This can be seen in figure 5.1. The process for spinning liftoff resists is show below.

1. Wash samples
2. Drying oven bake for 10 mins at 90°C
3. Spin LOR3B photo resist (300nm thickness), drip on, 10s still, 30s at 4000 RPM
4. Pre-bake on hotplate for 10 min at 210°C
5. Leave for 5 mins too cool
6. Continue with the normal photo resist process without the primer step (Continue from item 4 in section 5.2.1)

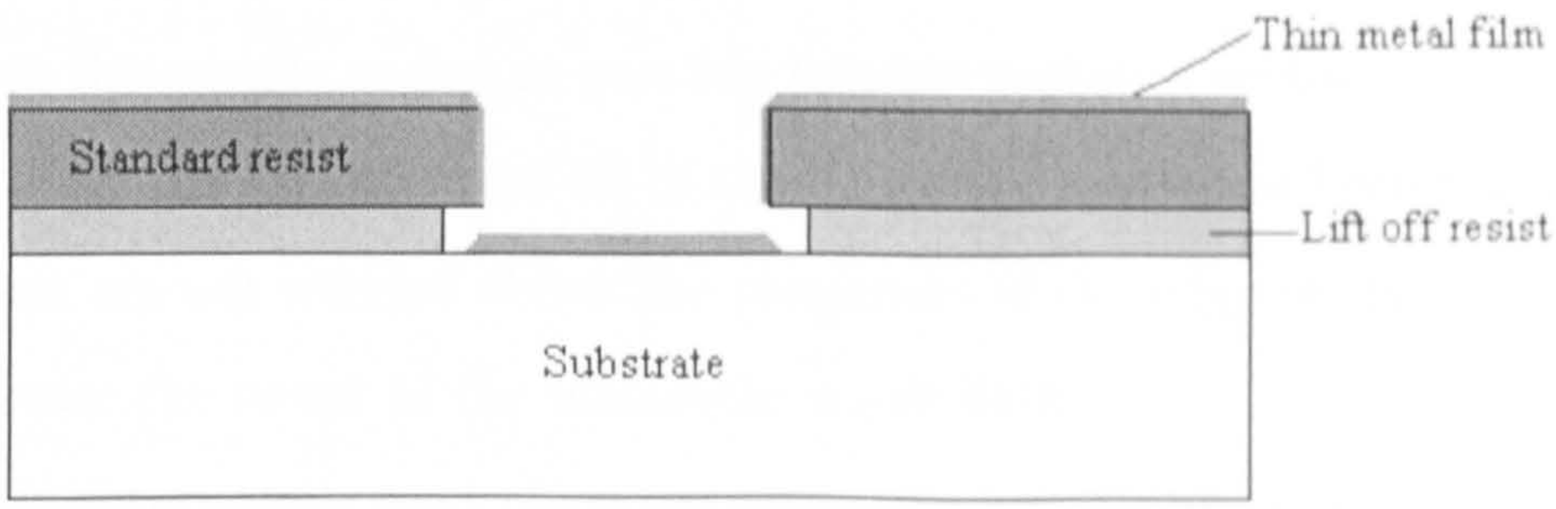

Figure 5.1: Lift-off resist profile

5.3. Metal Evaporation

Thin layers of metal are deposited onto the surface of a wafer sample using an evaporator. This process is normally used for evaporating a 50nm layer of nickel to be used as a mask for dry etching silicon oxide and nitride.

1. Use section of adhesive pad to mount sample to a glass slide and place in chamber
2. Place coiled nickel wire in boat and close shutter
3. Pump the chamber down to approximately $10^{-6} Torr$
4. Slowly increase the power supply voltage to the boat until the current is approximately $8A$

5. Open shutter and adjust voltage slowly until deposition rate is approximately 1.2Å/s
6. Wait until about 20Åless than the thickness required then close the shutter
7. Reduce the supply current slowly, then switch off supply
8. Allow chamber to cool, then vent and retrieve samples

5.4. Liftoff Process

To begin the liftoff there must be a pattern of photoresist underneath a thin metal film (normally nickel or the p contact). The use of a liftoff resist under a normal resist will make this process better.

1. Place a beaker of acetone in the ultrasonic water bath with the power set to 20
2. Drop the sample as flat as possible into the agitated acetone.
3. Leave in the acetone until all of the unwanted metal has been removed.
4. If you are not worried about the roughness of the edge of the metal, you can increase the power of the ultrasonic water bath.
5. If liftoff resist was used place the sample in microposit remover in a hot water bath set to 60°C for 10 min.

5.5. Silicon oxide and nitride etching

Silicon oxide and nitride are etched in a reactive ion etching (RIE) machine. This is a dry etching process where the active gas is CHF_3. The Florine ions react with the silicon in a plasma environment producing good vertical side walls. The settings used are as shown in table 5.3.

$O_2 \Delta P$	$1mT$
$CHF_3 \Delta P$	$2mT$
$Ar \Delta P$	$10mT$
RF Power	$270W$
SiO_2 Etch Rate	$20nm/min$
Si_3N_4 Etch Rate	$18nm/min$

Table 5.3: Silicon oxide and nitride process settings

5.6. ICP/RIE dry etching

The wafer has an indium phosphide (InP) substrate with a pattern of InP and indium gallium arsenide phosphide (InGaAsP) quaternary layers grown on the surface as shown in table 4.3. The etch processes are implemented in an inductively coupled plasma/reactive ion etching (ICP/RIE) machine. A plasma of the injected gasses generated by a RF field is enhanced and concentrated on the sample by a magnetic field. As electrons are more mobile than the holes in the plasma, the sample is bombarded by a greater proportion of electrons. This means that a negative electrical field builds up on the sample repelling more electrons and attracting positive ions in the plasma. It is this field that causes anisotropic etching due to reactive ions reacting with the surface of the semiconductor. There is also some mechanical etching as high energy particles collide with the sample and there is some more chemical etching due to the free radicals in the plasma, which are not affected by the electric field.

Two different processes were required for dry etching the semiconductor; one for use with a nickel mask and one for use with a silicon oxide or nitride mask.

The process using high inductively coupled plasma (ICP) power with high RIE power has a high etch rate but it would sputter a nickel mask over the rest of the sample, causing damage to the devices. Therefore this process was used for etching deep trenches where there was an oxide or nitride mask. The RIE only process is relatively slow, so it has been sped up by including a low ICP power that is small enough so that it does not damage the nickel mask.

5.6.1. Fast ICP etching

The optimised settings for this fast etch process are shown in table 5.4. This process is sensitive to the processes that have been run in the chamber previously, so this process was run for five minutes with an empty chamber before the samples were etched. Tested on pure InP the etch rate is $1.4\mu m/min$ and using the wafer shown in table 4.3 the average etch rate of the quaternary layers is $800nm/min$. This etch process had the most variable etch rate varying from 1 to $1.4\mu m/min$ this is thought to be because the RIE/ICP machine does not have the helium thermal

some changes in the process without significantly affecting the semiconductor etch.

CH_4 flow rate	$8cm^3s^{-1}$
H_2 flow rate	$24cm^3s^{-1}$
Chamber pressure	$7mT$
RF Power	$250W$
ICP Power	$100W$
Table temperature	$100°C$
Strike pressure	$15mT$
Strike ramp	5mT/s
Etch rate	$50nm/min$

Table 5.5: Fast RIE process for etching InP

5.6.3. Gentle ash clean

The gentle ash clean process is used for cleaning polymers from the surface of samples. The process details are shown in table 5.6.

O_2 flow rate	$50cm^3s^{-1}$
Chamber pressure	$20mT$
RF Power	$100W$
ICP Power	$0W$
Table temperature	Insensitive
Strike pressure	n/a
Strike ramp	n/a

Table 5.6: Gentle ash clean

5.7. Profiler

To use the Talysurf Form Plus to produce a profile of a sample, the profile length must be selected and the gauge range set to 0.1mm. The dump settings must be set to profile only and setting data dump to auto is the easiest method to read the data. A program was written in Visual C++ v6.0 to receive the data dump from the profiler over the serial port and display the data as a graph. The program could be used to correct for a fixed angle in the reading and to measure the vertical distances between cursors.

contact enabled and this is the process that generates the most heat. The etch rate will vary with sample temperature as the higher the temperature the greater the volatility of the surface material, which means the etch rate will increase. Without the helium the repeatability of the thermal contact between the carrier wafer and the table is bad so this is likely to be the problem. However, the verticallity of the etch does not suffer significantly and as long as the device is not over etched there is not an overall problem.

Cl_2 flow rate	$11cm^3s^{-1}$
CH_4 flow rate	$10cm^3s^{-1}$
H_2 flow rate	$12cm^3s^{-1}$
Chamber pressure	$4mT$
RF Power	$160W$
ICP Power	$1000W$
Table temperature	$60°C$
Strike pressure	$20mT$
Strike ramp	6mT/s
Max etch rate	$1400nm/min$

Table 5.4: Fast ICP process for etching InP

5.6.2. Fast RIE etching

This process was optimised in the same manner as in section 5.6.1 using pure InP samples to improve the verticality and the etch rate. However, this process was required to be used with a nickel mask. It was found that ICP powers in the order of 150W and above caused the nickel mask to be sputtered over the rest of the sample. Therefore a maximum limit of 100W ICP was imposed. The process uses methane (CH_4) and hydrogen(H_2) as the etch gasses so that the verticality of the sidewalls can be adjusted by altering the growth rate of the polymer that is formed on the surface of the sample. The greater the proportion of methane in the chamber the faster the production of polymer. The ideal state is where the polymer production on the sidewalls is exactly counteracted by the etch rate of the process so that there is no build up. However, this state would be impossible to achieve exactly so the process was optimised so that there would be a thin layer of polymer on the surface of the mask after 20 minutes of etching. The thickness of polymer was chosen so that it could be removed by 30 seconds of gentle oxygen ash cleaning to allow for

5.8. Thin Metal Film Deposition

To deposit the contact layers on the device a Laybold L560 device was used. It can sputter gold, palladium, titanium and nichrome. It also has an e-beam evaporator for germanium.

Table 5.7 shows the layers and settings used to create the p contact which is on the top, patterned side of these devices.

Material	Power (W)	rate (Å/s)	Pot Setting	Time(s)	Total thickness (nm)
Ti	493	10	2.34	50	50
Pd	172	11	0.81	45	50
Au	149	9	0.7	167	150

Table 5.7: P contact layers

Table 5.8 shows the layers and settings for the n contact which is on the underside of these devices. After annealing, an extra layer of $100nm$ of gold is deposited to improve the wire bonds required later.

Material	Power (W)	rate (Å/s)	Pot Setting	Time(s)	Total thickness (nm)
Au	149	9	0.7	15	15
Ge	Evaporation	≈ 2			35
Au	149	9	0.7	15	15
Ni	150	4	0.81	27	11
Au	149	9	0.7	167	150

Table 5.8: N contact layers

5.9. Wafer Thinning

The substrate of the wafer is supplied with a thickness of 500µm. This needs to be reduced to decrease the substrate resistance and to make the wafer easier to cleave. The instructions for thinning down using a hand jig is described here.

1. The jig mount is placed on the sprung loaded vice on a hotplate set to approximately 200°C.
2. When the mount reaches temperature, a small amount of wax can be dotted on the surface where the sample(s) will be placed as symmetric around the centre as possible.
3. The samples are dropped gently onto the molten wax.

7. 30 sec heating up to 400°C.
8. 1 min stabilisation at 400°C.
9. Cool down to room temp.
10. Vent the chamber and extract the samples

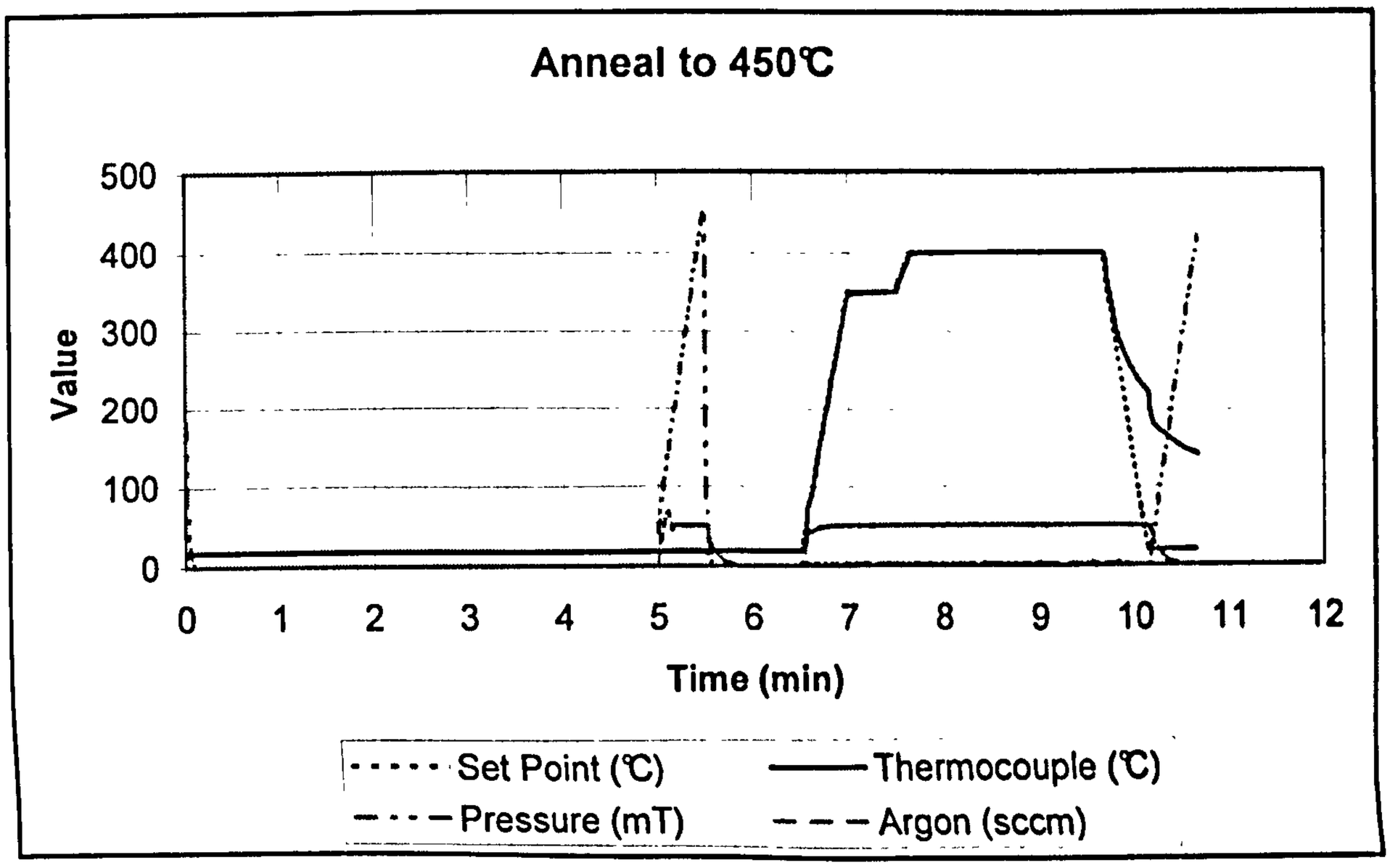

Figure 5.2: Annealing data at 400°C

5.11. Cleaving

The cleaving method found to work well with small samples is described below.

1. Place sample on the scriber plate and align a crystal edge with the cross-hairs on the microscope eyepiece.
2. Align the horizontal position of the plate so that the vertical cross-hair is where you wish the sample to be cleaved.
3. Move the plate backwards so that the sample is underneath the diamond scribe tip at the start of the short mark that will be made. Ensure that it is not close to any waveguides as they will be broken by the tip.
4. Lower the diamond scribe tip gently until it is pressing firmly on the sample.
5. Pull the plate forwards gently until a small movement has been seen.
6. Lift the scribe tip and view the mark under the microscope.

4. A flat plate covered in a thin layer of paper (A Post-It note is useful for this) is placed on top of the samples.
5. The sprung loaded vice is tightened to apply pressure to the samples to ensure that they are flat.
6. The whole vice is removed from the hotplate and left to cool.
7. The sprung loaded vice is released and the samples attached to the jig mount is removed.
8. The thickness of the sample on the mount is measured using the Talysurf profiler as there will be some unknown thickness of wax under the sample.
9. the jig mount is attached to the polishing jig and the zero level found by adding shims until the jig does not wobble on a flat surface when the bolts are tight.
10. Shims that sum to 50µm less than required thickness to be thinned are removed from the jig.
11. 5µm alumina polishing powder is mixed with water on a glass polishing plate and the samples are thinned down to the shim setting.
12. The last 50µm of shims are removed and the final polishing is completed with 0.5µm alumina powder.
13. The jig mount is heated on a hotplate and the sample carefully scraped onto a watch glass.
14. The sample is left in a beaker of acetone overnight to remove the wax.

5.10. Annealing

Devices require annealing to diffuse the contact metal into the semiconductor making an ohmic contact instead of a Schottky diode. The data captured during an annealing process is shown in figure 5.2 where the sequence of events is as follows.

1. Load samples into the chamber.
2. 5 min of pumping down the chamber.
3. 30 sec of purging the chamber in argon.
4. 1 min pumping down again.
5. 30 sec heating from room temp to 350°C.
6. 30 sec plateau at 350°C.

Chapter 6

Device Fabrication

The model was used to design and fabricate a wavelength converter device. This device was designed to use both cross phase and cross gain modulation in an active vertical coupler structure.

6.1. Fabrication steps

The steps that were used to fabricate the round two devices from an 8×8mm sample of the basic planar wafer are described in this section.

6.1.1. Mask deposition

Deposit silicon oxide or nitride to act as the main etch mask. The silicon oxide process was more stable at this time so that material was used. Some of this mask could be exposed for over 4µm of semiconductor etch where in indium phosphide with the fast ICP etch there is a selectivity of 12:1 and in the quaternary layers a selectivity of only 5:1. Therefore a thickness of 600nm was chosen to ensure that the mask is not removed unintentionally. This deposition uses the PECVD as described in section 5.1 to produce the start of the process in figure 6.1(b).

6.1.2. Mirror mask definition

The first step of photo lithography is to define the areas where there will be only a passive waveguide. These areas are larger than the waveguides so that exact alignment is not as important later on. 300nm of lift off resist (LOR3B) is used with photoresist of thickness 0.5µm (S1805) to leave photoresist only where there will be passive waveguides. The only alignment required is for the optical mask (figure 6.1(a)) to be aligned with the sample crystal plane so that the cleaving

7. Move the sample horizontally to the next position for cleaving and repeat the above steps to create the cleaving marks.
8. Place the sample face down on a sheet of acetate so that the waveguides are touching the acetate.
9. Cover the sample and acetate with a piece of low-tack tape, ensuring that the sample is held firmly.
10. Place the taught acetate over a blunt knife edge with the scribe marks facing up.
11. Gently bend the acetate and sample on the blunt knife edge until the sample cleaves.
12. Move the acetate from side to side until the sample has cleaved at all of the marks.

This method works well as the sample has a bending force applied over the whole of it's width by the low-tack tape rather than in other techniques where the bending force is only applied at the edges. The spread of bending force means that the cleavage occurs at the weakest point on the sample, which will be where the marks have been scribed rather than at the point of a sharp knife edge which may not be at the same position.

5.12. Wire Bonding

The wire bonding machine creates a ball bond at one end of the gold wire and a wedge bond at the other. This creates an electrical contact between the two ends of the wire. The power, force and time of each of the bonds can be specified and the closer in heights each of the bonds is, the more likely it will succeed.

during if required, and after the TFG etch to remove any polymer layer protecting the nickel. Once this is complete there should be semiconductor visible only where there will be passive waveguides as shown in figure 6.2 and the profile is shown in figure 6.1(g). It is important that the face that will be the mirror is smooth. The

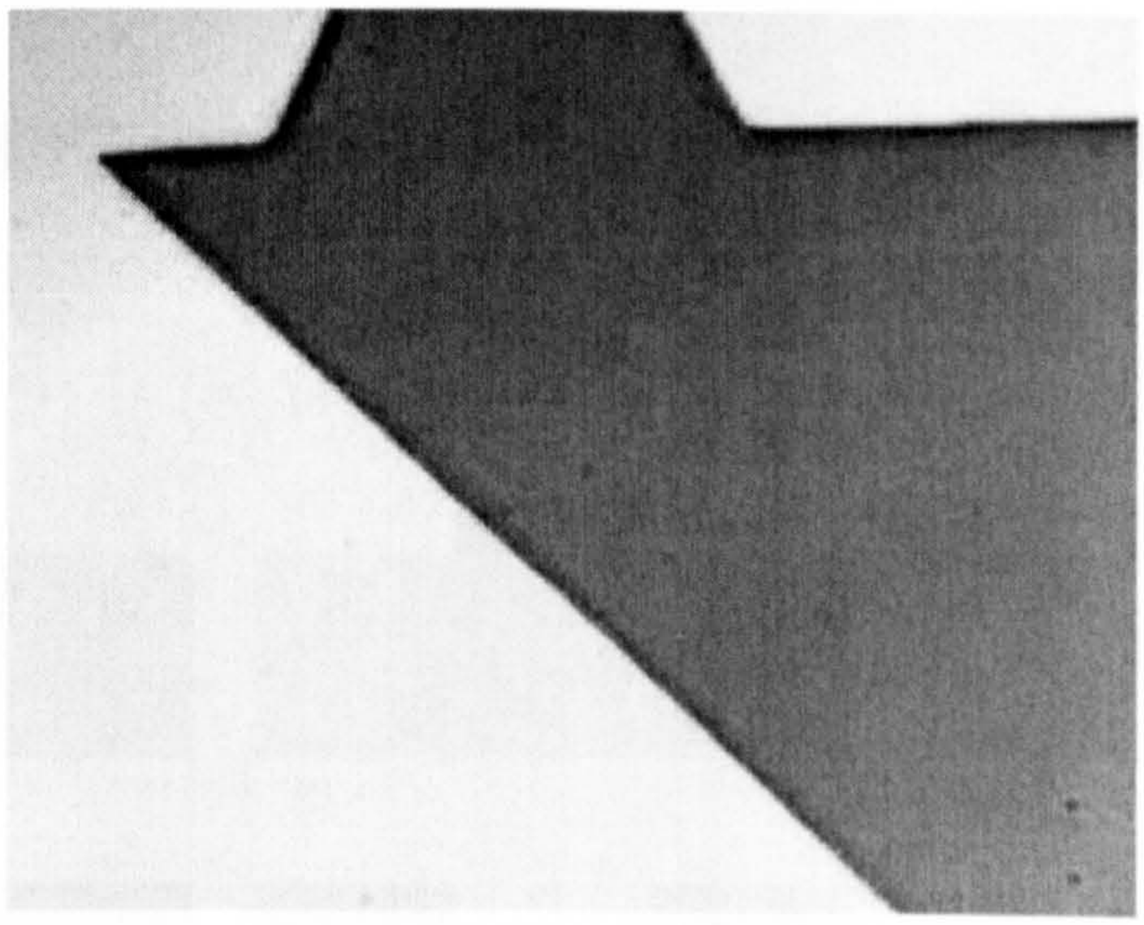

Figure 6.2: Mirror mask definition complete

mask and process above is shown is figure 6.1.

6.1.3. Waveguide mask definition

The next stage uses the liftoff resist LOR3B and normal resist S1805 to define the waveguide mask (Sections 5.2.3 and 5.2.1). This is a difficult alignment step as the mirrors must be in line with the cross in the waveguide to work correctly and only have a tolerance of $\pm 0.25 \mu m$. Once the photo resist has developed well there should be no resist everywhere there are waveguides. The mask used is shown in figure 6.3(a) and the profile at this stage is shown in 6.3(b).

50nm of nickel is then evaporated onto the sample (section 5.3 giving the profile in 6.3(c). Sections of the nickel are then lifted off via the liftoff process in section 5.4 to produce the profile shown in 6.3(d).

The exposed silicon dioxide is then RIE etched (section 5.5) for 35 mins as before to give the profile in 6.3(e).

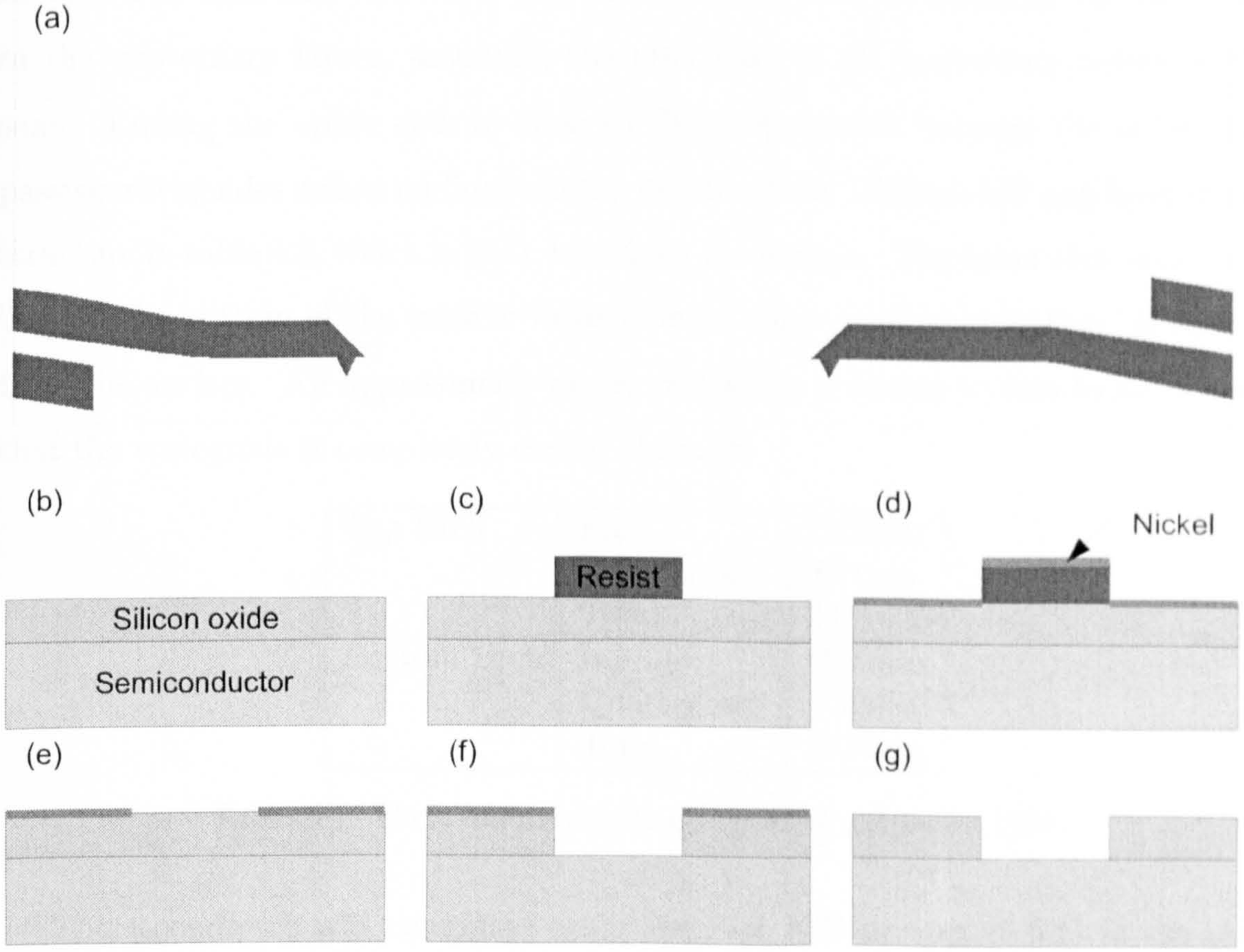

Figure 6.1: Mirror mask definition. (a) Single device mask (b) After silicon oxide deposition (c) After photo lithography (d) After nickel evaporation (e) After liftoff (f) After RIE etch (g) After nickel removal.

works correctly and is not a difficult task. The lithography process is explained in section 5.2.3.

Once there is a good photoresist mask (figure 6.1(c)) 50nm of nickel is evaporated onto the sample, as explained in section 5.3(figure 6.1(d)), then lifted off as described in section 5.4. There will now be a thin layer of nickel everywhere except where there will be passive waveguides as shown in figure 6.1(e).

Now there is a nickel mask for the RIE etching of the silicon oxide. The etch is described in section 5.5 where it is etched for 35 mins at $20nm/min$. After checking that all the silicon oxide has been removed under an optical microscope the profile should look like figure 6.1(f), the nickel is removed by wet etch in TFG. TFG contains sulphuric acid which does slowly etch indium phosphide so etch for no longer than 10 mins. A 5 min oxygen ash clean (section 5.6.3) is performed before,

in use. The difference in overall etch rates can be used to calculate the etch rate in the quaternary layers, assuming the etch rate of all quaternary layers is the same. Ending the upper etch as close to the centre point between the active and passive waveguides means ending it in the middle of the 1200nm InP gap layer in the structure in table 4.3, which is 2411.4nm from the surface. The lower etch must stop beyond the bottom of the passive waveguide so must reach greater than 3741.4nm from the surface. An approximate excess of 600nm is added to this to be certain that the waveguide is completely etched through.

Top Etch	Inp	1800nm
	Quarternary	611nm
	Total	2411nm
Bottom Etch	Inp	1200nm
	Quarternary	730nm
	Total	1930nm

Table 6.1: Etch requirements grouped by material type

The second etch will be etched using the Fast ICP process (5.6.1) as the only mask will be silicon oxide. This process has an InP etch rate of 1400nm/min and a quaternary etch rate of 592nm/min. It will need to etch for 2411.4nm from the surface to make the top etch end at the correct place. This corresponds to an etch time of 2 min 19 s, which is calculated from the above etch rates and table 6.1. Working backwards from the end of the bottom etch it will take 2 min 5 s to etch the whole of the bottom etch (1930nm) and a further 326.7 nm of InP in the extra 14 s. This means that the first etch must end 326.7nm above the end of the top etch, which is a depth of 2084.7nm. The first etch uses the fast RIE etch process (5.6.2) which has an etch rate of 50nm/min in InP and 23.7nm/min in quaternary. This means that the first etch should last 55 min 16 s. The first etch is insensitive to different etch rates for varying material, however the second etch is more sensitive. As long as the ratio between etch rates stays constant it doesn't matter if the overall rate alters.

The first etch lasts 55 min 16 s using the fast RIE etch process and the etch depth checked. It is etched for longer if required. The profile at this stage is shown in figure 6.3(f) with a depth of $2084.7 \pm 50nm$ into the semiconductor. After this, the nickel is removed using a combination of oxygen ash cleaning and TFG as before

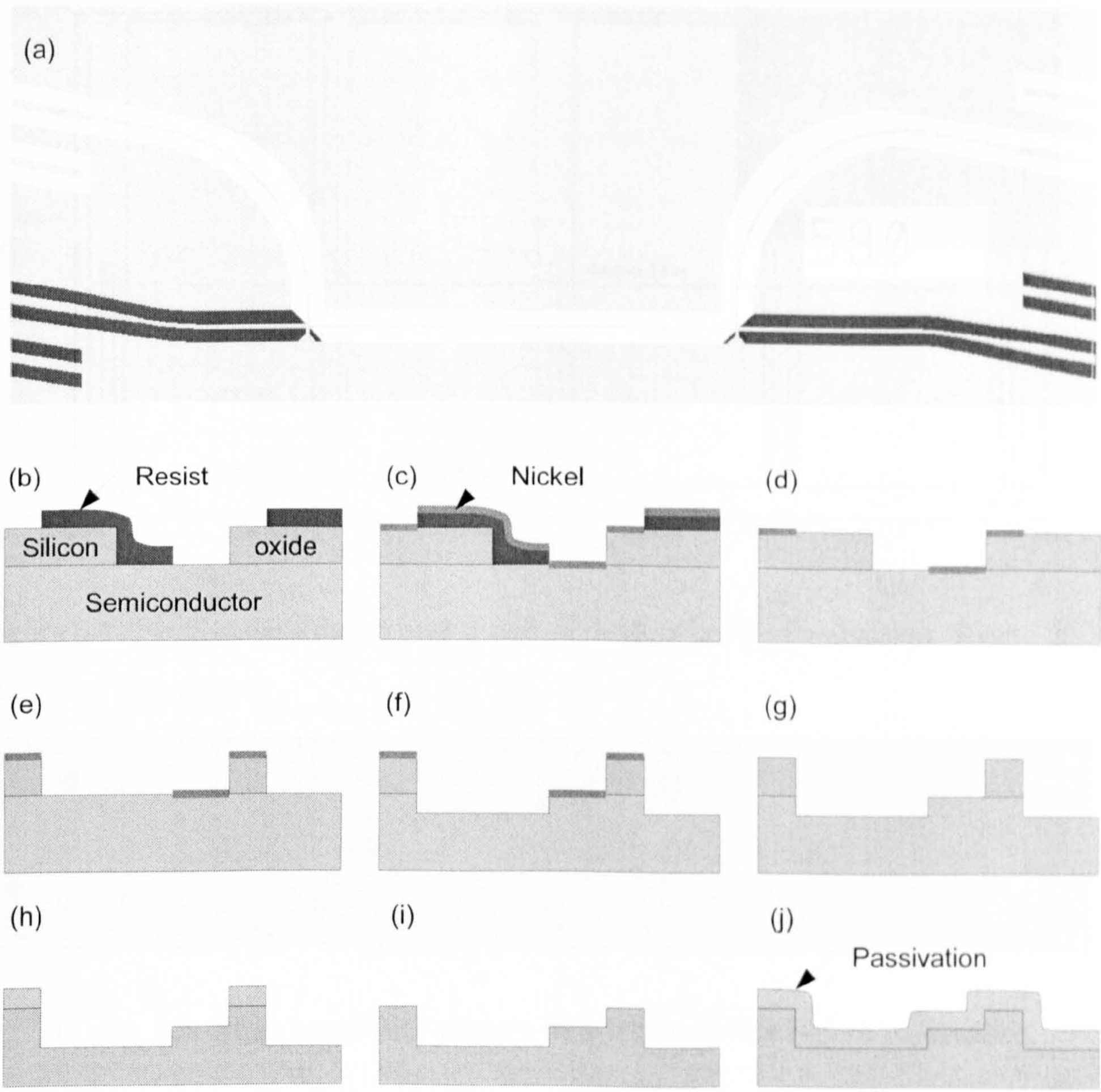

Figure 6.3: Waveguide mask definition. (a) Single device mask overlay (b) After photo lithography (c) After nickel evaporation (d) After liftoff (e) After RIE etch (f) After fast RIE semiconductor etch (g) After nickel removal (h) After fast ICP semiconductor etch (i) After silicon oxide removal (j) After passivation deposition.

6.1.4. Semiconductor etch

The sample is now at the stage where the semiconductor is to be etched. The first etch must use the fast RIE etch process outlined in section 5.6.2 as there is a nickel mask that higher power ICP would sputter. As there are two masks, calculating the etch depths is a little complicated. The etch rates for the different etches must be known for the different materials in the semiconductor. These were found by running the etches on pure indium phosphide and also through the actual structure

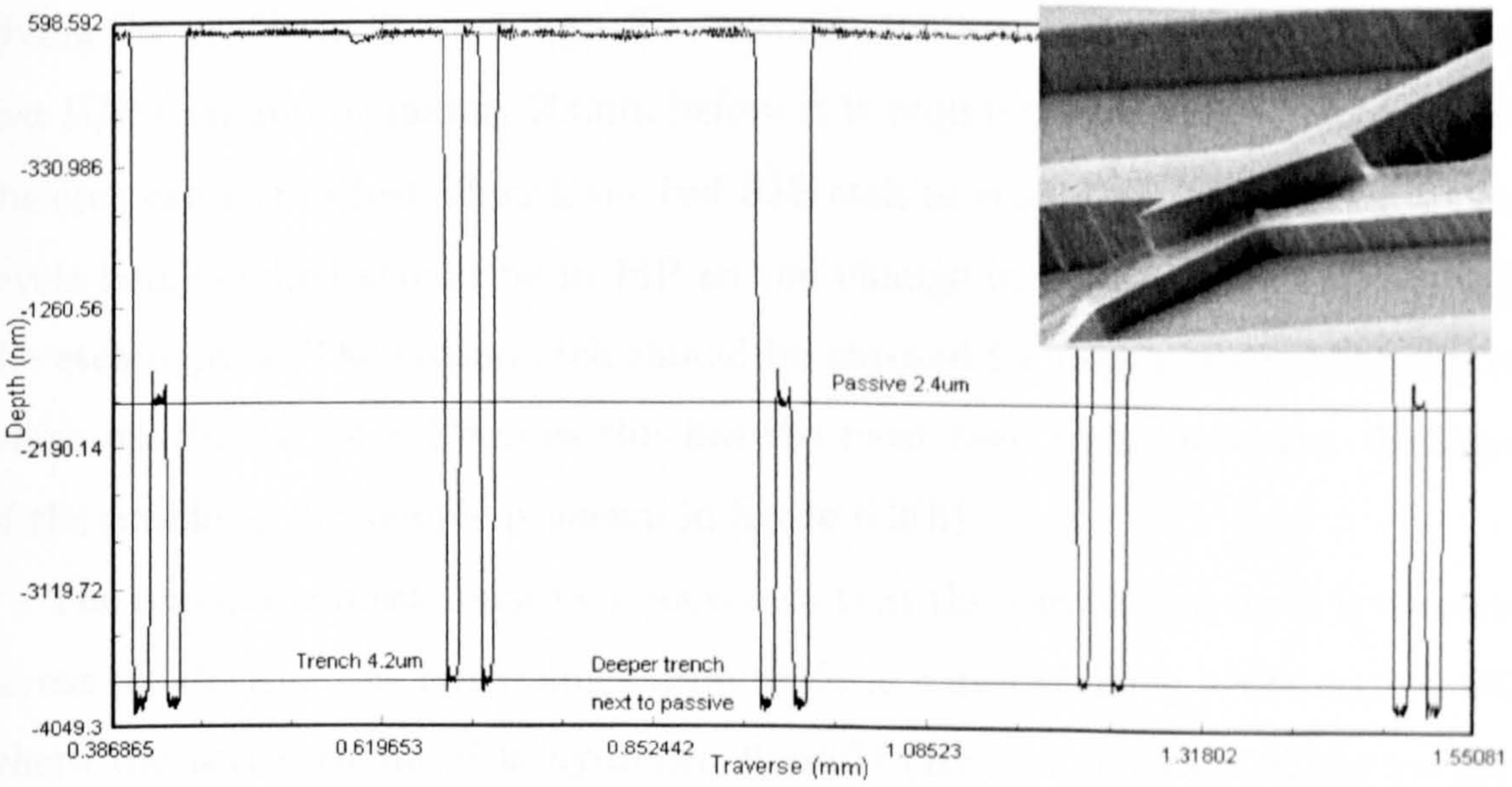

Figure 6.4: Profiler data dump over a pair of devices before passivation. Inset: SEM picture of one mirror.

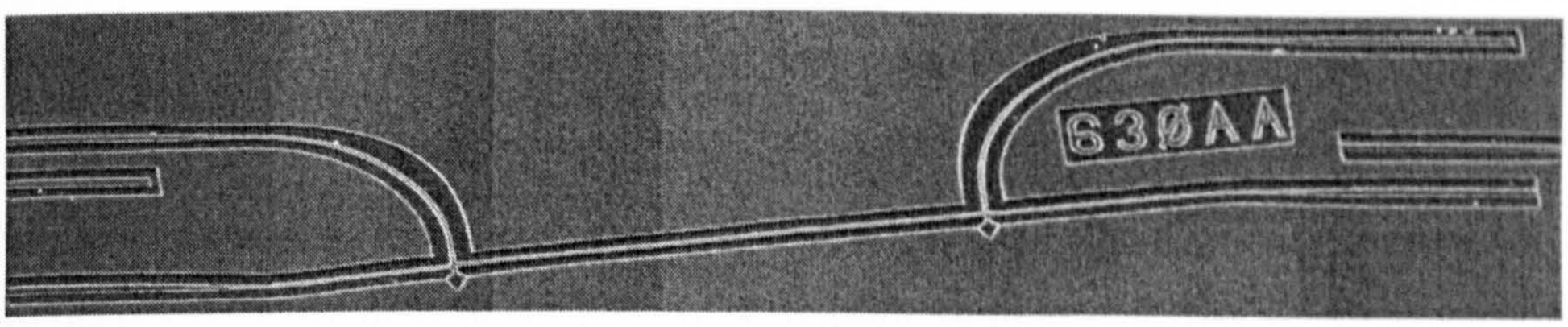

Figure 6.5: SEM composite picture of a whole device before passivation

resist, S1813, is used in the photo lithography step to pattern the mask shown in figure 6.6(a). The photo lithography will self align if it is purposefully underexposed slightly as the resist on the top of the waveguides is thinner than in the trenches. Once the resist pattern is good, the sample is placed in an oven set to 120°C for 30 min. This is called hard baking and increases the toughness of the resist for use as an etch mask. The profile after hard baking is shown in figure 6.6(b).

The contact windows must then be RIE etched though to the semiconductor which is an etch of 15 min. The profile of the sample will then be as in figure 6.6(c).

Once the RIE etch is complete, the remaining photo resist is removed in acetone in an ultrasonic water bath. The profile is shown in figure 6.6(d).

giving the profile in figure 6.3(g). The second etch is completed aiming to stop the fast ICP etch approximately 200nm before it is required (9 s short). The last bit of the etch can be finished off with the fast RIE etch to ensure an accurate finish. Both levels being etched should be in InP so the change in etch process will not affect the etch depths. The second etch should be checked for depth against the top etch which will be $2411.4 \pm 50nm$ as this has the most need to be accurate. A diagram of the profile of the sample is shown in figure 6.3(h).

The remaining mask must be removed so that the passivation layer is consistent across the device. The remaining silicon oxide is removed using a wet etch in BOE, where the active chemical is hydrogen fluoride (HF). A diagram of the profile of the bare semiconductor is shown in figure 6.3(i). The measurements and an SEM picture are shown in figure 6.4 where a 'fence' can be observed around the edges of the middle level. This 'fence' is formed due to a residual mask being left on the sidewalls after the first etch when the nickel is removed. The 'fence' is very thin, so will not affect the optical properties of the device and it should cause no problem with the passivation layer. It can also be observed from the profiler data that there are deeper trenches next to the passive waveguide than next to the active waveguide. This is because of the oversized gap in the mask for the passive waveguide causing the semiconductor surface to be etched slightly during the second oxide mask etch. This deeper trench will also not affect the optical properties significantly as the waveguides are deep etched.

6.1.5. Passivation deposition

200 nm of silicon nitride was chosen as the passivation layer as the deposition process seemed stable and nitride is harder wearing than oxide. Only a thin layer is required as it is not being used as a mask, only as an insulating layer between the contacts and the semiconductor. The nitride process is described in section 5.1 and the profile is shown in figure 6.3.

6.1.6. Window definition

The next stage is to define the contact windows which allow the p contact to make an electrical connection to the surface of the semiconductor. The normal photo

in figure 6.7(a). A cross section of the device is shown in figure 6.7(b) after successful photo lithography.

The p contact layers are deposited using the procedure and recipe in section 5.8 to produce a cross section shown in figure 6.7(c).

After deposition the unwanted metal can be removed by liftoff to give separation between the contacts. The cross section that this should produce is shown in figure 6.7 where there is continuous contact over the contact windows and separation between neighbouring contacts.

6.1.8. Thinning down

The sample is thinned down from the back (n side) to less than 200µm using the technique explained in section 5.9.

6.1.9. N Contact layers

The n contact layers are deposited as described in section 5.8 which allows the devices to have basic IV (current and voltage) measurements taken before annealing.

6.1.10. Anneal

Before annealing there are bad electrical contacts between the contact layers and both sides of the semiconductor. This shows up on the IV curves as a high dynamic resistance of the device. Once the device has been annealed well, the metal will diffuse into the surface of the semiconductor, the dynamic resistance will drop and there should only be a single diode characteristic in the curve which will be the optical device. If there is a second diode characteristic shape it is likely that the annealing has not been completed successfully leaving a metal-semiconductor (Schottky) junction. The annealing curve with the minimum temperature required for good annealing is shown in section 5.10. It is best to use a lower temperature for annealing if possible as higher temperatures can cause damage to other parts of the device.

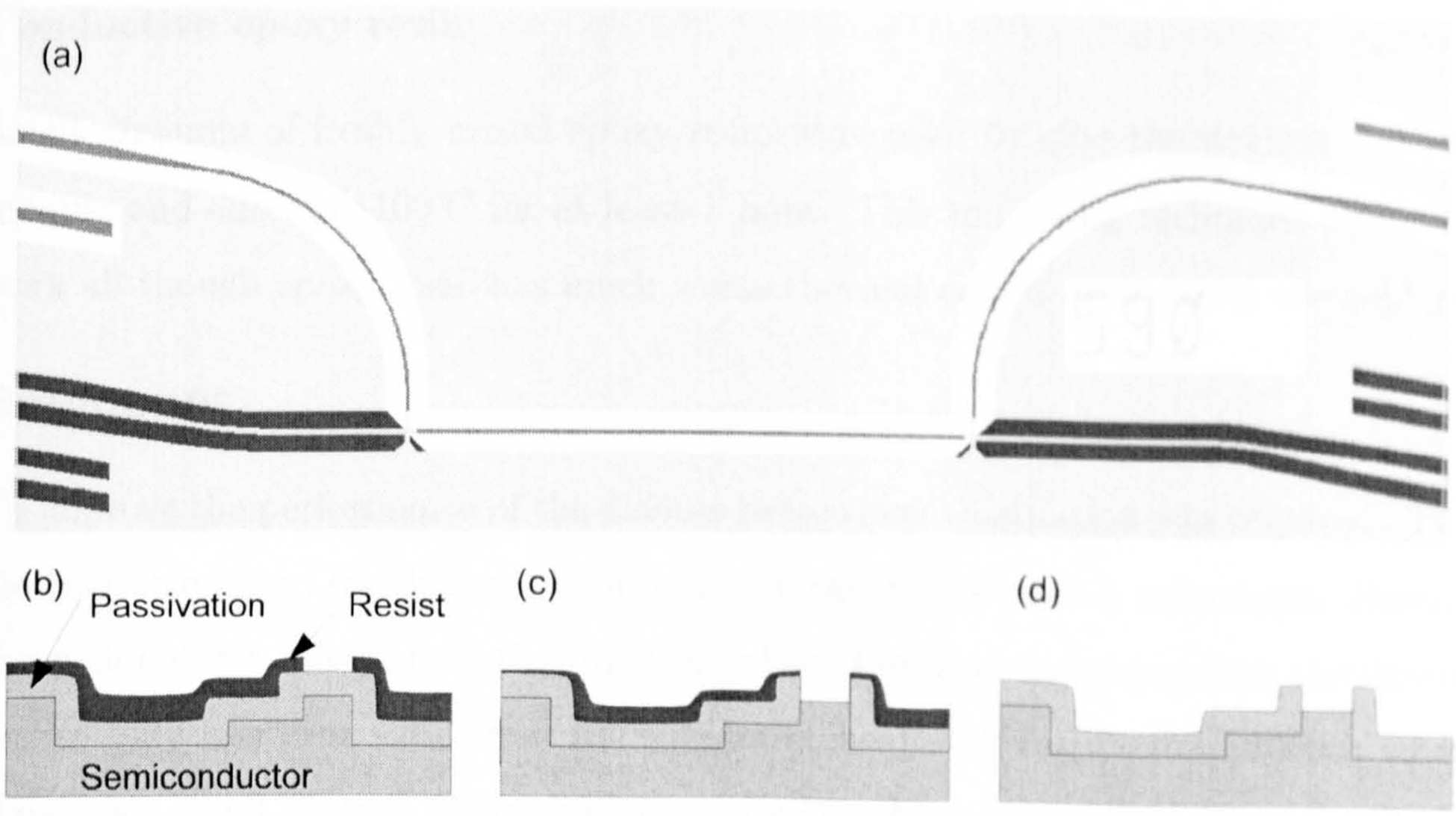

Figure 6.6: Window mask definition. (a) Single device mask overlay (b) After photo lithography (c) After RIE etch (d) After resist removal

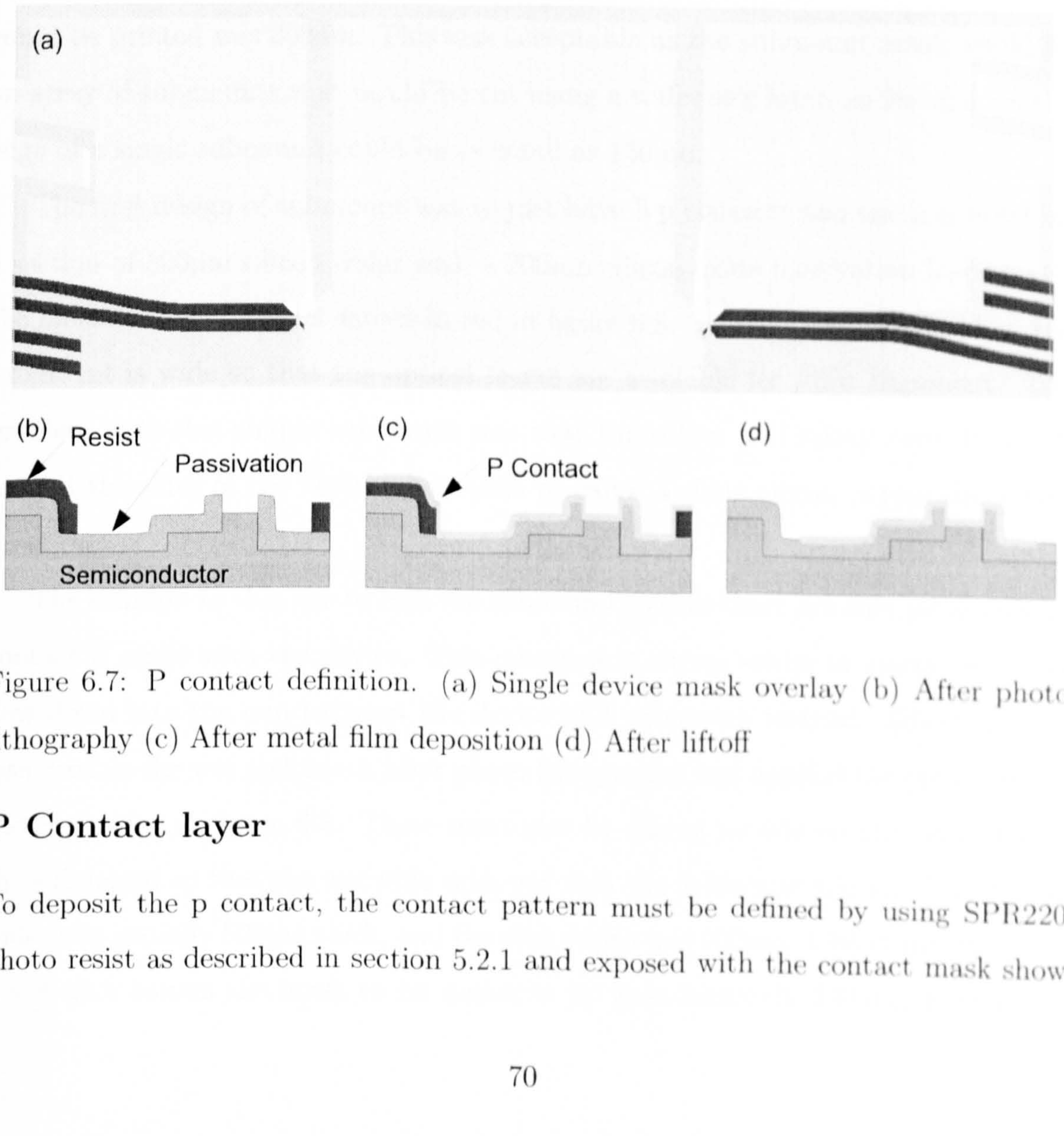

Figure 6.7: P contact definition. (a) Single device mask overlay (b) After photo lithography (c) After metal film deposition (d) After liftoff

6.1.7. P Contact layer

To deposit the p contact, the contact pattern must be defined by using SPR220 photo resist as described in section 5.2.1 and exposed with the contact mask show

Conductive epoxy resin

Small amounts of freshly mixed epoxy resin were used to glue the devices to their mounts and cured at 100°C for at least 1 hour. This mounting technique seems to work all though epoxy resin has much worse thermal conductivity than the solders.

6.2.2. Submount

To improve the performance of the devices better heat dissipation was required. The method attempted for this was to flip-mount the device onto a submount. Having the p side down means that the junction where the heat is produced in the device is now only less than 2µm from the submount heat sink rather than 200µm when the device is not flipped. This should improve the heat dissipation dramatically.

For speed of development the submount optical masks were produced on acetate using a high accuracy plotter that is normally used to create the masks for printed circuit board manufacture. This method meant that the smallest feature size that could be printed was 300µm. This was acceptable as the submount mask would be an array of submounts that would be cut using a wafer saw later, so features on the edge of a single submount could be as small as 150µm.

The first design of submount was to just have 3 p contacts and one n contact on a section of 500µm silicon wafer with a 200nm silicon oxide passivation layer under the metal contact. This is shown in red in figure 6.8. The device is longer than the submount is wide so that the optical facets are available for fibre alignment. The problem with this simple submount was that the solder and epoxy resin flows up around the sides of the device and seems to cause a short circuit across the active junction.

The solution to this was to etch the submount so that there are only pillars where contact is made with the device. This means that excess solder or epoxy resin will flow down into the gap between the device and submount instead. Silicon nitride was used as the wet etch mask after photo lithography had applied the optical mask shown in blue in figure 6.8. There must also be silicon nitride on the back side of the submount so that the wet etch does not thin the submount too far. The silicon wafer was initially 500µm thick, and the etch depth was 200µm. Unfortunately using a wet etch causes the mask to be undercut by approximately 200µm, so that the

6.1.11. Gold deposition

After annealing an extra layer of 200nm of gold is sputtered onto the n-contact to allow wire bonding onto that surface to take place.

6.1.12. Cleaving

The sample is cleaved into separate devices by scribing marks along the orientation that is to be cleaved then bending the sample using some low tack adhesive tape on some acetate. The adhesive tape applies an equal bending force over the sample so that the sample cracks at each of the scribed marks and the crack propagates along the crystal cleavage plane.

The devices are now ready to be mounted and tested.

6.2. Device mounting

6.2.1. Mounting with the n side down

A few different methods were used for mounting the devices for testing. They are described below.

Lead-tin solder

Lead-tin solder was used to mount the devices n side down. Normal electrical solder was cut into small pieces and placed on a gold plated copper mount. The mount heated to 200°C to melt the solder on a die bonding machine and the device positioned onto the solder. This method was also used with small amounts of solder paste. Unfortunately the solder did not wet onto the devices, which meant that it was only the solder flux holding them on which is not a good electrical conductor.

Gold-tin solder

Small amounts of gold-tin solder were cut up and placed on a gold plated copper mount. The mount was heated to 320°C and the n side of the devices were soldered to the mount. Unfortunately there did not seem to be enough strength in the solder as it would crack when the wire bonder was used.

pillars become very small.

Both types of solder are not strong enough to hold the device onto the submount as they crack off when wire bonding it attempted. Epoxy resin seems to hold well but it was not possible to test this mount with a working device.

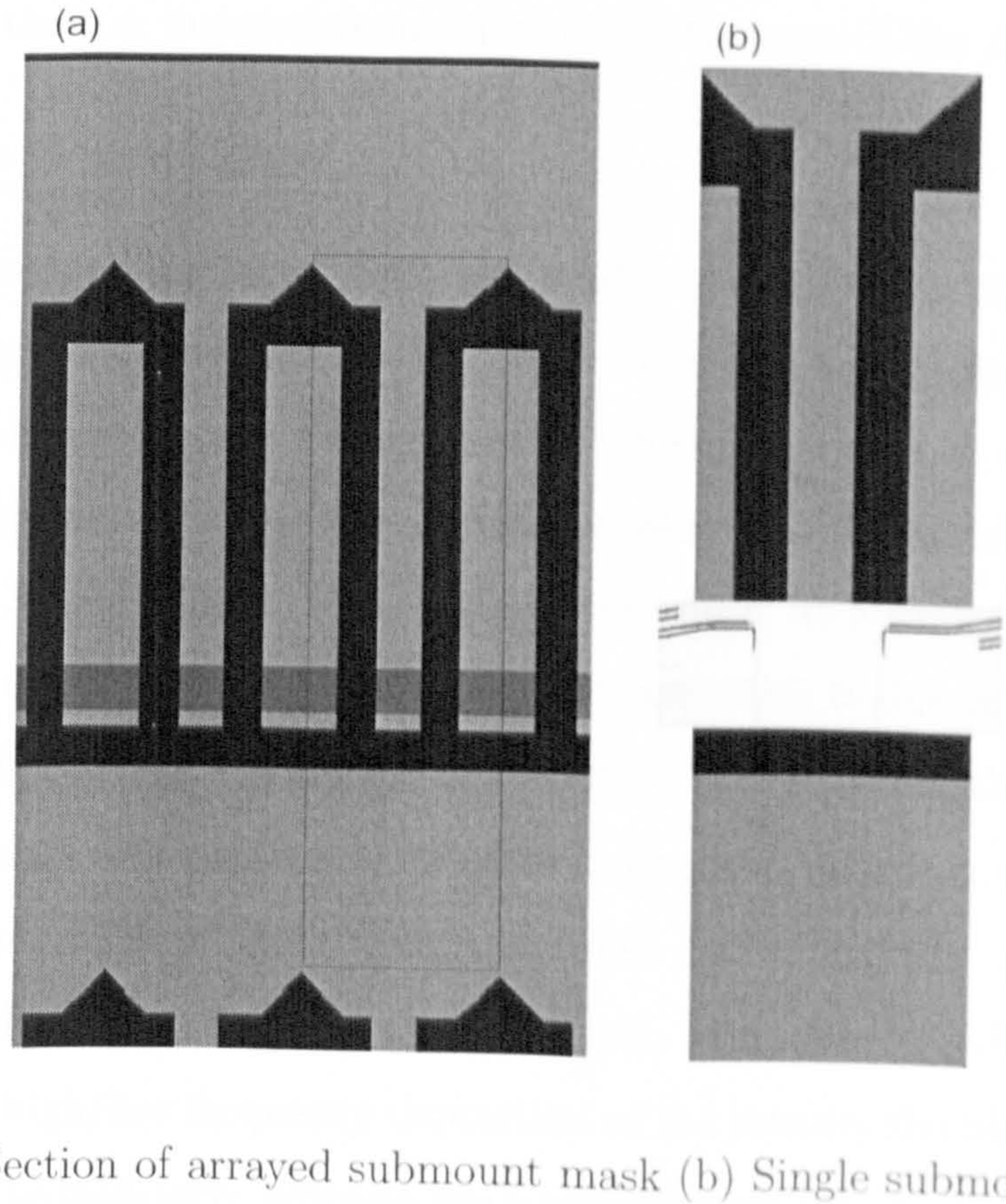

Figure 6.8: (a)Section of arrayed submount mask (b) Single submount with device mounted overhanging the sides

6.2.3. Wire bonding

Once a device is mounted wire bonds are required to make a contact between the top contacts of the device and large contact pads on the mount. This is so that probes can be used on the contact pads without the possibility of damaging the waveguides. Wire bonding is explained in section 5.12.

6.3. Fabrication Obstacles

A selection of the obstacles encountered during the fabrication of the devices are described in this section.

6.3.1. Junction losses

During the first round of devices the first etch used a previous RIE etching recipe that had an etch rate of only 20 nm/min. It was discovered that during this etch the sidewalls of the active layer became damaged. This caused a large leakage current to flow around the p-n junction reducing the effectiveness of the device.

6.3.2. Bad nitride deposition

The PECVD machine used for silicon and oxide deposition was upgraded to a new control computer part way through this PhD. The new set up was tested and the processes altered to the new calibrations. Unfortunately there were some faults that did not become clear until the latest samples were annealed. Annealing the sample with a 200nm silicon nitride passivation layer at above 400°C caused the nitride layer to crack off the semiconductor surface. This is due to bad adhesion to the semiconductor so that the nitride cracks due to the different thermal expansion rates of the nitride and the semiconductor. The bad adhesion could have been caused by an intermittent fault that sometimes caused the RF plasma to strike for a few seconds before the gas flows stabilised. The other possible cause is that with the pulsed high/low frequency deposition of the nitride, the high frequency RF source turns on immediately whereas the low frequency RF source seems to have a delay of approximately 2 s that may be variable. This may cause weak layers in the deposition which would also reduce the initial adhesion to the semiconductor.

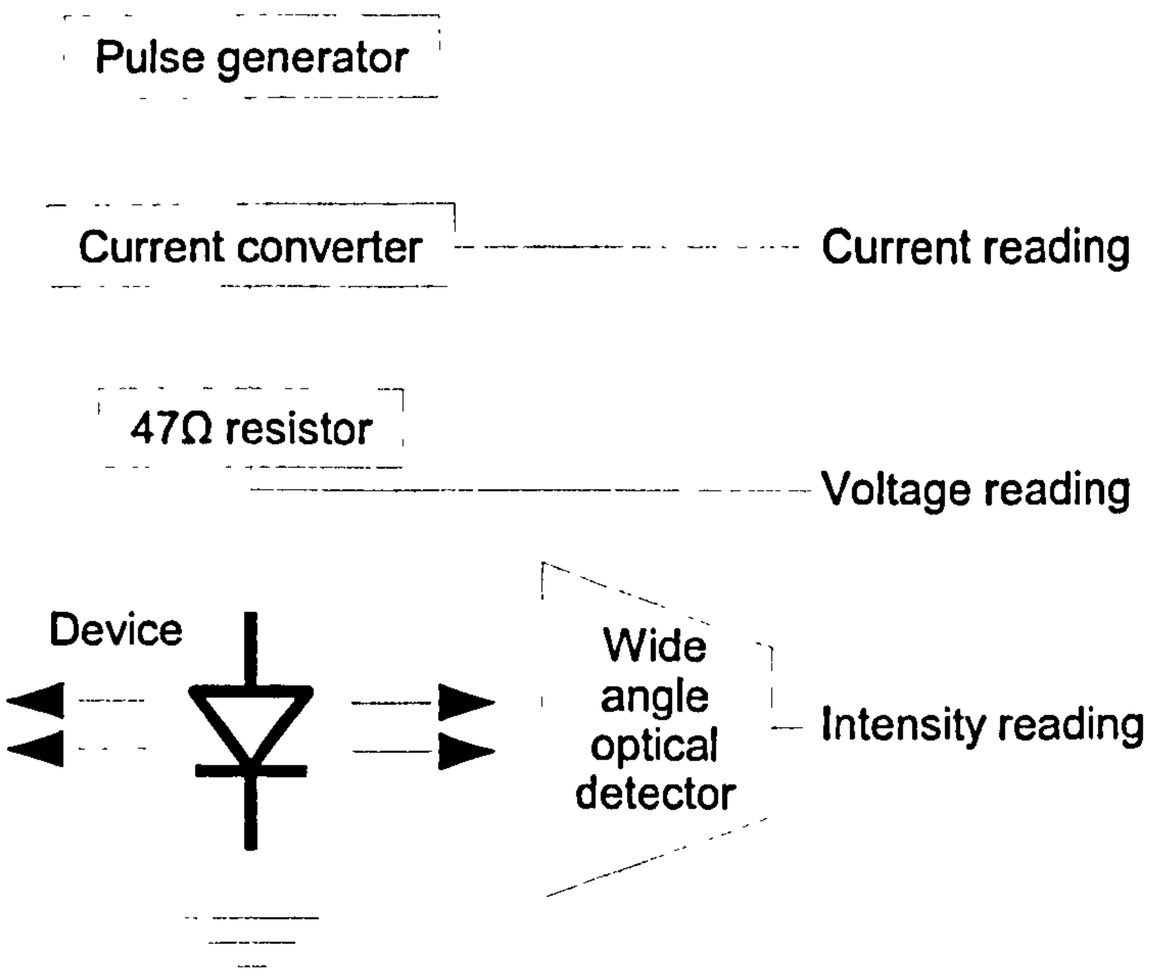

Figure 7.1: LIV experiment setup

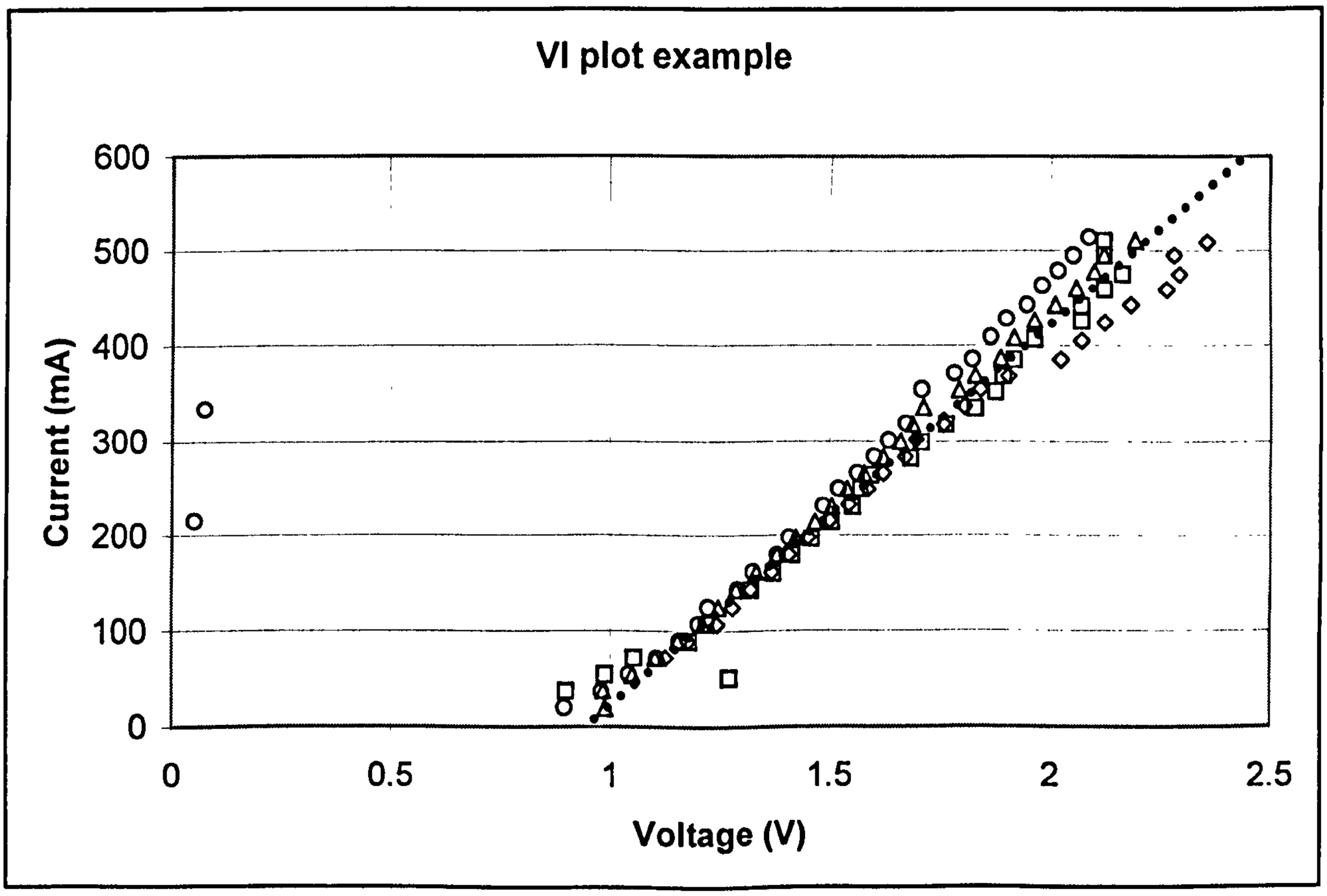

Figure 7.2: IV graph for an 800μm device

bandwidth of the detector. The drive current verses optical power graph (IL) gives information about the threshold current for lasing of the device which is desired to be as high as possible as the device is being used as an amplifier. The black traces in figure 7.3 show the ASE coupled into a wide angle power meter head, out of three

Chapter 7

Characterisation

7.1. Electrical Characteristics

The initial test for all the devices is to measure the electrical characteristics. This is achieved using the setup in figure 7.1 without the optical detector attached. This test can screen all of the devices and some problems can be diagnosed if the VI graph does not fit a typical forward biased diode. If the VI graph is a straight line with an x-axis intercept of 0V then the p-n junction has short circuited so the device is only a resistor. If the voltage increases dramatically with current then there is an open circuit. If the probe and wire bonding contacts are good then it is most likely that the thinnest part of the device contact layer has overheated and become open circuit there. This is usually the sidewall of the ridge, so can be recovered by placing a wire bond on to the other side or on top of the ridge. If there are two diode characteristics superimposed on one another it is likely that the one with a low junction voltage of around 0.2V and a high dynamic resistance will be a metal-semiconductor (Schottky) diode junction at the p-contact. This, or a high dynamic resistance in a single diode characteristic suggest that the p-contact has not diffused into the semiconductor well, so the device needs annealing at a higher temperature. The VI graph shown in figure 7.2 shows a good selection of data. The junction voltage of the device is 0.9V which is a good value for these devices and the dynamic resistance is 2.5Ω, which is a good low value so should work well as it has a good forwards biased diode characteristic.

7.2. Amplified Spontaneous Emission

To measure the ASE, the complete setup in figure 7.1 is used where the power meter has an open, wide angle lens so that all optical power is measured over the

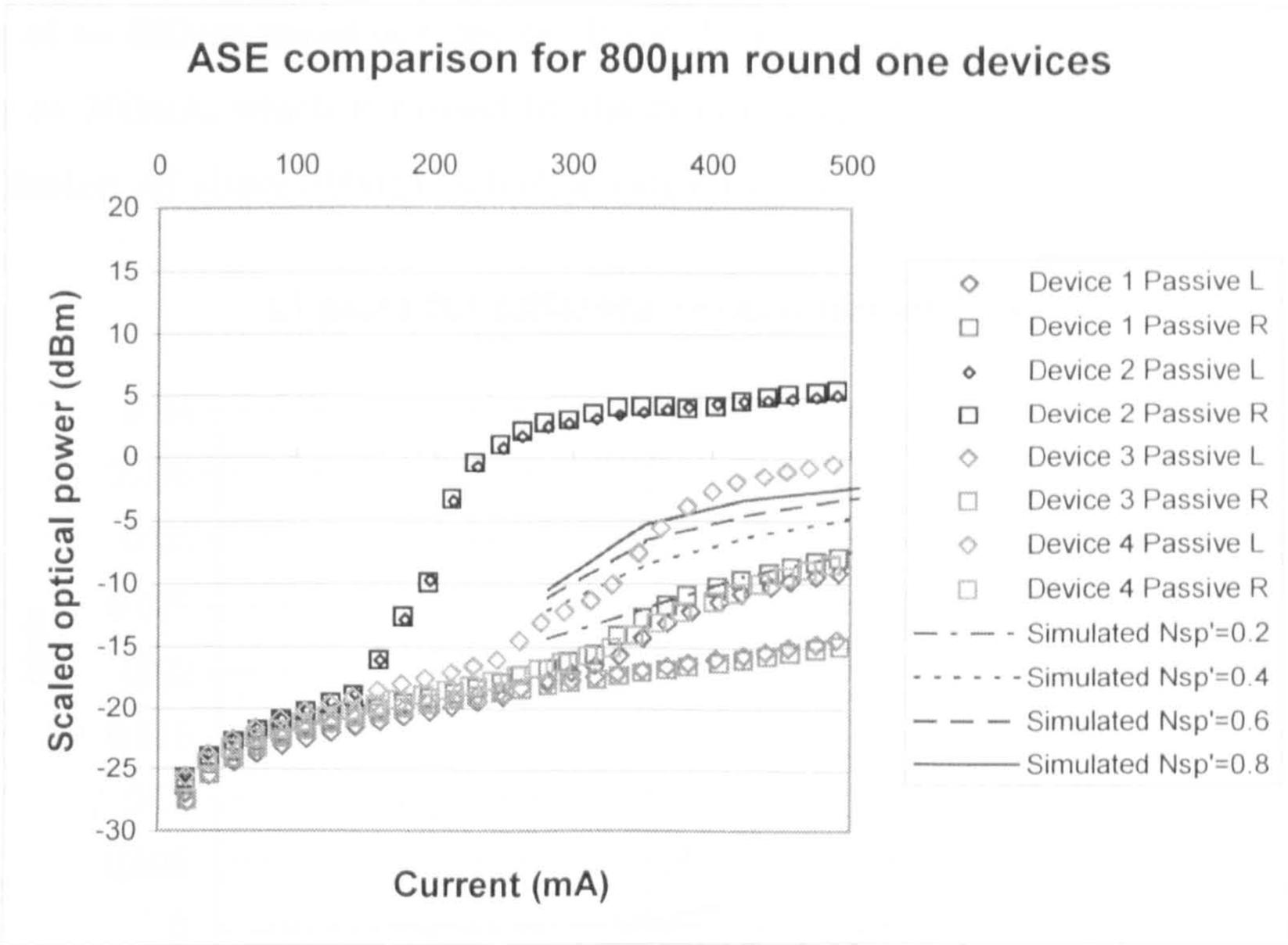

Figure 7.4: ASE comparison between simulation and experimental results for the passive waveguide output of a 800 µm round one device

fibres were used to couple the light in and out of the device as shown in figure 7.7. One set of first round devices had their facets etched on a focused ion beam (FIB) machine at an angle of 5° so that the lensed fibres needed to be angled down towards the device. The Second round of devices had mode expanded angled facets with a pair of waveguides on a single edge of the device. Therefore these devices required angled fibre arrays as shown in figure 7.8.

The angle of the fibre array is calculated using Snell's law from the effective index of the fundamental mode of each waveguide ($n_{active} = 3.272$, $n_{passive} = 3.264$) and the facet angle, $\theta_{facet} = 10^o$. The material on the other side of the boundary will be a single mode fibre as the fibre is butt coupled to the device (simulated in Fimmwave this has an effective refractive index of $n_{fibre} = 1.458$).

facets of an 800µm round one device. It can be seen that all the outputs increase in power at 200mA, which is caused by the device beginning to lase, and the outputs then flatten off above 300mA, which is caused by the saturation of the device.

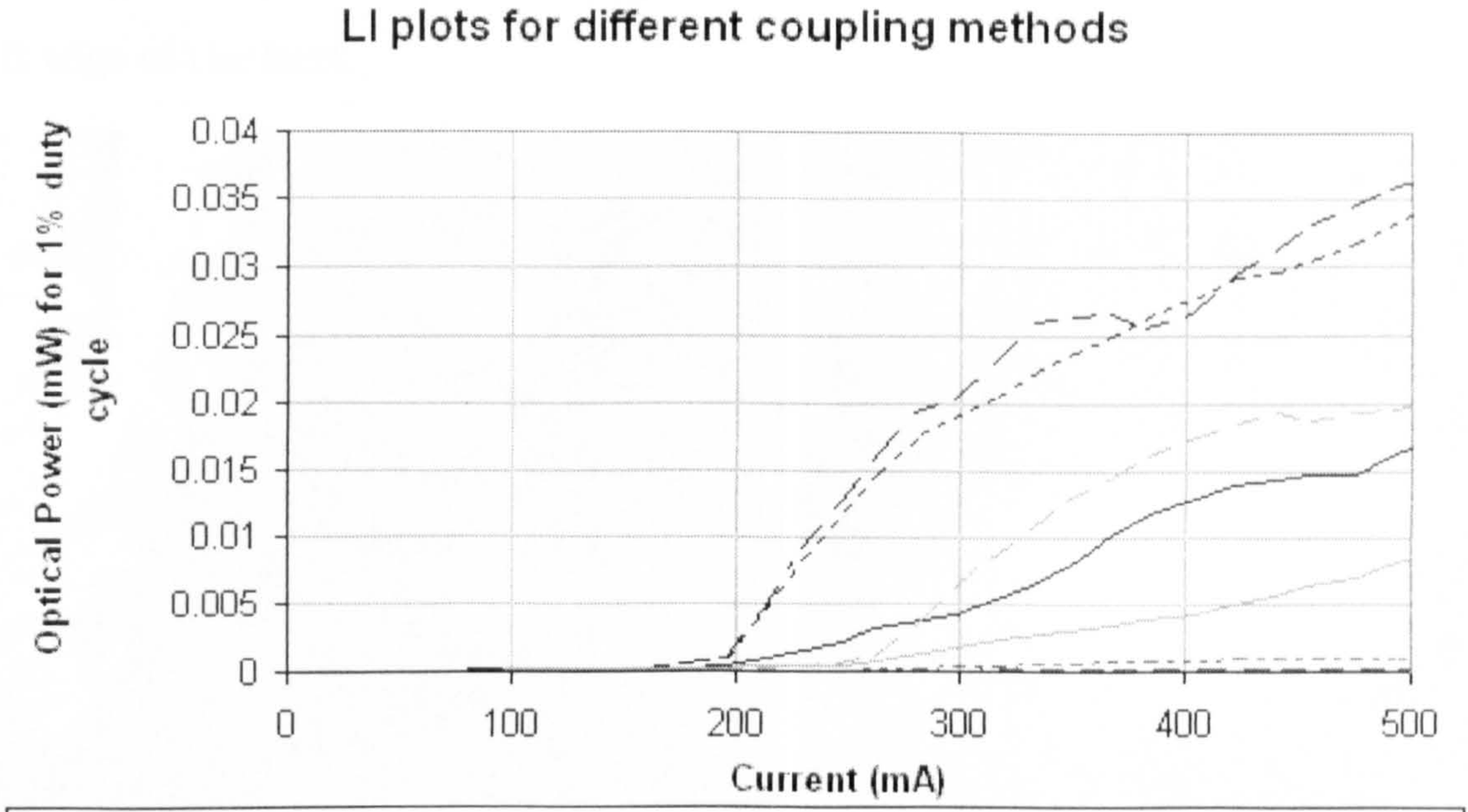

Figure 7.3: IL graphs showing different coupling methods to the power meter

Figure 7.4 shows a comparison of the simulated wide band ASE power with the experimental ASE measured on a wide band power meter for a round one device. It was discovered that the current injection efficiency required for the simulated curves to agree with the experimental results was 10%. This is very low and can be explained by a large proportion of the current not affecting the carrier concentration in the quantum wells. This is explained in section 7.9. Figure 7.5 backs up this hypothesis as the current injection efficiency there is 15% for a round two device. Unfortunately, this means that the predicted useful operating points would be at currents well over 1A which would easily destroy the active junction in the device.

7.3. Fibre Alignment

The next stage of characterisation is for fibres to be aligned to the facets of the device. The first round of devices did not have any tapers or angled facets so lensed

is shown in figure 7.6 alongside a picture of the facet. It can be seen that the lensed fibre has a relatively large coupling area so that the power scan is much larger than the facet. There is some light being detected that is higher than the main spot. This is due to a vertical discontinuity in the facet which can be seen just above the left edge of the facet.

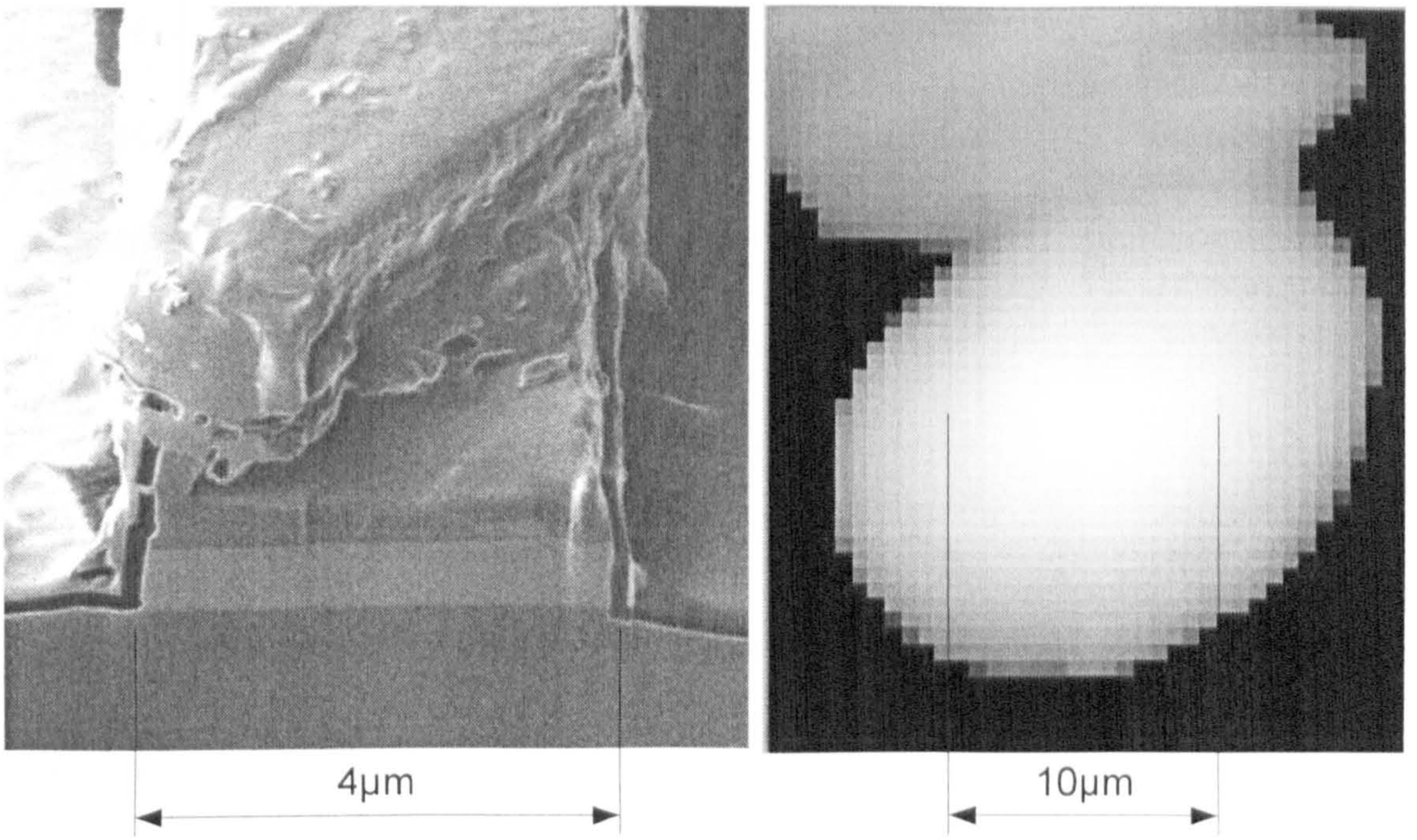

Figure 7.6: Facet picture taken on a FIB and a fibre coupling position scan

A program was also written in Visual Basic to track the position of highest power over time. This was very useful when changing the device mount temperature as the height of the device would move significantly due to expansion and contraction of the mount and stages. Tip, tilt and rotation alignment stages were also required for both types of alignment all though these made most impact with the fibre array as both fibres in the array needed to be at the same height and parallel with the device facet. The arrangement of the alignment stages are shown in figures 7.7 and 7.8.

7.4. ASE in Fibres

Once fibres are aligned the ASE power and spectra can be measured out of each facet. The ASE spectra can be used to find reflective cavity lengths within the device and the ASE power can be compared to the simulation's predicted ASE power. The

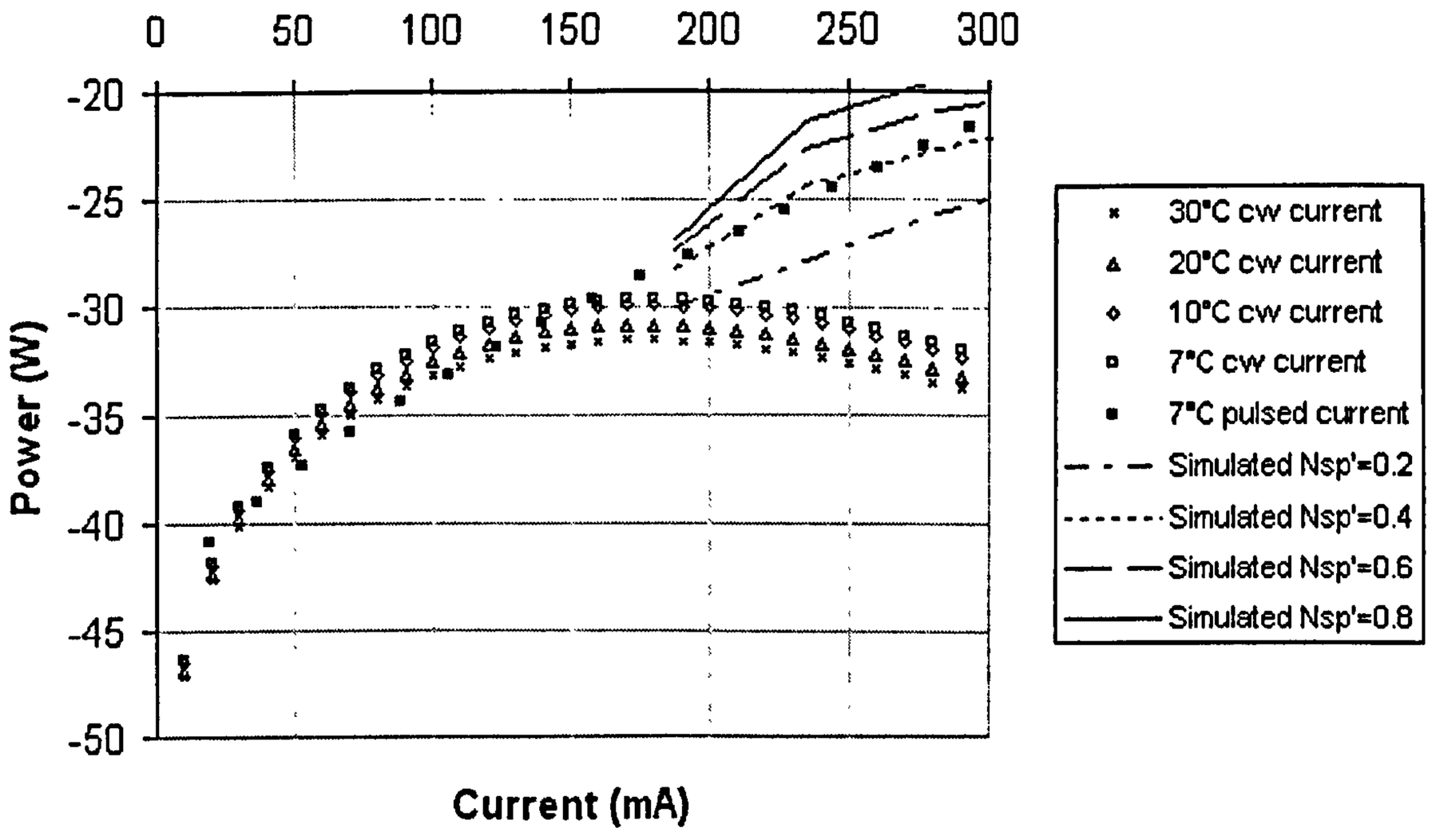

Figure 7.5: ASE comparison between simulation and experimental results for the active waveguide output of a 880 µm round two device

$$n_1\theta_1 = n_2\theta_2 \tag{7.1}$$

$$\theta_{fibre} = \frac{n_{waveguide}\theta_{facet}}{n_{fibre}} \tag{7.2}$$

$$\theta_{fibre,active} = 22.45^o \tag{7.3}$$

$$\theta_{fibre,passive} = 22.40^o \tag{7.4}$$

$$\tag{7.5}$$

The closest fibre arrays available were angled to 23°. This was deemed close enough that the excess loss would be negligible.

Both types of fibre alignment required fine position control to reduce the coupling loss. This was achieved with piezo x,y and z stages that could be controlled over the GPIB bus by a computer. Software was written in Visual Basic to move the fibre in two dimensions reading the ASE power at each position to get a near field pattern, so that the position of highest power could be selected for the position of least coupling loss. A detailed scan of the output power with lensed fibre position

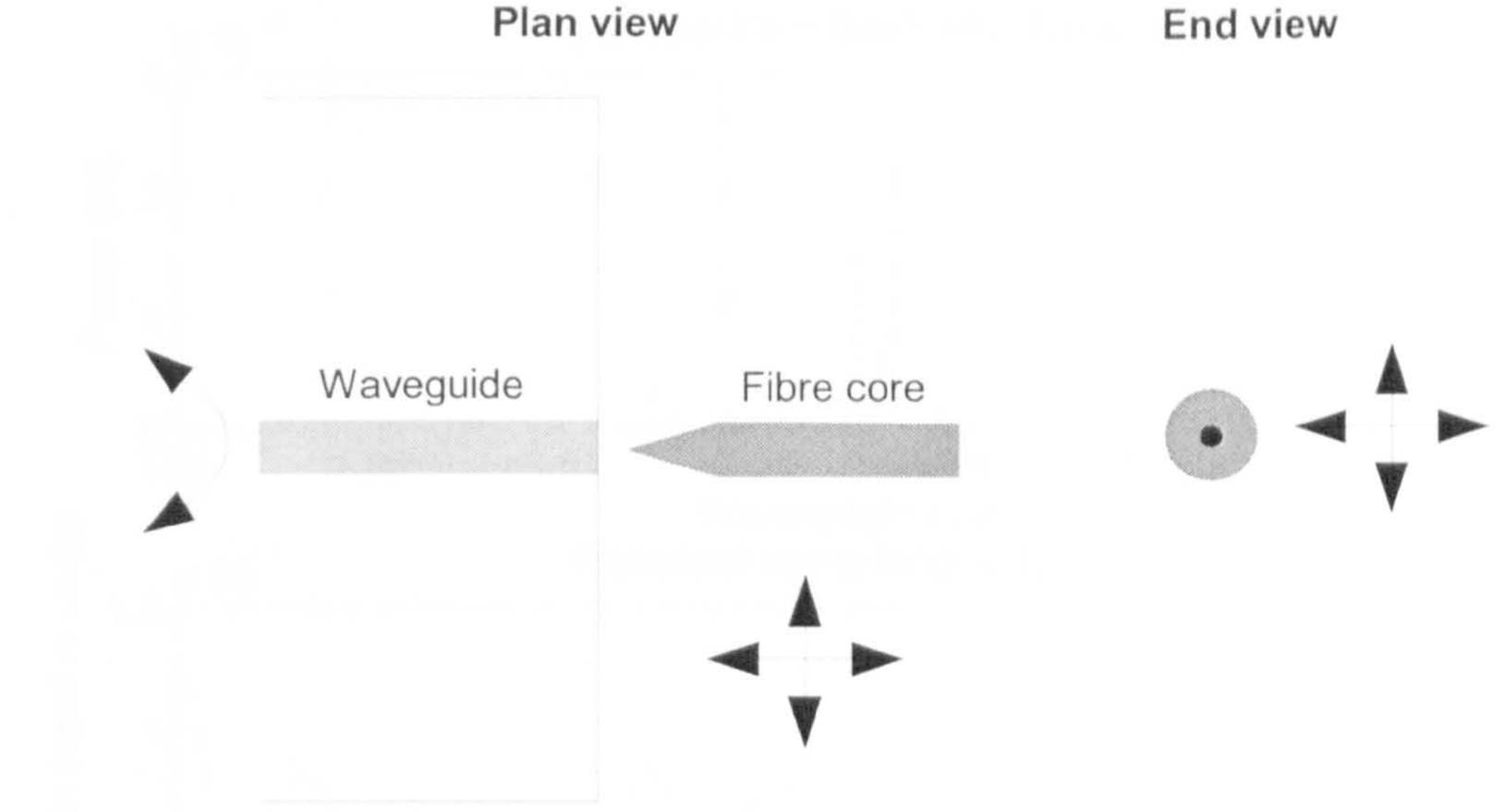

Figure 7.7: Lensed fibre alignment

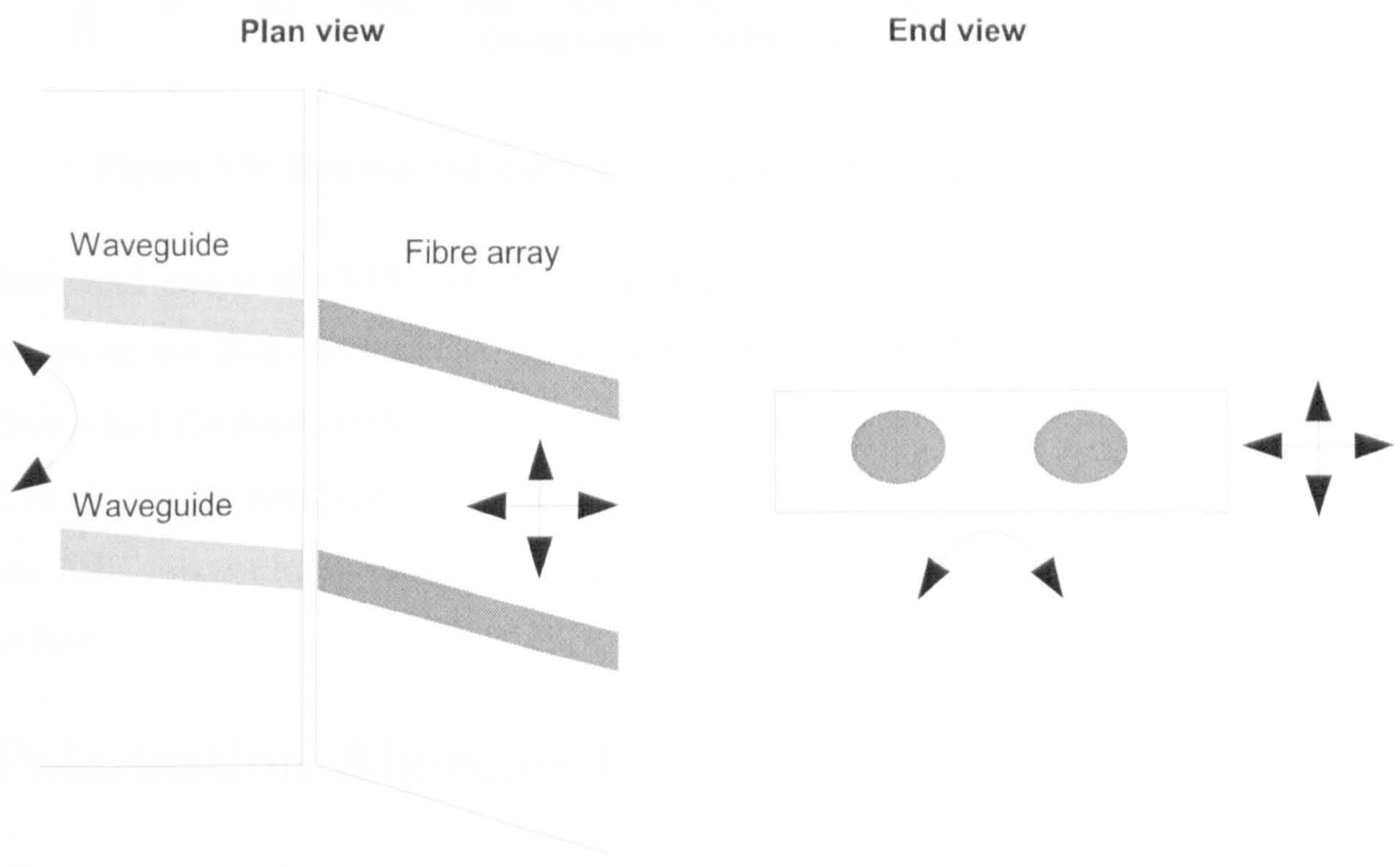

Figure 7.8: Arrayed fibre alignment

spectrum for a device that is exhibiting lasing characteristics is shown in figure 7.9 and the spectrum for a device that is not lasing is shown in figure 7.10. Figure 7.5 shows the ASE power comparison with simulated results.

Figure 7.3 shows the measured ASE output from the same device with an open power meter head, before and after focused ion beam (FIB) etching of the facets at an angle as well as fibres aligned to the angled facets. It can be seen that there is a

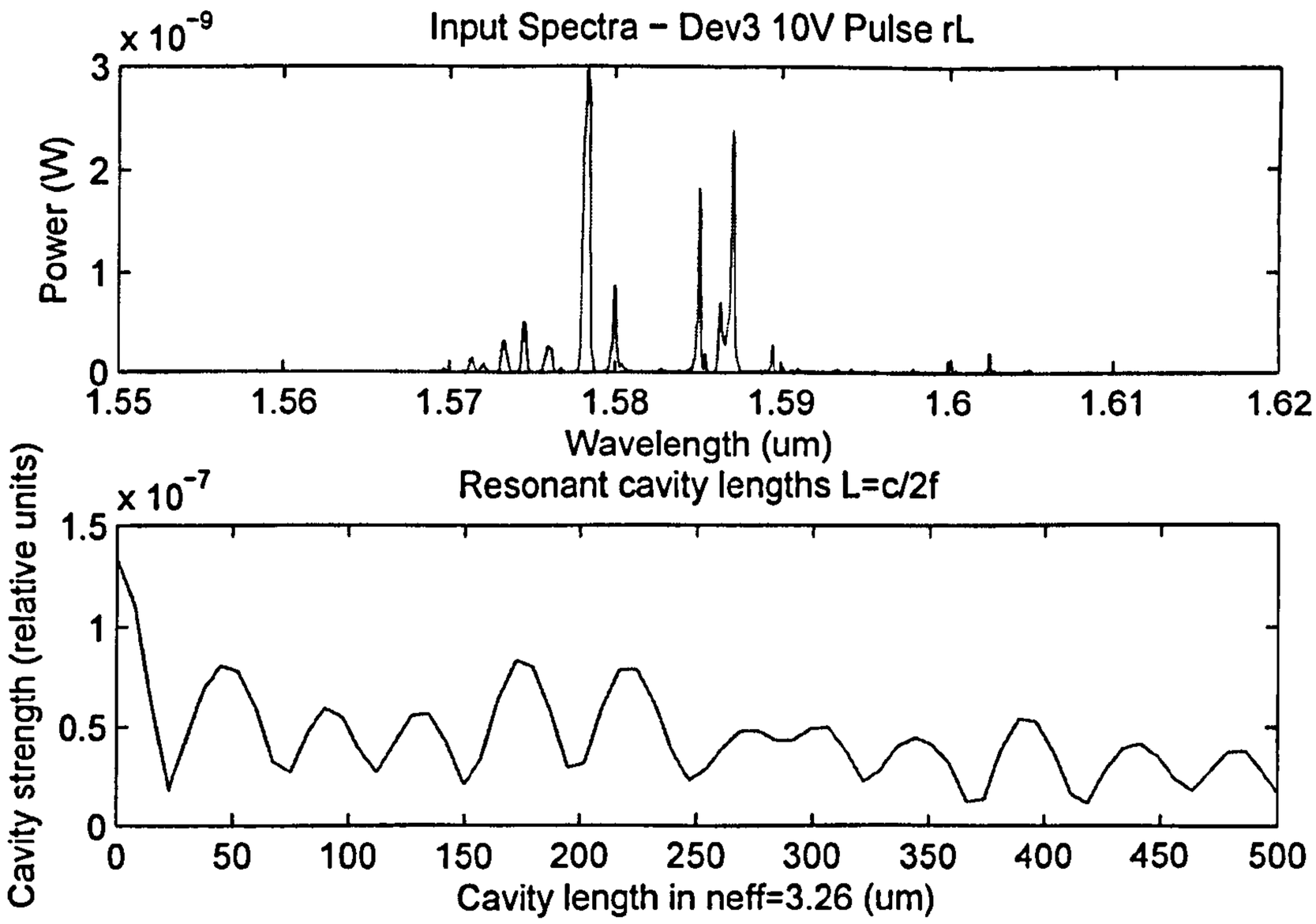

Figure 7.9: Spectra and calculated cavity length of a round one device

facet and one of the TIR mirrors. This indicates that the surface of the mirror is rough or the alignment of the mirror within the waveguide is bad. However, this device had the facets etched at and angle of 5° and the experiment repeated in figure 7.10. It can be seen that the cavity of approximately 40µm is now insignificant and the ASE spectra looks much flatter and also has a lower power as it is not starting to lase.

7.6. Polarisation Alignment

When light must be input into the device, it is important to align the polarisation with the active layer of the device as the active layer was only designed for TE mode operation. Using the setup shown in figure 7.11 the best method of aligning the polarisation before an experiment is shown below.

1. Align fibres using ASE
2. Connect the contact nearest to the input to a pico-ammeter so that the photocurrent can be measured.
3. Set the tunable laser source to a high output power (0dBm is reasonable).

fibre coupling loss of between 12 and 20dB which can be measured as the difference between the open power meter head and with fibres aligned. It can also be seen that angling the facets has increased the lasing threshold current by 50mA. This indicates that in this device there are still some reflective surfaces that lead to lasing.

7.5. Cavity lengths

If there are partially or fully reflective surfaces in an optical waveguide there will be ripples in the spectra that pass through the device. These could be passive waveguides in which case transmission or reflection spectra are required or in the case of an active waveguide, the ASE spectra can be used. The ripples occur due to interference patterns set up between these reflective surfaces, which is exactly the same as in the case of a laser where there are two intentionally reflective surfaces. The space between any two reflective surfaces is known as a cavity and some longitudinal modes are amplified between them and others are attenuated. This mechanism can be used to calculate the approximate length of these cavities. A cavity of length L will have a fundamental mode wavelength of $2L$ in the waveguide material. This will correspond to a peak in the spectra at every integer fraction of this wavelength. If this is converted to free space frequencies there will be a fixed frequency step in the spectra as calculated below.

$$f = \frac{c}{\lambda} \tag{7.6}$$

$$df = \frac{c}{2Ln_{eff}} \tag{7.7}$$

This means that there will be ripples in the frequency spectra every df step in frequency. Therefore a fast Fourier transform can be taken of the frequency spectra which will give peaks at every different df step that exists. These df steps can then be converted to cavity lengths using an approximate effective refractive index of the device. This is the method used to produce the graphs shown in figures 7.9 and 7.10 with the addition of a Hanning window function to reduce the effects of not having an infinite spectra.

Figure 7.9 shows that there is a relatively strong cavity with a length of approximately 40µm. The only position that this cavity could occur is between the active

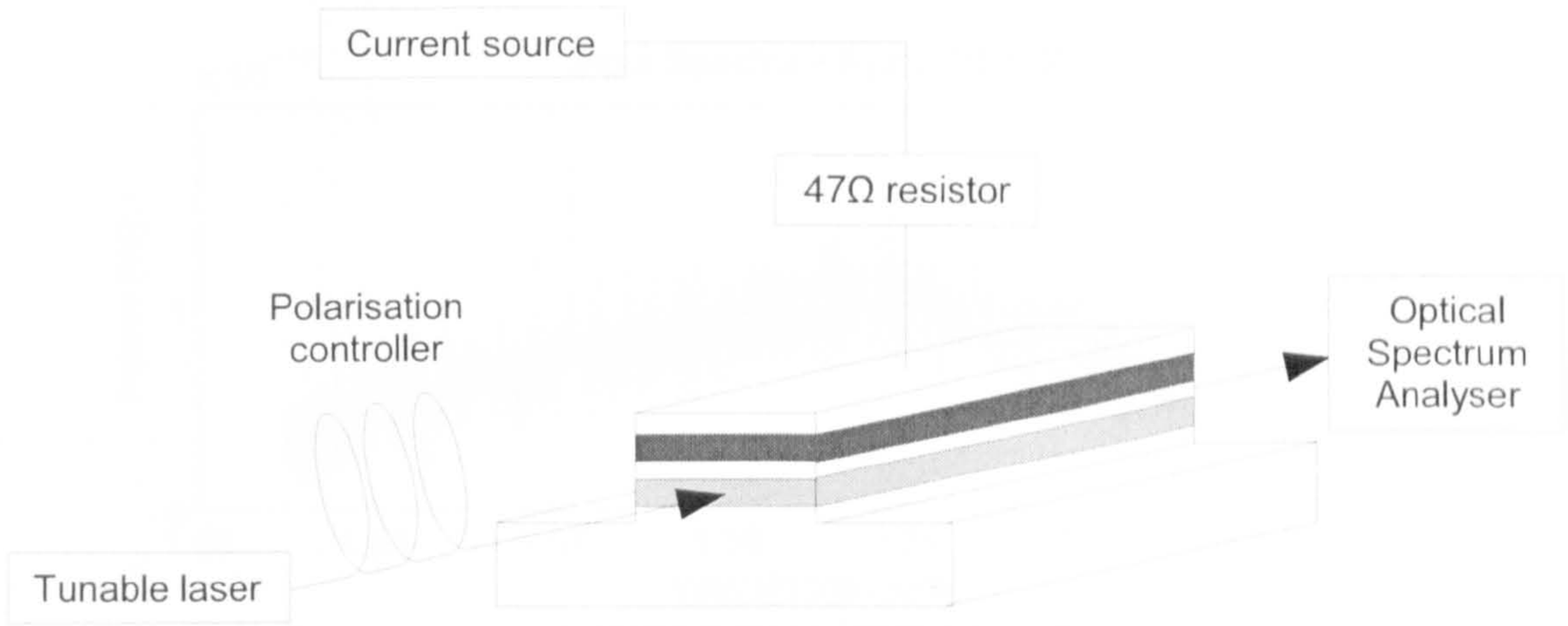

Figure 7.11: Transmission experiment

7.7. Transmission

Using the experiment setup shown in figure 7.11 the transmission characteristics with varying injection current for a round one device are shown in figures 7.12 and 7.13. These results show that a variation of over 20dB is possible by changing the carrier concentration in the active layer, for the passive to active case, at a wavelength of 1600nm. If the device in figure 7.12 was to be used as a wavelength converter it would be run at a cw current of approximately 40mA giving a high output power with no pump input. When the pump input increased in power the carriers would be depleted which means that the effect can be approximated to that of reducing the pump current. The output power would then drop by up to 20dB as it falls into the deep trough. There is a trend where the deep trough position reduces in current injection as longer wavelengths are used. This is due to the slightly different optical length of the waveguides to different wavelength of light, so the point of maximum destructive interference is moved. However, assuming that the junction is very lossy as explained in section 7.9, the 40mA injection current would not be enough to take the device into the gain region, so this device would be operating in the attenuation region. This means that a greater pump power would increase the number of free carriers so the operating points described above would have to be swapped around.

Figure 7.14 shows the passive to passive gain of a round 2 device altering with the temperature of the device mount. It can be seen that altering the temperature of the mount has a large effect on the transmission results which is another indication

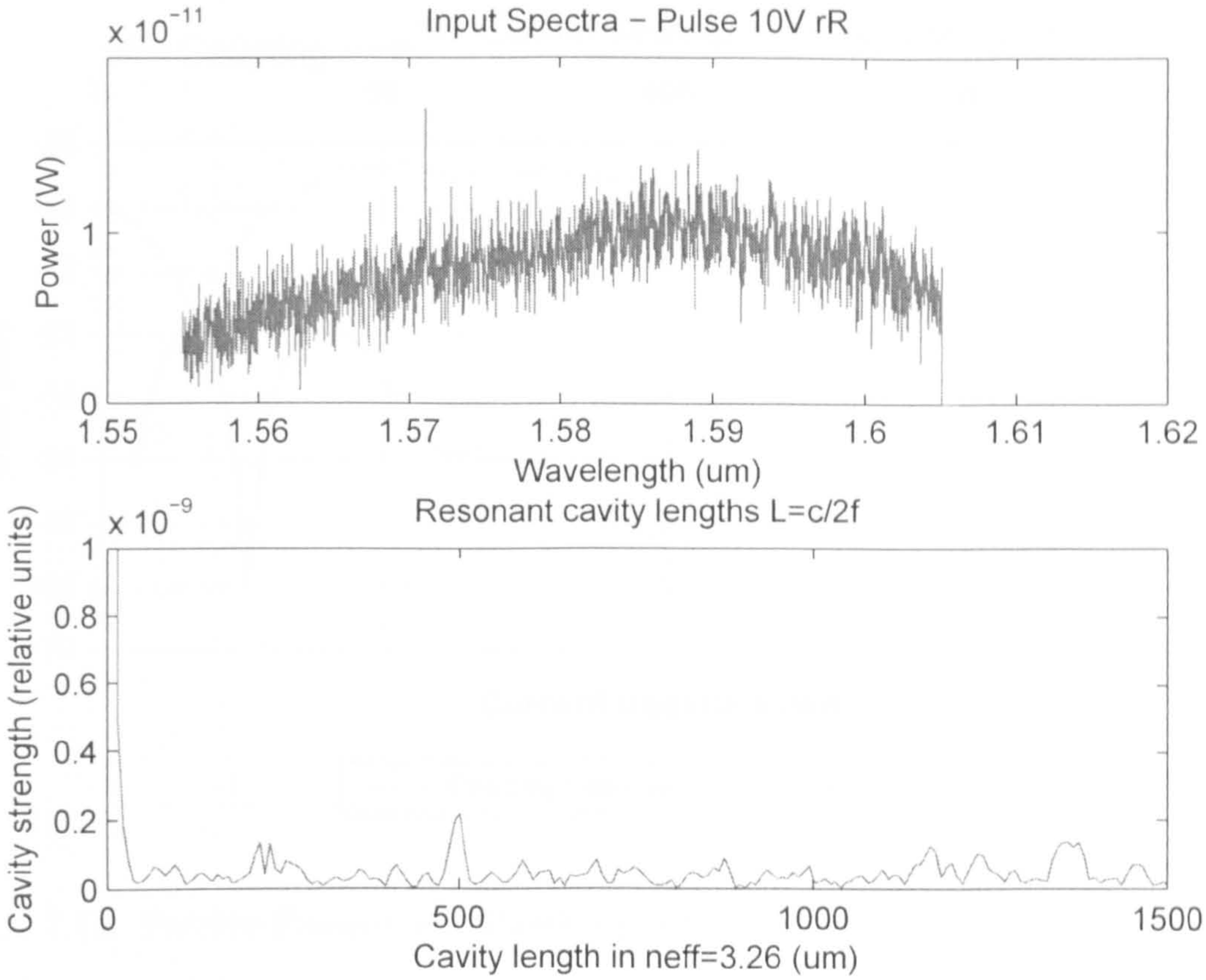

Figure 7.10: Spectra and calculated cavity length of a round one device with angled facets

4. Adjust the polarisation controller paddles until maximum photocurrent is found.

An alternative method is shown below that is especially useful when the alignment stages and the polarisation controller are controlled from the computer using new Visual Basic software and the alignment is changing often.

1. Align input and output fibres using ASE.
2. Set couple injection current to a known peak or trough in the transmission.
3. Set the tunable laser to a high output power.
4. Track the polarisation controller to the maximum or minimum transmission power.
5. Realign the fibres using the transmission power.
6. Track the polarisation every time the fibre positions alter.

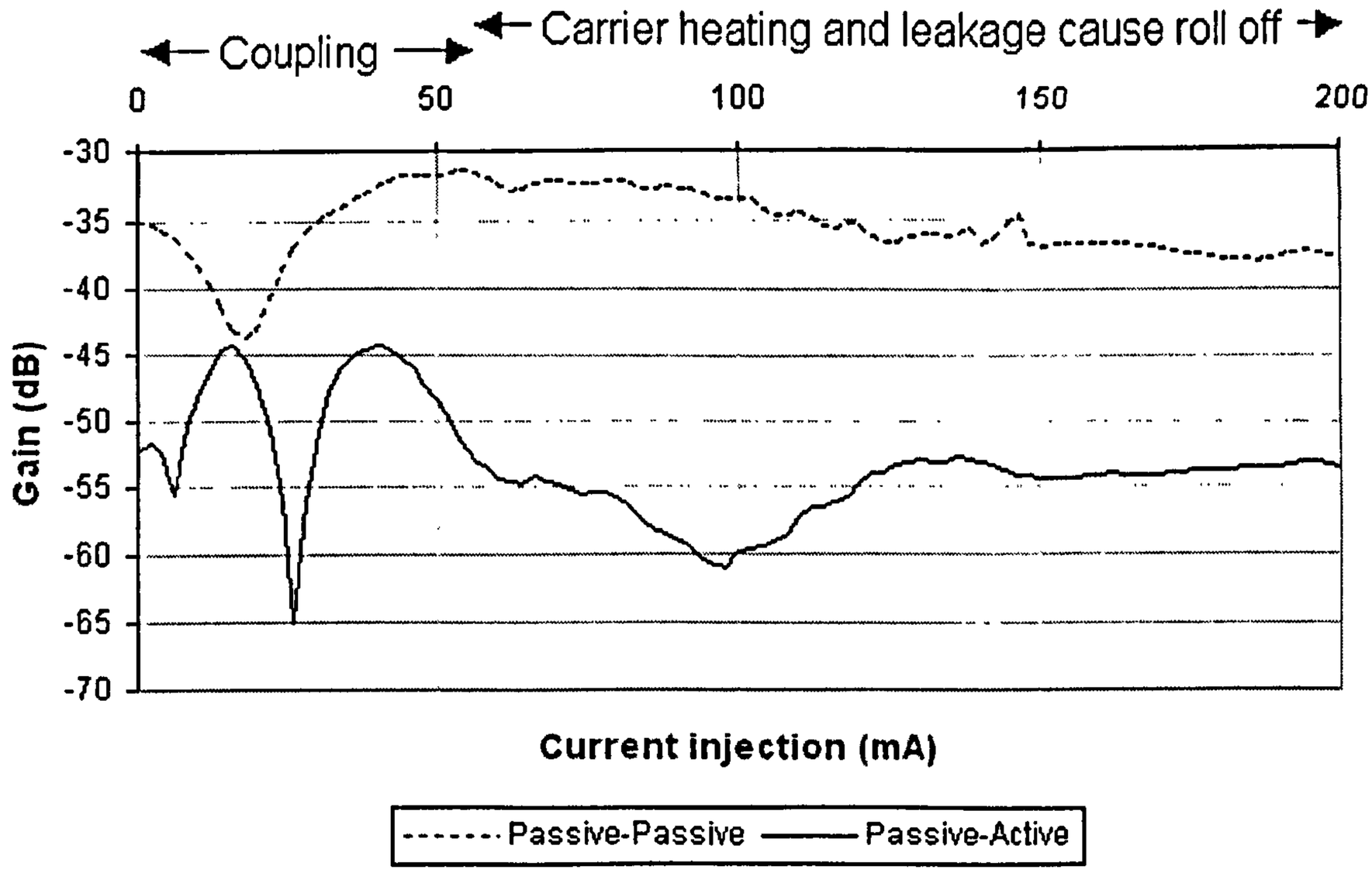

Figure 7.12: Passive-Passive and Passive-Active gain measured on an optical spectrum analyser (OSA) for a round one device at 1600nm with cw current injection of the overheating of the device as explained in section 7.9.

7.8. Wavelength conversion

The devices were tested for wavelength conversion using the setup in figure 7.15, however none of the devices tested exhibited a change in the probe power as the pump power was altered. The coupling losses in the round one devices of 15 to 20dB at each facet were too high for the pump to saturate the device as the highest pump power available was 14dBm. The round two devices were not very robust and so did not survive for long enough to test for wavelength conversion. Also, the very low current efficiency observed means that there is only a low carrier concentration in the quantum wells, meaning that the change in probe output power would not be observable as there would be little gain to be saturated. Also, the longer than designed operation wavelength of the devices meant that no optical amplifiers were available that were designed to operate at that wavelength.

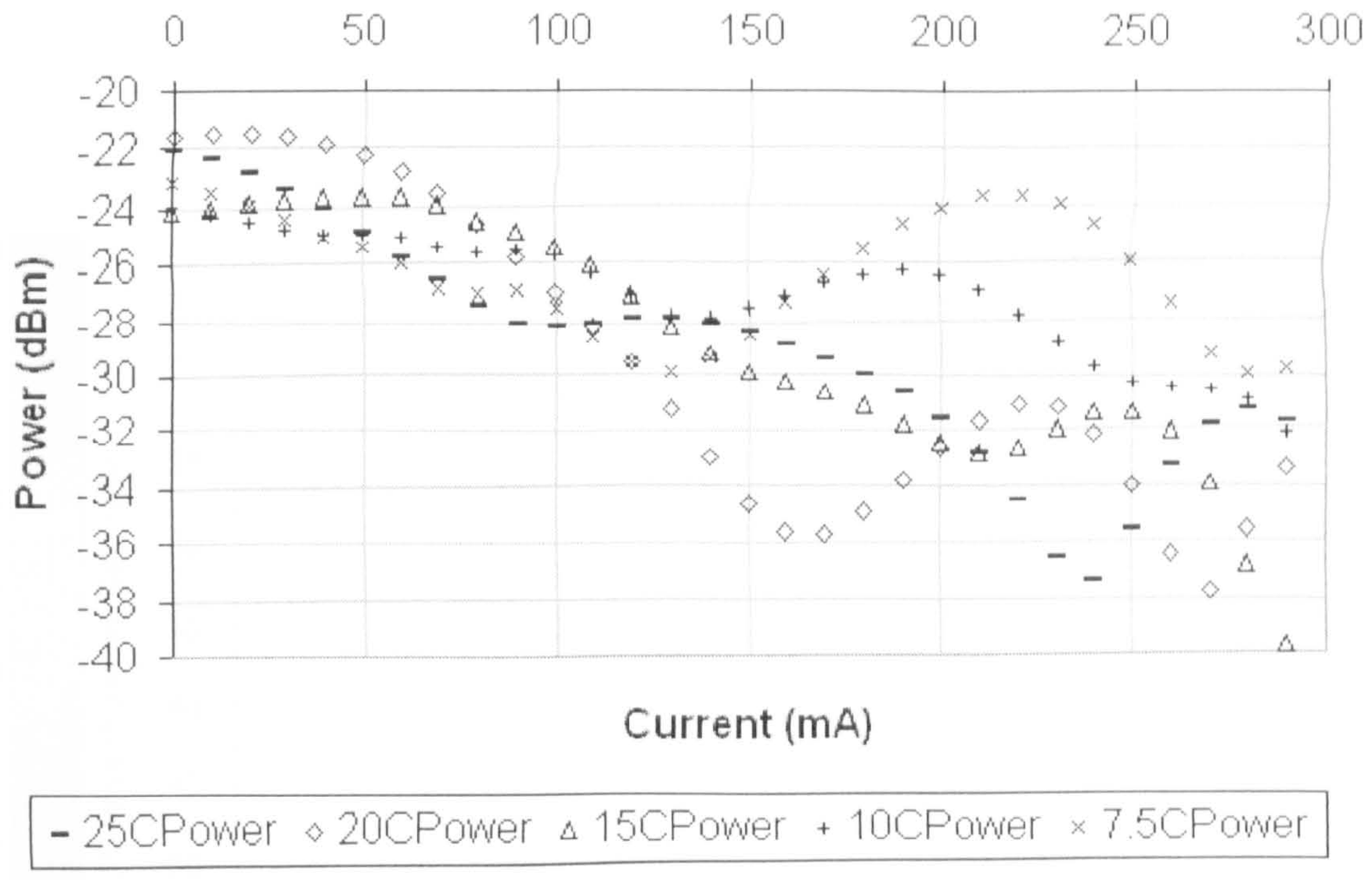

Figure 7.14: Passive-Passive transmission curve of a $880\mu m$ round two device at 1585nm

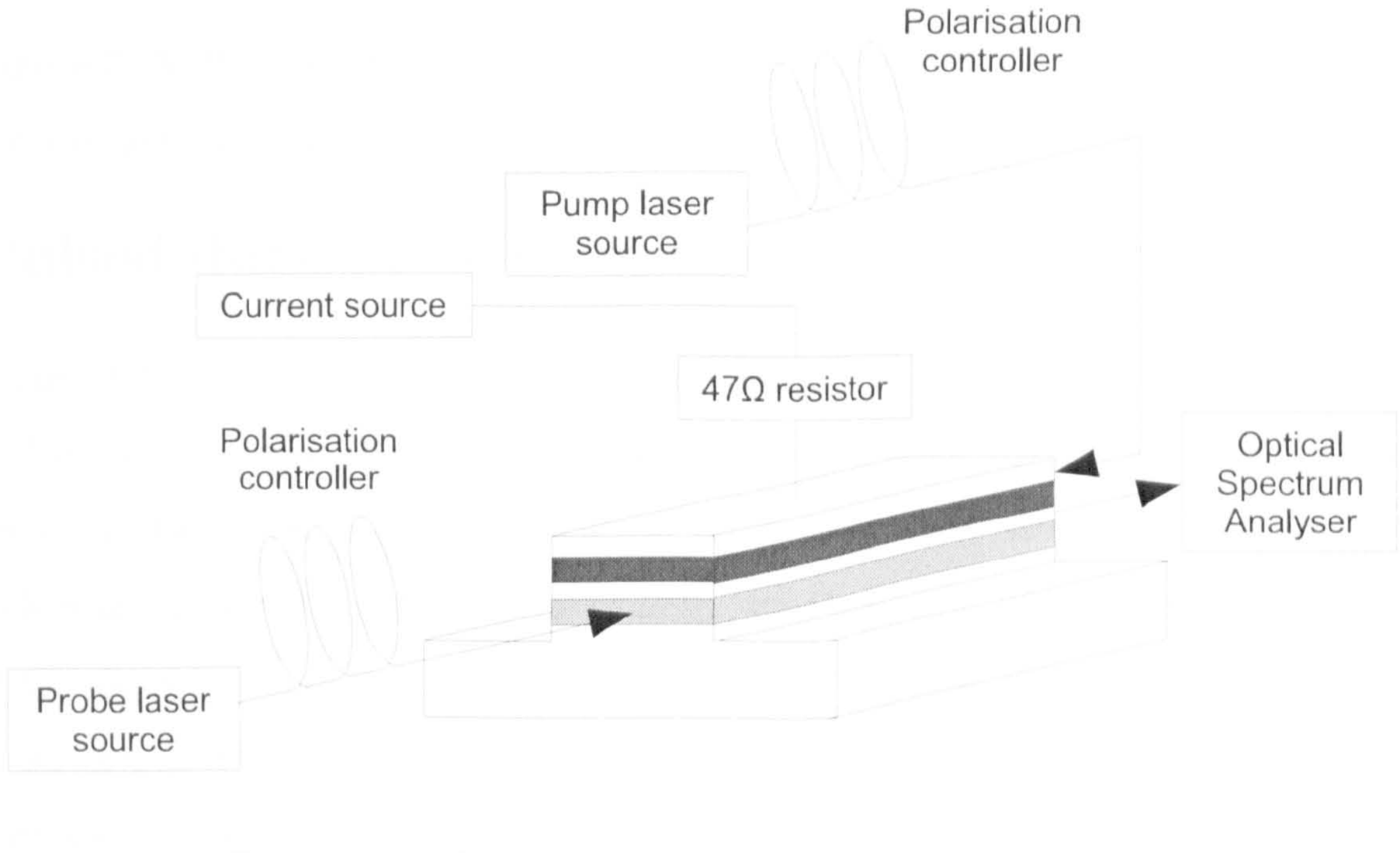

Figure 7.15: Wavelength conversion experiment setup

explanation is that the gain peak of the devices is at a wavelength of approximately 1600nm as seen in figures 7.9 and 7.10. If the carrier concentration was as high as was intended the gain peak would be shifted to a shorter wavelength of approximately 1550nm. This is not a simulation problem as the simulation predicts the carrier

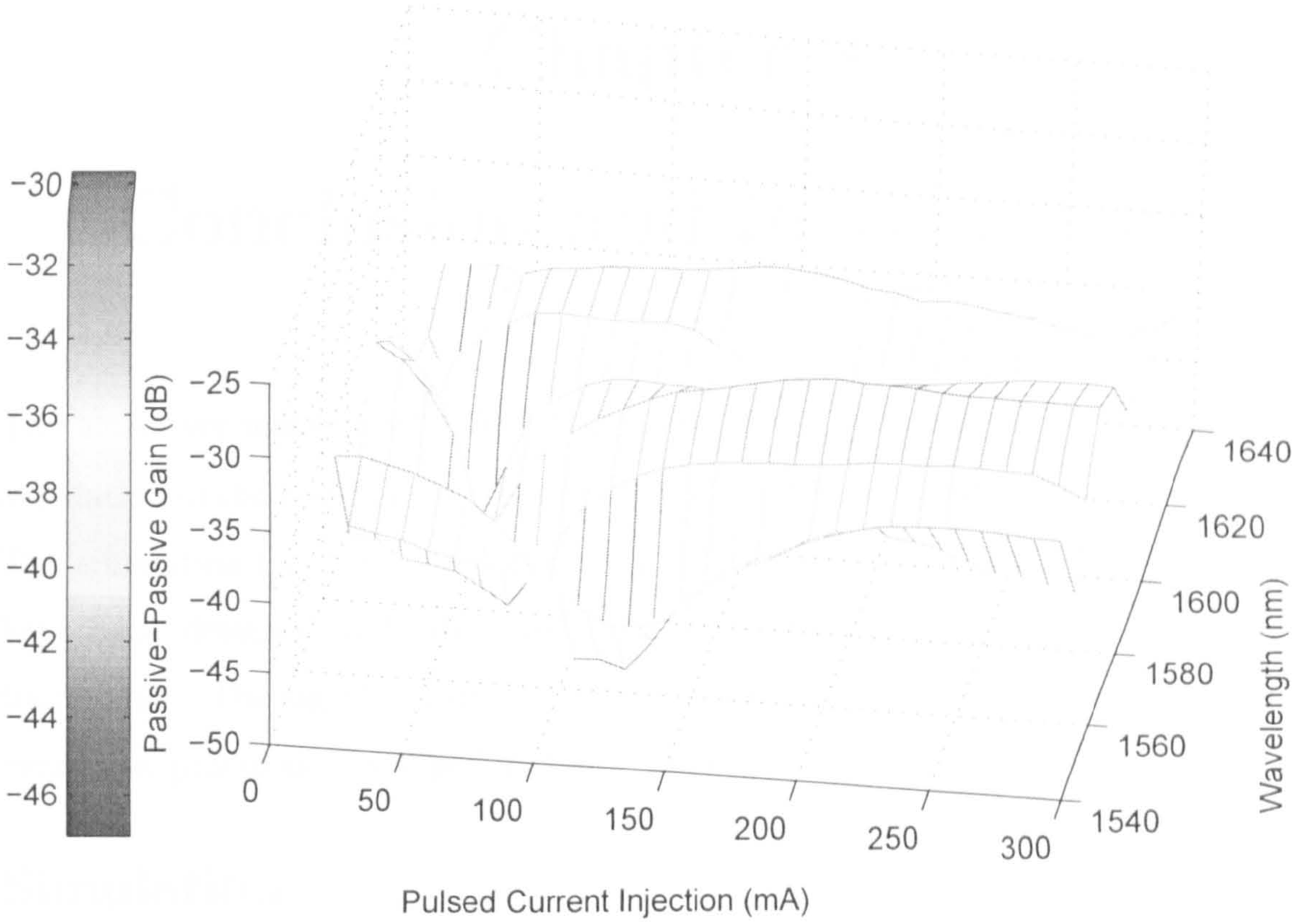

Figure 7.13: Passive-Passive gain measured on an optical spectrum analyser (OSA) for a round one device with varying wavelength

7.9. Pulsed duty cycle comparison

Figure 7.16 shows that the larger the duty cycle, the smaller the ASE power. This is due to the active junction overheating, which causes a large increase in carrier recombination that reduces the carrier concentration in the active region. This reduction causes the optical gain to drop dramatically. Reducing the duty cycle of the electrical pulse means that the proportion of time the device is operating in an overheated condition is reduced, so the average ASE power in that pulse is increased. This overheating effect is due to the fact that the barrier potentials between the quantum wells are too low. Therefore, when the junction heats up the concentration of carriers in the quantum wells will decrease significantly as the carriers have enough energy to escape the barriers and recombine. This also explains the short life expectancy of the devices as the junction temperature is extremely high which is likely to cause irreversible damage. Another observation that backs up this

Chapter 8

Conclusion and further work

The active vertical coupler (AVC) waveguide structure has been investigated and a simulation of the non-linear effects in the AVC has been designed and implemented. The simulation has been validated using existing devices, after which new devices have been designed and fabricated. These devices have then been characterised thoroughly. During the course of this research many interesting problems were overcome, processes developed and mechanisms discovered.

8.1. Simulation

A flexible simulation has been implemented using Microsoft Visual C++ 6 and the commercial software Fimmwave, by Photon Design. This simulation has the flexibility to model any multiple waveguide device with multiple inputs and outputs at multiple wavelengths. It models the affect of amplified spontaneous emission and the injected light from all ports on the carrier concentration throughout the length of the device. This means that non-linear saturation effects are also modelled allowing the simulation of many types of active device.

The simulation requires some assumptions to simplify the problem to make it realistic to simulate. The carrier concentration distribution across the active layer is assumed to be constant as is the light intensity. This assumption is valid for quantum well devices with a limited number of quantum wells as the concentration of the carriers in the wells is much higher than in the barrier region and the active layer is very thin compared to the width of the optical mode in the waveguide. Due to this assumption and the fact that the confinement factor can only be extracted from one particular area per simulation only one active waveguide can be simulated in any given structure.

Any broadband signal must be simulated at a single wavelength, so the noise

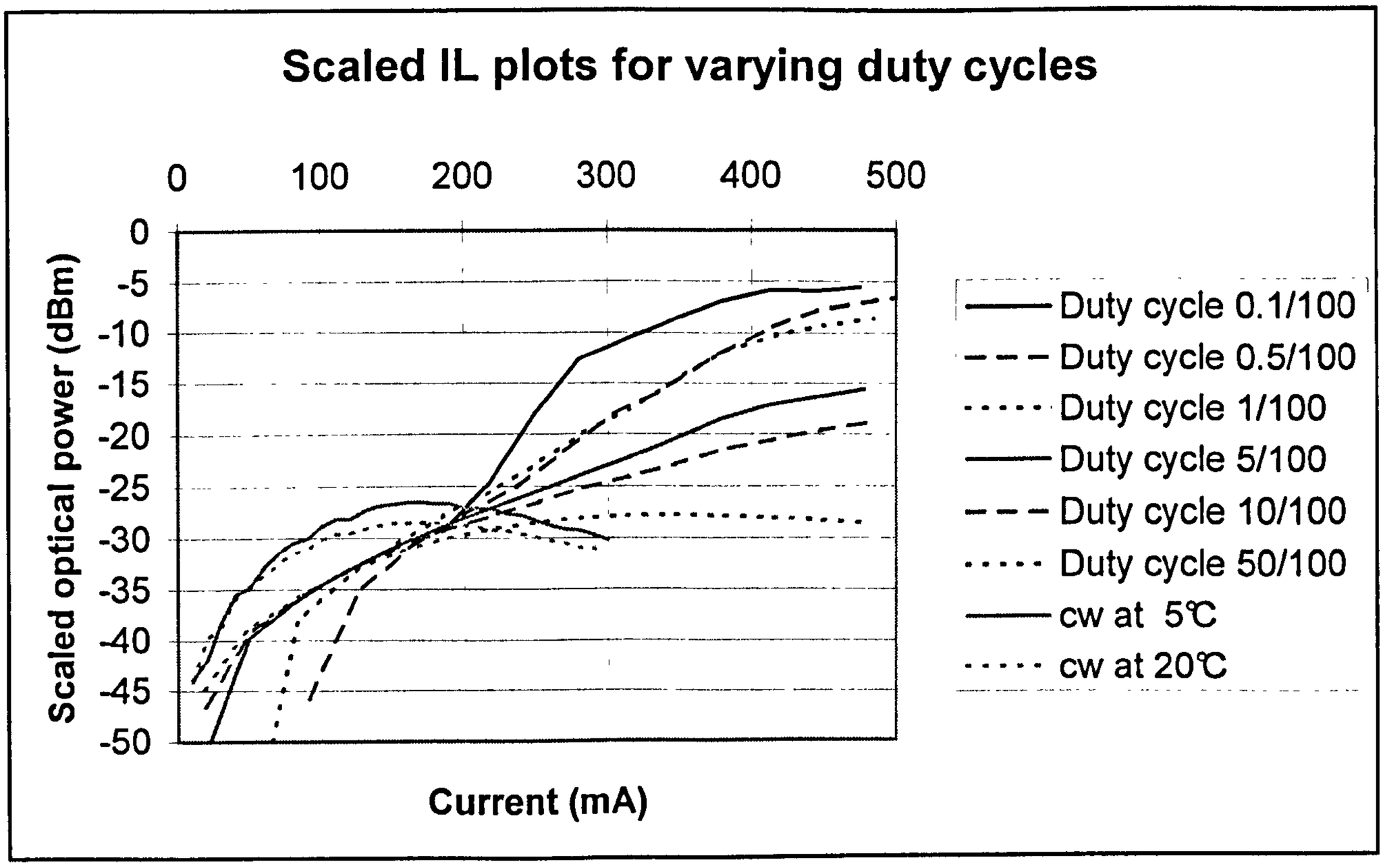

Figure 7.16: Round one device varying pulse duty cycle

saturation correctly when applied to the different wafer structure of a cross-point device (see figure 2.2.

8.4. Characterisation

The characterisation of preexisting devices and the devices fabricated for this thesis show good correlation with the simulated results where it is possible to compare them. Unfortunately the quality of the fabricated devices was found to be bad due to low quantum well barriers and due to delays in the wafer manufacture it was not possible to order a second round of wafers to be grown.

Automated systems for characterisation were developed using computer controlled lab equipment, which allowed fast, accurate measurements to be taken. Automated fine alignment and tacking of fibre coupling and polarisation control was developed and implemented successfully.

Electrical voltage vs current (VI) results were obtained showing correct diode characteristics, all though indicating some loss of current through leakage around the p-n junction of the devices, by a slow turn on of the diode. Amplified spontaneous emission (ASE) measurements were taken, showing the optical characteristics of the devices and how they were affected by temperature and duty cycle of the injected current. This indicated that the junction was overheating causing significant loss of the optical properties of the quantum wells in the devices. This information along with fitting the simulated ASE to the experimental results showed that the current efficiency and therefore the quantum efficiency of the devices was 10-15%. The reason for this is that the barriers between the quantum wells are too low, meaning that the carrier concentration in the quantum wells is much lower than predicted. Also, any heating of the junction will cause carriers to easily escape the wells and recombine, causing heating rather than optical power.

Transmission measurements were found to have output extinction ratios of over 20dB with a variation of pulsed current injection. This result is explained by the device working well in the absorption region as the carrier concentration was not enough to cause gain in the device at the injection current levels supplied. The devices would not exhibit wavelength conversion as they were operating in the absorption region rather than the gain region that they were designed for.

introduced and amplified by a device is approximate. This means that the broadband spontaneous emission is simulated at the gain peak of the material thereby introducing some inaccuracies.

An initial implementation of timing simulation has been implemented, however it has not yet been developed to give accurate results.

8.2. Design

The simulation has been used to design a wavelength converter device using an AVC structure with a steady-state output extinction ratio of 30dB, with a maximum input power after coupling to the semiconductor of 6dBm. This wafer and coupler design has had integrated optical components designed to supplement it to produce a wavelength converter device with angled facets with mode expanders that will couple to fibre arrays with minimal losses.

8.3. Fabrication

Many fabrication processes were developed and optimised during the fabrication stages of this research. One of these processes is a consistent, fast, indium phosphide etch process that will not sputter nickel masks and that has a very low mask erosion rate. A very fast inductively coupled plasma etch process has been developed for the deep etching of indium phosphide. Software that allows simple profile measurements to be taken from a Talysurf Plus profiler has been written that has the added advantage of removing the need for paper that sheds particles in the clean room. All the processes involved in photo lithography, metal film deposition and wet etching have been optimised for the devices fabricated.

Silicon oxide and nitride deposition processes were developed on a recently upgraded PECVD machine giving good reliable results for the oxide process. The nitride process was found to have low adhesion with the semiconductor surface due to changes in the equipment during the upgrade.

cation more difficult but should reduce the loss at the mirrors.

8.5.3. Fabrication

Any new devices being fabricated should use a stable passivation layer by either developing the silicon nitride process further on the upgraded PECVD or by using silicon oxide.

The sub-mount bonding step could be improved dramatically if a gold/tin solder source was available for the sputtering machine. This would require another photo lithography step after the samples had been annealed so that the solder could be deposited only over the contacts. The advantage of this extra stage is that the flipped device would easily solder onto a gold coated sub-mount, removing the problems of placing tiny amounts of solder in the correct places. It would also remove the requirement for contact studs on the sub-mount as the amount of solder would be sufficient that it would not flow over the junction.

8.5.4. Characterisation

The new devices fabricated should be tested for ASE power and transmission with current injection as the previous rounds of devices have been. These results can then be used to refine simulation parameters particularly the recombination time constants A,B and C and the new spontaneous emission factor, Nsp', if a new spontaneous emission simulation has not been implemented. The results from devices without large injection current losses can also be used to check the material properties $\frac{dn}{dN}$ and $\frac{dg}{dN}$. Once these parameters have been checked, the devices can be tested for wavelength conversion and the results compared to the simulation predictions.

8.5. Future work

8.5.1. Simulation

The simulation could be improved by allowing the ASE to be propagated at increasing numbers of different wavelengths and where the SE is created according to the SE spectra which is wider than the gain spectra and does not reduce to below zero at low carrier densities. This will improve the simulation at low carrier densities and allow devices to be accurately modelled in the adsorption region. The spread of ASE over different wavelengths will increase the simulation time in proportion to the number of wavelengths as each wavelength is treated as almost a separate simulation. This means that it should only be used if found to be important to simulating the ASE correctly.

The simulation could also be improved by including more mechanisms in the timing simulation. Carrier transport effects associated with carriers moving between the barrier layer and the quantum wells [26] will affect the high-speed response times greatly and should therefore be included in the simulation. Spectral hole burning [34] could have a large impact on the dynamic response of the device, so this must be included in the model. Another process that must be investigated is carrier heating [34] as it could also have a significant impact on the time response of the device.

8.5.2. Design

To continue the work begun in this thesis the next step would be to simulate, design and fabricate devices with higher barriers between the quantum wells. This would involve using a material for the barriers with a lower band gap than the 1.3μm band gap that is currently in the design. It should not alter the optical simulation properties significantly, so only small changes are expected in the new device designs.

Changing the active waveguide to be made from strained quantum wells would make the device polarisation insensitive which is a current aim of many optical devices as it simplifies the alignment of devices in a system. It also permits the use of orthogonal polarisations to transfer a greater amount of data or a control signal.

The total internal reflection mirrors could be improved by including the Goos-Hänchen shift [17] when designing them. This would make alignment during fabri-

[9] T. Durhuus, B. Mikkelsen, C. Joergensen, S. Lykke Danielsen, and KE Stubkjaer. All-optical wavelength conversion by semiconductor opticalamplifiers. *Lightwave Technology, Journal of*, 14(6):942–954, 1996. [8]

[10] AD Ellis and DM Spirit. Compact 40Gbit/s optical demultiplexer using a GaInAsP opticalamplifier. *Electronics Letters*, 29(24):2115–2116, 1993. [4]

[11] JMH Elmirghani and HT Mouftah. All-optical wavelength conversion: technologies and applications inDWDM networks. *Communications Magazine, IEEE*, 38(3):86–92, 2000. [8]

[12] G. Giuliani and D. DAlessandro. Noise Analysis of Conventional and Gain-Clamped Semiconductor Optical Amplifiers. *JOURNAL OF LIGHTWAVE TECHNOLOGY*, 18(9), 2000. [19, 21]

[13] D. Goff. *Fiber Optic Reference Guide.* Focal Press, 2002. [1]

[14] Jim Hayes. *Fiber Optics Technician's Manual.* Thomson Delmar Learning, 2 edition, 2000. [1]

[15] J. Hecht. *Understanding fiber optics.* Prentice Hall Upper Saddle River, NJ, 2002. [1]

[16] E. Iannone and R. Sabella. Optical path technologies: a comparison among differentcross-connect architectures. *Lightwave Technology, Journal of*, 14(10):2184–2196, 1996. [6]

[17] HM Lai, FC Cheng, and WK Tang. Goos–Hänchen effect around and off the critical angle. *J. Opt. Soc. Am. A*, 3:550–557, 1986. [46, 94]

[18] S.C. Lee, R. Varrazza, O. Ansell, and S. Yu. Highly Flexible 4×4 Optical Cross-point Packet Switch Matrix for Optical Multicast Operations. *Photonics Technology Letters, IEEE*, 17(4):911–913, 2005. [viii, xi, 33, 34]

[19] T. Liu, K. Obermann, K. Petermann, F. Girardin, and G. Guekos. Effect of saturation caused by amplified spontaneous emission on semiconductor optical amplifier performance. *ELECTRONICS LETTERS*, 33:24, 1997. [21]

[20] B. Ma and Y. Nakano. Realization of All-Optical Wavelength Converter Based on Directionally Coupled Semiconductor Optical Amplifiers. *IEEE PHOTONICS TECHNOLOGY LETTERS*, 11(2), 1999. [9]

Bibliography

[1] M. Saitoh B. Ma and Y. Nakano. Analysis and fabrication of an all-optical wavelength converter based on directionally-coupled semiconductor optical amplifiers. *IEICE Transactions on Electronics*, E83-C(2), Feb 2000. [6]

[2] NAN CHI, J.J. VEGAS OLMOS, K. THAKULSUKANANT, Z. WANG, O. ANSELL, S. YU, and D. HUANG. Experimental characteristics of optical crosspoint switch matrix and its applications in optical packet switching. *Journal of lightwave technology*, 24(10):3646–3653, 2006. [xi, 35]

[3] KG Coffman and A.M. Odlyzko. Internet growth: Is there a Moores Law for data traffic. *Handbook of Massive Data Sets*, 2001. [1]

[4] SL Danielsen, PB Hansen, and KE Stubkjaer. Wavelength conversion in optical packet switching. *Lightwave Technology, Journal of*, 16(12):2095–2108, 1998. [5, 6]

[5] J. De Merlier, D. Van Thourhout, G. Morthier, and R. Baets. Amplified spontaneous emission in index-guided multimodal waveguide structures. *Quantum Electronics, IEEE Journal of*, 39(9):1099–1105, 2003. [21]

[6] Casimer DeCusatis. Optical data communication: fundamentals and future directions. *SPIE Optical Engineering*, 37(12):3082–3099, Dec 1998. [vii, 1, 2]

[7] S. Diez and H.G. Weber. Noise Analysis of Frequency Converters Utilizing Semiconductor-Laser Amplifiers. *IEEE JOURNAL OF QUANTUM ELECTRONICS*, 33(1), 1997. [21]

[8] M. Duelk, J. Gripp, J. Simsarian, A. Bhardwaj, P. Bernasconi, M. Zirngibl, and O. Laznicka. Fast packet routing in a 2.5 Tb/s optical switch fabric with 40 Gb/s duobinary signals at 0.8 b/s/Hz spectral efficiency. *Optical Fiber Communications Conference, 2003. OFC 2003*, 2003. [6]

[32] G. Talli and M.J. Adams. Gain dynamics of semiconductor optical amplifiers and three-wavelength devices. *Ieee Journal of Quantum Electronics*, 39(10), 2003. [21, 22]

[33] G. Talli et al. Amplified spontaneous emission in semiconductor optical amplifiers: modelling and experiments. *Optics Communications*, 218(1):161–166, 2003. [17, 21]

[34] JM Tang and KA Shore. Strong picosecond optical pulse propagation in semiconductoroptical amplifiers at transparency. *Quantum Electronics, IEEE Journal of*, 34(7):1263–1269, 1998. [94]

[35] L. Thylen. Amplified spontaneous emission and gain characteristics ofFabry-Perot and traveling wave type semiconductor laser amplifiers. *Quantum Electronics, IEEE Journal of*, 24(8):1532–1537, 1988. [22]

[36] G. et al. Toptchiyski. Time-domain modeling of semiconductor optical amplifiers for otdm applications. *Journal of Lightwave Technology*, 17(12), 1999. [21]

[37] K. TSUJI, N. MATSUSHITA, N. ONODERA, and M. SARUWATARI. Analysis of XGM-Based Wavelength-Conversion Using ASE in SOAs. *IEICE TRANSACTIONS on Electronics*, 86(5):741–748, 2003. [21]

[38] R. Varrazza, I.B. Djordjevic, and S. Yu. Active Vertical-Coupler-Based Optical Crosspoint Switch Matrix for Optical Packet-Switching Applications. *JOURNAL OF LIGHTWAVE TECHNOLOGY*, 22(9), 2004. [9, 30]

[39] J. Yates, J. Lacey, D. Everitt, and M. Summerfield. Limited-range wavelength translation in all-optical networks. *INFOCOM'96. Fifteenth Annual Joint Conference of the IEEE Computer Societies. Networking the Next Generation. Proceedings IEEE*, 3, 1996. [7]

[40] SJB Yoo. Wavelength conversion technologies for WDM network applications. *Lightwave Technology, Journal of*, 14(6):955–966, 1996. [7]

[41] S. Yu, S.C. Lee, O. Ansell, and R. Varrazza. Lossless Optical Packet Multicast Using Active Vertical Coupler Based Optical Crosspoint Switch Matrix. *Lightwave Technology, Journal of*, 23(10):2984–2992, 2005. [viii, xi, 34]

[42] S. Yu, R. Varrazza, M. Owen, RV Penty, IH White, D. Rogers, S. Perrin, and CC Button. Ultra-low crosstalk, compact integrated optical crosspoint spaceswitch arrays employing active InGaAsP-InP vertical waveguide couplers. *Lasers and Electro-Optics,*

[21] Y. Matsui, S. Kutsuzawa, S. Arahira, and Y. Ogawa. Generation of wavelength tunable gain-switched pulses from FP MQWlasers with external injection seeding. *Photonics Technology Letters, IEEE*, 9(8):1087–1089, 1997. [3]

[22] Y. Matsui, M.D. Pelusi, and A. Suzuki. Generation of 20-fs Optical Pulses from a Gain-Switched Laser Diode by a Four-Stage Soliton Compression Technique. *IEEE PHOTONICS TECHNOLOGY LETTERS*, 11(10):1217, 1999. [3]

[23] P.P. Mitra and J.B. Stark. Nonlinear limits to the information capacity of optical fiber communications. *Arxiv preprint physics/0011016*, 2000. [2]

[24] T. Miya, Y. Terunuma, T. Hosaka, and T. Miyashita. Ultimate low-loss single-mode fibre at 1.55 micron. *Electronics Letters*, 15:106–108, 1979. [1]

[25] B. Mukherjee. WDM optical communication networks: progress and challenges. *Selected Areas in Communications, IEEE Journal on*, 18(10):1810–1824, 2000. [3]

[26] LVT Nguyen, AJ Lowery, PCR Gurney, and D. Novak. A time-domain model for high-speed quantum-well lasers includingcarrier transport effects. *Selected Topics in Quantum Electronics, IEEE Journal of*, 1(2):494–504, 1995. [94]

[27] NS Patel, KL Hall, and KA Rauschenbach. 40-Gbit/s cascadable all-optical logic with an ultrafast nonlinear interferometer. *Opt. Lett*, 21(18):1466–1468, 1996. [9]

[28] K. Petermann. Calculated spontaneous emission factor for double-heterostructure injection lasers with gain-induced waveguiding. *IEEE Journal of Quantum Electronics*, 1979. [21]

[29] M. Saitoh, B. Ma, and Y. Nakano. Static and dynamic characteristics analysis of all-opticalwavelength conversion using directionally coupled semiconductor opticalamplifiers. *Quantum Electronics, IEEE Journal of*, 36(8):984–990, 2000. [17]

[30] M. Shtaif and G. Eisenstein. Noise characteristics of nonlinear semiconductor optical amplifiersin the Gaussian limit. *Quantum Electronics, IEEE Journal of*, 32(10):1801–1809, 1996. [22]

[31] H. Takahashi, S. Suzuki, K. Kato, and I. Nishi. Arrayed-waveguide grating for wavelength divisionmulti/demultiplexer with nanometre resolution. *Electronics Letters*, 26(2):87–88, 1990. [3]

1999. CLEO'99. Summaries of Papers Presented at the Conference on, 1999. [9, 30, 43]

[43] J. Zhou, N. Park, KJ Vahala, MA Newkirk, and BI Miller. Four-wave mixing wavelength conversion efficiency in semiconductortraveling-wave amplifiers measured to 65 nm of wavelength shift. *Photonics Technology Letters, IEEE*, 6(8):984–987, 1994. [vii, 8, 9]